©Copyright 2022

Sian Jin

Vehicular Radar Network: Cross-layer Design Optimization

Sian Jin

A dissertation
submitted in partial fulfillment of the
requirements for the degree of

Doctor of Philosophy

University of Washington

2022

Reading Committee:
Sumit Roy, Chair
Thomas Henderson
Hui Liu

Program Authorized to Offer Degree:
Electrical and Computer Engineering

University of Washington

Abstract

Vehicular Radar Network: Cross-layer Design Optimization

Sian Jin

Chair of the Supervisory Committee:
Sumit Roy
Electrical and Computer Engineering

With the increasing proliferation of radars on vehicles, interference among vehicular radars is becoming a serious issue. In this thesis, we consider the most widely adopted frequency modulated continuous wave (FMCW) automotive radars. We analyze and propose methods to mitigate two types of interference, coherent interference and incoherent interference. Coherent radar interference is the interference with the same FMCW waveform parameters of victim radar, while incoherent radar interference is the interference with different FMCW waveform parameters.

For dealing with coherent interference, we propose to adopt media access control (MAC) protocols for mutual radar interference mitigation. We propose two cross-layer performance metrics - multiple access capacity and probability of target misdetection to quantify the network performance under each MAC protocol. Based on our analysis and extensive simulations, we find that pure random access achieves a very poor trade-off between multiple access capacity and probability of target misdetection. However, such a trade-off can be significantly improved by frequency hopping and phase coding. This shows that proper MAC protocols can achieve very good coherent interference mitigation performance even without synchronization and coordination. We describe new insights behind such gains that can be

valuable for FMCW radar MAC design.

To improve the range-velocity detection performance under incoherent interference, we exploit distinguished features of target and interference components in the fast-time-frequency (fTF) representation and propose to directly recover the underwhelmed target component via the fast-time-frequency mode retrieval (fTFMR). This is achieved by utilizing the Fourier synchrosqueezed transform (FSST) and introducing robust ridge detection that, in combination, guarantees that the recovered fast-time errors of the target signal are bounded at separable time intervals. Comprehensive performance comparison with a list of baseline methods shows that the fTFMR method yields higher output signal-to-interference-noise ratios (SINRs) at both the range and velocity domains and reduces the false alarm compared to the state-of-the-art fast-time interference mitigation methods.

To improve the angle detection performance under incoherent interference, we formulate a spatial multiple-input multiple-output (MIMO) detection problem that counts for interference structure and propose a subspace-based detector in the framework of generalized likelihood ratio test (GLRT). We derive the exact theoretical performance of the proposed subspace-based GLRT detector and show that it's a constant false alarm rate (CFAR) detector. Further, we extend our analysis to massive MIMO radar and show that the proposed subspace-based GLRT detector has perfect angle detection performance under interference when the array size goes to infinity. We theoretically derive the massive MIMO regime where the proposed subspace-based detector is guaranteed to achieve a high enough detection probability under interference. Extensive simulations show the superior performance of our proposed subspace-based GLRT detection scheme compared to the classic detector and validate the effectiveness of massive MIMO for interference mitigation.

TABLE OF CONTENTS

LIST OF FIGURES

ACKNOWLEDGMENTS

I wish to express sincere appreciation to University of Washington, where I have had the opportunity to work on my Ph.D. degree. I thank my academic advisor Dr. Sumit Roy, who has provided me a lot of guidance on my radar interference mitigation project and my ns-3 wireless network simulation project. During my early stage of my Ph.D., Dr. Roy corrected my lots of mistakes and taught me how to work on good problems. We work closely in nearly all of my papers published in my Ph.D. program. I not only thank Dr. Roy for his guidance on my projects and papers but also thank his advice on my future career. I also appreciate the help from Dr. Hui Liu, one of the most important people in my life. Dr. Liu introduces me to University of Washington and has provided me with a lot of opportunities. Without Dr. Liu's recommendation, I cannot even come to the US. I cannot imagine what my life will be without the help of Dr. Liu. I further thank Dr. Thomas R. Henderson, one of my advisors on my ns-3 project and my close collaborator who give me a lot of guidance. I really appreciate Dr. Henderson for his patience in guiding me to work on ns-3 codes. I also really appreciate Dr. Henderson's recommendations in my job search. I thank Dr. Guanbin Xing for his instructions on my vehicular radar project. I thank all of my other current or previous supervisory committee members, Dr. Payman Arabshahi, Dr. Kurtis Heimerl, and Dr. Tadesse Ghirmai for their time in supervising me. I also thank my ECE graduate advisors Brenda Jean P. Larson and Jennifer Huberman for their advising and help in my Ph.D. program. I thank UW copyright librarian Maryam Fakouri for providing me with very detailed advice on properly citing papers in this thesis.

During my Ph.D. program, I had 2 internships in the industry. I value my first internship experience in MathWorks. I thank my host, Dr. Colin McGuire, in MathWorks for hiring

me and providing me a daily supervising and help. We worked remotely and had a large time difference, but that didn't make our remote work difficult. I also thank Dr. McGuire for his code support in my ns-3 projects. I also value my second internship experience in Mitsubishi Electric Research Laboratories (MERL). I thank my host, Dr. Pu Wang, in MERL for hiring me and providing me a lot of advice on radar signal processing including time-frequency analysis and MIMO radar signal processing. My work in MERL constitutes a large part of my Ph.D. thesis, and I really thank Dr. Wang's instruction.

I thank my colleagues, Yaping Sun, Xiangyu Gao, Weihua Jiang, Jun Hyeon Park, Xuhang Ying, Lyutianyang Zhang, Hao Yin, Liu Cao, Collin Brady, Yonghun Lee, and Sachin Nayak, at my UW lab for their collaboration and help when I'm in Seattle. I thank my colleague, Yuchen Liu, at Georgia Tech, for discussing with him on ns-3 related projects and our career development. I thank my colleagues, Faisal Darbari and Honglei Chen, at MathWorks for their instructions and help on my MATLAB coding and system building. I thank my colleagues, Yuying Liu, Dayu Zhu, and Zejiang Wang, at MERL for their suggestions and accompany when I was in Boston.

I give my sincere appreciation to my parents and grandparents for supporting me and encouraging me to finish my Ph.D. program. I would also give my special thanks to all of my roommates, Yuying Liu, Chien-Yu Lin, Ting Huang, Yuxi Jin, Wenzhe Zhang, Meng Tian, Shixin Huang, Xiaowei Tan, and Yang Su, for their help in my daily life at the US. I thank one of my best friends, Yannan Liu, for his consistent help and accompany. I also thank my other friends including but not limited to Baicen Xiao, Yue Sun, Yihan Jiang, Yize Chen, Yue Yang, Haiyang Zhang, Xiao Lin, Wenjun Guo, Keyu Li, Jiaxin Shi, Roy Lu, Mingzhe Chen, Litai Kang, Peipei Han, Xin Han, Ao Wang, Xiahan Zhang, Addison Lin, Xu Guo, Xiaochuang Yuan, Tony Fei, Chumei Yang, Ellen Chin, Daniel Chin, Danny Geng, Kenan Lv, Qiao Cui, Yuyang Wang, Esther Chen, Calvin Wu, Sarah Zhou, Yajun Wu, Mengjia Cen, Liang Xiang, Chuanhai Zhang, Yan Su, Jianming Kang, Jian Lou, Yuge

Tang, Victor Hsiao, Judy Yang, Sabrina Wang, Feilong Wang, Zili Wang, Xiaoxiao Jia, Peng Cui, Chaofeng Liu, Jialin Gao, Zhiping Chu, Canglong Cai, Yunyi Yang, Dechun Song, E Wang, Wenying Luo, Fengyi Sun, Qi Guo, Jirong Wang, Anhua Chen, Fang Ding, Jie Ying, Zhien Wang, Haiqing He, Shudi Xu, Yuanhao Li, Hua Zhou, Zhe He, Mingjia Zou, Peitong Xue, Tianchi Yao, Peng Liu, Xianjie Zhang, Xinrui Zhao, Yang Chen, Eric Ma, Senlin Liu, Xujie Chen, Mingrui Yu, Xin Ji, Yung-Hsu Liu, Joy, Colive, Emily, Jiali Huang, Hongbo Chen, Thomas Tang, Yanting Zhang, Yizhou Wang, Haotian Zhang, Jiarui Cai, Ruiyi Chen, Hui Ren, Tingting Shi, Wentao Luan, Changfu Ding, Jiqi Zheng, Jinxing Mao, Guchong Li, Chaofan He, Dongdong Jiang, Chenjun Guo, Hao Feng, Zhanzhan Zhang, Junfeng Guo, Jifang Xing, Wanli Wen, Yunlong Gao, Wei Xu, Kaixuan Long, Qi Wang, Zhan Wang, Chen Feng, Zitian Wang, Yanchang Guo, Zulian Liang, Tingyou Li, Guyi Chen, Tao Wang, etc.

DEDICATION

to my dear mom, dad and grandparents

Chapter 1

INTRODUCTION

1.1 Background

Automotive radars are increasingly becoming a commodity in support of various safety-enabling driver-assistive functions, based on estimating the relative range and radial velocity to targets (vehicles, pedestrians, etc.) [49]. Compared to other automotive sensors, radar is strong at operating in adverse weather and night, and also has low cost and processing overhead [3]. As intelligent vehicles are equipped with more and more radar sensors for full-view, all-weather perception, new signaling schemes such as phase modulated continuous wave (PMCW) [27] and orthogonal frequency-division multiplexing (OFDM) [6] have shown better capabilities than the traditional frequency modulated continuous wave (FMCW) scheme, at a price of significantly higher sampling rates and increased requirements for transceiver hardware [33, 73, 74]. Nevertheless, the FMCW scheme remains the mainstream option to achieve full four-dimensional (range-velocity-azimuth-elevation) automotive radar with a sub-degree angular resolution at a mass production level.

Compared to other automotive sensors like cameras and lidars, the main drawback of radar is its angle resolution [3]. For achieving high angular resolution while maintaining low cost and low processing overhead, multiple-input multiple-output (MIMO) radar technology has been proposed to synthesize a large virtual array using limited transmit (Tx) and receive (Rx) antenna chains [61]. For example, if the Tx and Rx arrays are uniform linear arrays (ULAs), a MIMO radar with N Rx elements of spacing d_r and M Tx elements of spacing Md_r can synthesize a virtual Rx ULA with MN elements of spacing d_r [61][1].

---

[1] In a MIMO radar system, each element of the Tx array transmits an orthogonal waveform. Because of this orthogonality, it is possible to recover the Tx signals at the Rx array [43]. The measurements at the physical Rx array corresponding to each orthogonal waveform can then be stacked to form the

This requires the signals from different Tx antennas are separated at each receive antenna, which can be realized using slow-time time-division multiplexing (TDM), slow-time linear code based Doppler-division multiplexing (DDM), and slow-time pseudo-random phase code based DDM [61]. The low-cost high-resolution implementation makes MIMO-FMCW radars the state-of-the-art high-resolution automotive radars [49, 61]. As a natural extension, the next-generation MIMO radar is the massive MIMO radar [22], which has a large virtual array size. The massive MIMO radar can improve angle of arrival detection performance [22], and can be foreseen to be used in automotive radar in the near future.

FMCW radars transmit chirps (linear frequency modulated signals) [6, 50] on radio frequency (RF) band. With the growing density of vehicular FMCW radars, multiple co-channel radars may cause mutual interference. In this case, the received signal at a victim radar is a superposition of the desired targets' echoes and undesired interference from other simultaneously active co-channel radars. Such mutual radar interference can potentially degrade radar detection and estimation performance [12][2].

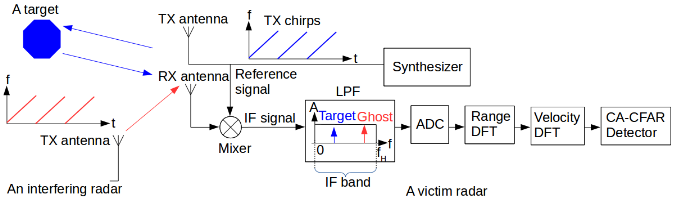

Figure 1.1: A typical transceiver block diagram of an single-input single-output (SISO)-FMCW radar in a coherent interference scenario. (© 2021 IEEE)

The interference at a victim radar receiver can be classified into coherent and incoherent interference [6, 14, 55, 75]. Coherent interference is generated when all radars have identical

---

measurements of the virtual array. As each of the N Rx elements can receive M orthogonal waveforms, the virtual array can maximally separate MN different Rx signals.

[2] Besides mutual radar interference, an FMCW radar's receiver may also suffer from the high-power near-DC self-interference/leakage from its transmitter via a direct path [61]. Such a self-interference can be suppressed by using a DC canceler [6] and is out of the scope of this thesis.

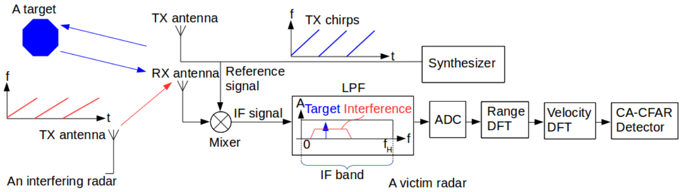

Figure 1.2: A typical transceiver block diagram of an SISO-FMCW radar in a incoherent interference scenario. (© 2021 IEEE)

chirp parameters (chirp slope, chirp bandwidth, pulse repetition period), while incoherent interference is generated when the victim radar and the interfering sources have different chirp parameters [6]. The coherent interference can happen when interfering radars operating at the same band come from the same manufacturer as the victim radar. The incoherent interference is more common because it's more likely that different radars come from different manufacturers or come from the same manufacturer but in different applications (e.g., long-range radars and short-range radars have different chirp parameters). At the victim radar's intermediate frequency (IF) band, coherent interference creates ghosts, i.e., fictitious targets (see Figure 1.1) that appear at random ranges [75], causing false alarms, and incoherent interference appears as a noise floor elevation (see Figure 1.2), which also impacts target detection performance [6][3].

To deal with mutual FMCW radar interference, mutual interference mitigation (MIM) has received attention over past few years. Recent developments can be divided into several categories: 1) fast-time domain[4] MIM [8, 11, 18, 30, 41, 47, 57, 69, 71, 72] such as interference-

---

[3] Notice that whether the interference causes ghosts or noise floor elevation at the IF band is the key for differentiating coherent interference or incoherent interference. The ghosts occur when the interfering radar adopts the same chirp slope, chirp bandwidth, and pulse repetition period as the victim radar [6]. The definition of coherent interference is independent of the initial phase offset between the interfering radar and the victim radar, as the initial phase offset between the two radars does not change ghosts into noise floor elevation, and vice versa.

[4] Fast-time domain samples refer to the samples from a single chirp cycle [56].

zeroing [8], adaptive noise cancellers [30] and sparse sampling [11]; 2) slow-time domain[5] MIM such as non-linear filtering [70], whitening [67], and slow-time generative adversarial network [17]; 3) range-velocity (RV) domain MIM [20,23,29,58] that directly treats the RV heatmap as an image and trains neural networks as a denoiser (such as convolution-based autoencoder) to remove the interference; 4) spatial domain MIM such as beamforming [9, 10,16,21,52,53] and slow-time MIMO radar code design [13]; 5) communication-assisted MIM [7,44]. Performance evaluation of a set of MIM methods can be found in [66] and [68].

Despite these prior arts, there are still some important problems in this field that have not been well investigated. First, as noted by the recent survey [3], very few prior works have analyzed the radar performance in mutual interference. A comprehensive study and evaluation of these schemes are still missing. Second, existing fast-time domain mutual interference mitigation schemes may not achieve good performance under strong incoherent interference, as will be shown in this thesis. Third, there is no interference signal formulation of the state-of-the-art MIMO-FMCW radar. The radar angle detection is easily impacted by mutual radar interference under the widely-adopted classic correlation scheme, as will be shown in this thesis. Thus, advanced signal processing methods based on the MIMO-FMCW interference signal modeling are very important but are missing. Fourth, for the next-generation massive MIMO radar [22], the analysis of its advantage on mutual automotive radar interference mitigation is also missing.

1.2 Summary of Research Contributions

We consider handling both the coherent mutual FMCW radar interference issue and the incoherent mutual FMCW radar interference issue in this thesis. To solve the coherent and incoherent interference issues, we propose different schemes operating within the time-scale of a coherent processing interval (CPI) [6].

---

[5] Slow-time domain samples refer to the samples across multiple chirp cycles [56].

[6] A CPI is the time of a series of slow-time pulses collected for measuring targets' ranges, velocities, and angles, assuming the radar and the targets do not move significantly during this interval [56].

We first consider the coherent mutual FMCW radar interference issue. To analyze the radar detection performance under coherent interference, we define two cross-layer metrics to quantify network performance: target misdetection probability and multiple access capacity. The multiple access capacity is defined as the average density of radars that can operate without false alarms caused by coherent interference. We consider 4 different multiple access schemes combined with slow-time domain signal processing. We comprehensively analyze the cross-layer performance of the FMCW radar coherent interference network under the 4 multiple access schemes using the two metrics. Via our analysis, we show that even without synchronization and coordination, some proper multiple access schemes can achieve very large multiple access capacities while maintaining low target misdetection probabilities.

We next consider the incoherent mutual FMCW radar interference issue. To improve range-velocity detection under incoherent interference, we first understand the target with incoherent interference from the fast-time domain. We find dechirped target signals are single tone signals while dechirped interference signals are still FMCW signals and can vary from pulse to pulse. These interference can significantly raise noise floor at the victim radar's IF band. The state-of-the-art solutions include zeroing out interference in the fast-time domain [8, 71] of the received IF signal. These schemes require interference detection. However, as the parameters (e.g., slopes and time durations) of different interference signals can be different, the interference detection is usually not very robust and can leave a lot of interference residuals. To deal with the drawback of the previous interference detection and cancellation schemes, we propose to try a different approach. The idea is given as follows. In the same CPI, the targets' frequencies are the same, and they are represented as the horizontal lines on the time-frequency representation. So, our idea is to identify these horizontal lines on the time-frequency domain and directly recover this portion. We name this method fast-time-frequency mode reconstruction (fTFMR). We show that the proposed fTFMR can achieve a much better range-velocity detection performance compared to the state-of-the-art fast-time domain schemes under strong interference.

To improve spatial detection under incoherent interference, we consider proposing a novel detection scheme for MIMO-FMCW radar in the angle domain. One of the most important contributions here is that we are the first to derive the interfered signal model in the existence of mutual MIMO-FMCW interference and formulate a hypothesis testing problem considering the interference structure. We solve the hypothesis testing problem using the generalized likelihood ratio test (GLRT) principle and obtain a subspace-based detector that suggests an interference cancellation solution. We analyze the performance of the proposed spatial detector for MIMO-FMCW radar and show that the proposed spatial detector is a constant false alarm rate (CFAR) detector. Our another original contribution is extending our analysis to next-generation massive MIMO radar with a large virtual array [22]. Via our analysis, we show that increasing the antenna array size can suppress interference. We validate the effectiveness of the proposed subspace-based detector and massive MIMO for interference mitigation in MATLAB Phased Array System Toolbox.

1.3 Thesis Outline

The remainder of this thesis is organized as follows. In Chapter 2 of this thesis, we adopt slow-time domain multiple access schemes to mitigate coherent interference. In Chapter 3 of this thesis, we use fast-time domain mode reconstruction to mitigate incoherent interference and improve the detection performance in the range-velocity (Doppler) domain. In Chapter 4 of this thesis, we use spatial domain MIMO detector and massive MIMO to mitigate incoherent interference. This thesis includes the material in the author's previous papers published on IEEE [31–33], one paper accepted by IEEE [34], and two papers to be submitted to IEEE [35, 36][7].

---

[7] In reference to IEEE copyrighted material which is used with permission in this thesis, the IEEE does not endorse any of University of Washington's products or services. Internal or personal use of this material is permitted. If interested in reprinting/republishing IEEE copyrighted material for advertising or promotional purposes or for creating new collective works for resale or redistribution, please go to http://www.ieee.org/publications_standards/publications/rights/rights_link.html to learn how to obtain a License from RightsLink. If applicable, University Microfilms and/or ProQuest Library, or the Archives of Canada may supply single copies of the dissertation.

1.4 Conventions and Notations

Throughout this thesis, we use $(\cdot)^T$ to represent transpose, use $(\cdot)^*$ to represent conjugate, and use $(\cdot)^H$ to represent conjugate transpose. We use $\mathbf{P}_{\mathbf{H}}^{\perp} \triangleq \mathbf{I} - \mathbf{H}(\mathbf{H}^H\mathbf{H})^{-1}\mathbf{H}^H$ to denote the projection matrix projecting to the space orthogonal to that spanned by the columns of $\mathbf{H}$. $Q_1(\cdot,\cdot)$ denotes the Marcum Q function of order 1 [62].

Chapter 2

MULTIPLE ACCESS SCHEMES FOR MITIGATING COHERENT INTERFERENCE

2.1 Motivation

Media access control (MAC) techniques in the time, frequency, and coding domains are widely adopted to deal with coherent interference [3, 6, 7, 28, 38, 42, 45, 55, 59, 63, 75]. Radar MAC designs are based on centralized [38, 45, 75] or distributed [7, 42, 55, 63] protocols. The schemes in [7, 38, 45] realize MAC scheduling using GPS for time synchronization or position updates, additional communication channels and control messages. However, such standardization requirements are undesirable for existing non-cooperative radars [28]. In [7, 38, 75], time-synchronous schemes aiming at achieving orthogonal access are proposed. A challenge in time-synchronous orthogonal scheduling is that the interference propagation delay, typically in the order of chirp duration (microseconds [19]), can deteriorate orthogonality significantly. Even if two radar sources are synchronously and orthogonally scheduled with different transmit start instants, the receiver of the reference radar may experience interference from the other source due to the random interference propagation delay caused by relative random position. Thus, the MAC protocols in [6, 7] separate transmit start instants of different radars beyond maximum interference propagation delay to achieve guaranteed orthogonal scheduling, which can be inefficient.

In this chapter, we focus on distributed MAC protocols that are operated without any time synchronization and cooperation. The underlying motivation is analyzing asynchronous distributed MAC protocols for multi-radar operations with a view to characterizing the pros and cons of various designs. As noted by the recent survey [3], very few prior works have analyzed the radar performance in mutual interference. [39] studies interference between one pair of radars using a pure physical (PHY) layer analysis without considering radar network aspects. [2] adopts stochastic geometry methods for modeling aggregate radar interference, while the PHY layer signal characteristics are not captured. [55, 75] constitute early work that considered both waveform (chirp) structure and network aspects to capture the interference probability at a victim radar. While [55, 75] broadly conclude that the interference probability is low for a pure random access scheme, they do not quantify this probability in terms of target detection performance and false alarm performance under different radar densities. In this chapter, we define two *cross-layer* metrics to quantify network performance: target misdetection probability and multiple access capacity. The multiple access capacity is defined as the average density of radars that can operate without false alarm caused by coherent interference. In contrast with the conclusions in [55, 75], our analysis shows that a pure random access scheme like un-slotted ALOHA (UA) with random frequency division multiplexing (RFDM), achieves a poor trade-off between multiple access capacity and probability of target misdetection even in a low radar density regime. To improve this trade-off, we adopt frequency hopping (FH) [42, 59] and phase coding (PC) [55, 63, 75] as potential enhancements. Our analysis shows that even without synchronization and coordination, UA along with FH and PC improve operational trade-off by significantly increasing the multiple access capacity. This can be explained by the *detect-and-classify* principle introduced later, which provides potential guidance for future standardization activities.

Major materials of this chapter is presented the author's previous publication [32, 33][1].

2.2 FMCW PHY Layer under Coherent Interference

We now review the signal processing flow for an FMCW radar complex baseband transceiver chain [55] and illustrate the impact of coherent interference. As shown in Figure 1.1, FMCW radars periodically transmit a sequence of chirps [49] and receive a delayed version of the transmitted chirps. If the transmitted chirp signal is backscattered from a target at a distance

---

[1] © 2020 - 2021 IEEE. Reprinted, with permission, from [32, 33].

of d meters, the round-trip delay for receiving the target's echo is $\frac{2d}{c}$, where c is the speed of the light [54]. The received target echo is then mixed with the output of the local FMCW synthesizer (the reference signal), which is called dechirping, to generate the IF signal - a single tone whose frequency equals to the round-trip delay $\frac{2d}{c}$ multiplied by the chirp slope h [54]. The resulting single tone signal is then passed through a low pass filter (LPF) with cutoff frequency f_H chosen for anti-aliasing and eliminating out-of-band interference. If the echo from the target at distance d passes the LPF, then its IF signal frequency $\frac{2dh}{c} \leq f_H$. Similarly, if the delayed same-slope interference chirp is de-chirped and passes through the LPF of the victim radar, the resulting single-tone IF signal looks like a de-chirped target echo and appears as a ghost (see Figure 1.1). The low-pass filtered signals are sampled by an analog-to-digital converter (ADC) and processed using discrete Fourier transform (DFT) for subsequent range and velocity estimation.

To estimate the target range d, each radar estimates IF frequency of the target $\frac{2dh}{c}$ using DFT - hence called range DFT. The maximum detectable range $d_{t,max} = \frac{f_H c}{2h}$ corresponds to a radar-target pair such that the target's IF signal just falls inside the radar's LPF passband cutoff. The range resolution - the minimum distance that a DFT based range estimation algorithm can resolve - is $d_{res} = \frac{c}{2B_c}$ [54], where B_c is the chirp bandwidth. This partitions the maximum detection range into $N = \frac{d_{t,max}}{d_{res}}$ range bins (see Figure 2.1), or equivalently, partitions the IF band of bandwidth f_H into N frequency bins of bandwidth $\frac{f_H}{N}$ (frequency resolution). As shown in Figure 2.1, the peak of each dechirped target or ghost will appear in one range bin. Note that the above range estimator is feasible when the transmit start instant of the radar's chirp is known. Unlike measuring the range of targets, measuring ranges of interferers (or propagation delay of interference) is non-trivial because the transmit start instants of interference is unknown at the victim radar, even if ghosts were identified.

For a target moving with relative velocity v over a chirp transmission period T_g, the relative motion $\Delta d = T_g v$ is typically sufficiently small to keep the target in the same range bin. The corresponding phase difference between two consecutive range measurements is $\Delta\Phi = 2\pi f_c \frac{2\Delta d}{c}$ [25], where f_c is the chirp's central frequency. Over L such chirp cycles, if

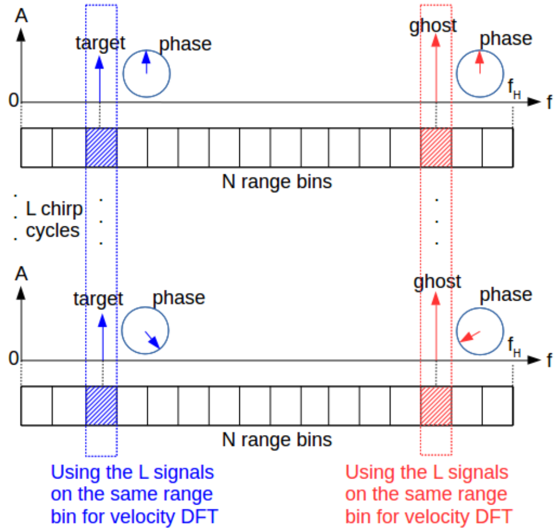

Figure 2.1: Signals over L chirp cycles (a CPI) on the same range bin are used for velocity DFT. (© 2021 IEEE)

the velocity of the target remains nearly constant, the target phase in the same range bin increases linearly with $\Delta\Phi$ per chirp cycle. Then, using the DFT on the L signals in the same range bin yields an estimate of $\Delta\Phi$ (see Figure 2.1), which in turn can be used to estimate the velocity v [54] - hence such DFT is called velocity DFT. The L chirp cycle time $T_f = LT_g$ for a single velocity estimation is called coherent processing interval (CPI) [63]. The corresponding maximum detectable relative velocity $v_{t,max} = \frac{c}{4f_cT_g}$ [59] and the velocity resolution resolvable by DFT is $v_{res} = \frac{c}{2f_cT_f}$ [59]. This partitions the maximum relative velocity into $\frac{v_{t,max}-(-v_{t,max})}{v_{res}} = L$ velocity bins. Above range DFT and velocity DFT form the 2D N-by-L range-velocity bins shown in Figure 2.2. The outputs on the range-velocity bins are fed into the cell-averaging constant-false-alarm rate (CA-CFAR) detector for detecting signal peaks [49]. From Figure 2.1 and Figure 2.2, we can see that after range-velocity DFT, a ghost may lead to a false target and causes false alarm after CA-CFAR detection. If a target and an interference signal are well separated on different range-velocity bins, the target can be correctly detected. However, if a target and a strong interference signal fall into adjacent bins, the side-lobe of the interference may cause target misdetection.

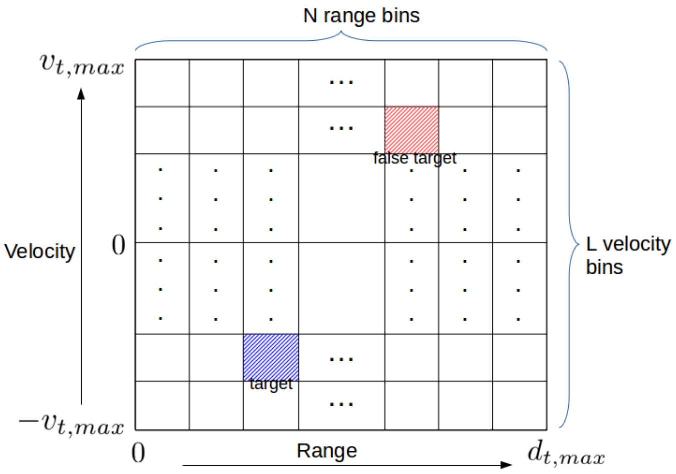

Figure 2.2: 2D range-velocity bins. (© 2021 IEEE)

2.3 *Radar Interference Model and Performance Metrics*

In this section, we propose a radar interference model and performance metrics for analyzing the considered MAC schemes. As shown in Figure 2.3, single SISO-FMCW radar-equipped vehicles distribute on an infinitely long single-lane road following 1D homogeneous Poisson point process (PPP) with density λ. We collect the first order PHY layer assumptions for our subsequent analysis as follows.

- Assumption 1: All radars are identical with the same chirp bandwidth B_c, chirp slope h, transmit period T_g, cutoff frequency f_H of IF section, transmitter power P_t and transmit (receive) antenna gain $G_t(G_r)$. All targets have the same radar cross-section (RCS) σ. For target at distance d, the received target power P_r follows the mono-static radar equation [6]

$$P_r = \frac{P_t G_t G_r \sigma c^2}{(4\pi)^3 f_c^2 d^4}. \tag{2.1}$$

- Assumption 2: The total system RF band is divided into M sub-bands, each of bandwidth B_c that is equal to the chirp bandwidth.

- Assumption 3: Noise power at IF band is negligible.

The same slope assumption implies that an interfering radar's signal being de-chirped into the victim FMCW radar's IF band appears as a ghost [14, 55], as shown in Figure 1.1[2]. Furthermore, as range resolution $d_{res} = \frac{c}{2B_c}$ of each radar is expected to be sufficiently small, chirp bandwidth B_c has a lower bound. Thus, for fixed total system bandwidth, the number of sub-bands M in Assumption 2 cannot be too large. The noise-free assumption in Assumption 3 allows us to ignore the false alarm and target misdetection caused by noise, and focus exclusively on radar mutual interference.

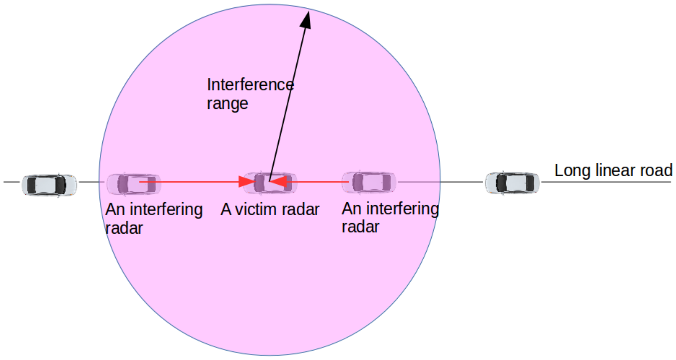

Figure 2.3: Radar interference scenario with unit-disk interference model. (© 2021 IEEE)

We only consider the line-of-sight (LOS) interference as in [3, 6], as non-LOS interference

---

[2] While our analysis later is based on the ideal (single-tone) ghost assumption, different radar oscillators may lead to slight slope differences [55] between different radars, causing the ghost to expand on the IF band. However, [24] indicates that current FMCW oscillators can achieve within 1 ppm frequency accuracy, such that the maximum relative clock drift between any two radars is $\delta_{\max} = 2 \times 10^{-6}$ [55]. Using such high-accuracy FMCW radar oscillators, the maximum dechirped interference bandwidth $h\delta_{\max}T_c$ is far less than the frequency resolution f_H/N under the setup in Table 2.1. Thus, these relative clock drift between different radar oscillators cannot cause discernible expansion on the ghosts, and our ideal ghost assumption still holds.

is much weaker [6]. For interference at range d_i, the received interference power P_{int} is determined by the free-space path-loss (Friis) formula [14]

$$P_{int} \triangleq \frac{P_t G_t G_r c^2}{(4\pi)^2 f_c^2 d_i^2}. \tag{2.2}$$

Thus, the maximum propagation range of LOS interference is $d_{Friis}^{max} = \left(\frac{P_t G_t G_r c^2}{(4\pi)^2 f_c^2 P_r^{min}}\right)^{1/2}$, where P_r^{min} the minimum receive power. By [50], $P_t = 12$dBm, $G_t = G_r = 12$dBi, $P_r^{min} = -128$dBm, $f_c = 77$GHz, we have $d_{Friis}^{max} = 49.1$km. Such a large d_{Friis}^{max} value is an over-estimate, as interference signals cannot propagate over such ranges without blockage in most realistic scenarios. Following a large body of prior work in vehicular networking [1] (and references therein) and ignoring the effect of directional antenna beams for simplicity, we adopt a unit-disk interference model. As shown in Figure 2.3, the unit-disk interference model defines the interference range $d_{i,max}$ - the maximum distance that can cause interference to a victim receiver. Typically, $d_{i,max} \ll d_{Friis}^{max}$ and $d_{i,max} \ll cT_g$. For example, if $d_{i,max} = 1000$ m and $T_g = 55$ us [19], then $\frac{d_{i,max}}{c} = 3.33$ us $\ll T_g$. Any interfering radar inside the victim radar's interference range ($d_i < d_{i,max}$) contributes LOS interference following Friis formula in (2.2) [14]; otherwise, the interfering radar contributes no interference.

Note that an interfering radar's presence within a victim radar's interference range does not necessarily imply that the interfering radar leads to a ghost at the range bin of the victim radar. This is determined by two further conditions:

a) Frequency condition: At chirp cycle y, the interference causes a ghost at a range bin of the victim radar only if the two radars transmit on the same sub-band. We denote the event that radar k and radar 0 transmit on the same sub-band at chirp cycle y as $F_{k,0}^{y}$.

b) Time condition: Suppose an interfering radar k falls into a reference radar 0's interference range. Let t_0 (t_k) denote the transmit start instant of radar 0 (radar k), and hence $\Delta t_{k,0} = t_0 - t_k$ is the difference of the transmit start instants. Let $d_{k,0}$ denote the distance between the two radars. As shown in Figure 2.4, the interfering chirp of radar k is dechirped by reference radar 0 and falls in radar 0's n-th range bin, only if the following time condition

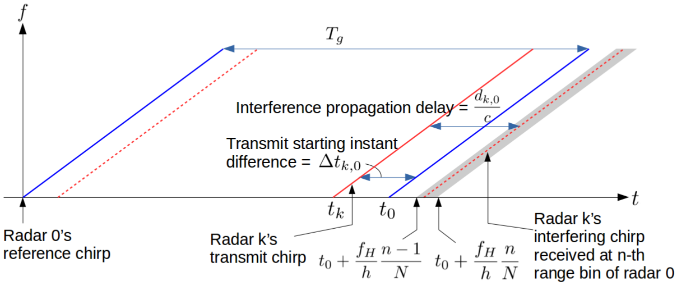

Figure 2.4: Time condition for radar k's interfering chirp falling into radar 0's n-th range bin. (© 2021 IEEE)

$G^n_{k,0}$ is met:

$$t_0 + \frac{f_H}{h}\frac{n-1}{N} \le t_k + \frac{d_{k,0}}{c} < t_0 + \frac{f_H}{h}\frac{n}{N}, \tag{2.3}$$

where $\Delta t_{k,0} \in [-\frac{f_H}{h}, T_g - \frac{f_H}{h}]$, and $d_{k,0} \in (0, d_{i,max}]$. It suffices to consider a single chirp repetition interval T_g, since the maximum interference propagation delay $\frac{d_{i,max}}{c} \ll T_g$. Figure 2.4 and (2.3) imply two important results. First, time-domain interference avoidance by synchronous scheduling t_0, t_k for two sources is challenging because $d_{k,0}$ is random and unknown. Second, pure random access implies random t_k that in turn places ghosts randomly in victim radars' range bins [75]. In this case, false alarms can appear on any range bins. In addition, a ghost typically has larger power than a target (indicated by (2.1) and (2.2)), and its side-lobe or ghost-spread pseudo-noise can lead to target misdetection. We formally define false alarm and target misdetection as follows.

False alarm event $E^{n,l}_{fa,k,j}$ occurs if radar j's detector detects a peak at its range-velocity bin (n, l) caused by the interference from radar k, given that a target does not exist in the range-velocity bin (n, l). The false alarm event caused by radar k at radar j is thus $E_{fa,k,j} = \bigcup_{n=1}^{N} \bigcup_{l=1}^{L} E^{n,l}_{fa,k,j}$. ◊

Target misdetection event $E^{n,l}_{md,k,j}$ occurs if radar k's ghost at range bin n renders a target at radar j's range-velocity bin (n, l) to be un-detected. The target misdetection event caused by radar k at radar j's range bin n is thus $E^n_{md,k,j} = \bigcup_{l=1}^{L} E^{n,l}_{md,k,j}$.

We define the target misdetection event for each range bin n because it depends on the power of the target return for that range bin. In contrast, as we'll see in the proof of Proposition 1, the ghost power under the considered MACs is independent of range bin indices, and hence it is easier to analyze the joint false alarm event $E_{fa,k,j}$. We denote the set of radars falling into radar j's interference range as $\mathcal{K}_j$. Then, radar j encounters a false alarm with probability $\mathbb{E}_{\mathcal{K}_j}\left[\Pr\left[\bigcup_{k\in\mathcal{K}_j} E_{fa,k,j}|\mathcal{K}_j\right]\right]$, and suffers target misdetection at range bin n with probability $\mathbb{E}_{\mathcal{K}_j}\left[\Pr\left[\bigcup_{k\in\mathcal{K}_j} E_{md,k,j}^{n}|\mathcal{K}_j\right]\right]$.

A MAC scheme is fair if all victim radars have the same false alarm probability

$$\Pr\left[E_{fa}\right] = \mathbb{E}_{\mathcal{K}_j}\left[\Pr\left[\bigcup_{k\in\mathcal{K}_j} E_{fa,k,j}|\mathcal{K}_j\right]\right],$$

and the same target misdetection probabilities

$$\Pr\left[E_{md}^{n}\right] = \mathbb{E}_{\mathcal{K}_j}\left[\Pr\left[\bigcup_{k\in\mathcal{K}_j} E_{md,k,j}^{n}|\mathcal{K}_j\right]\right], n = 1, 2, \ldots, N.$$

The multiple access capacity of a fair MAC

$$C \triangleq \lambda\left(1 - \Pr\left[E_{fa}\right]\right) \tag{2.4}$$

is average number of non-false-alarmed radars per meter.

The target misdetection probability and the multiple access capacity are two proposed metrics for evaluating the cross-layer performance of fair radar MACs. As the false alarm is the main issue under coherent interference, the multiple access capacity is defined to capture the false alarm probability only to emphasize the importance of the false alarm probability under coherent interference. Like in the traditional detection theory [37], which separately evaluates the detection probability and the false alarm probability in the physical layer, we also separately evaluate the target misdetection probability and the multiple access capacity in the cross-layer performance analysis.

Suppose each target independently and randomly falls into one of the range-velocity bins. Also, suppose the radars in $\mathcal{K}_0$ independently cause target misdetection and false alarm at a reference victim radar 0. Based on these assumptions, we analyze the target misdetection probabilities and the multiple access capacity of four distributed fair radar MACs in the following sections.

2.4 UA-RFDM

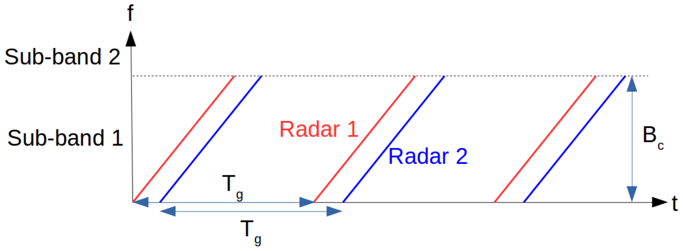

Figure 2.5: UA-RFDM with 2 radars independently choosing sub-band 1. (© 2021 IEEE)

To deal with coherent interference, we first consider the simplest distributed MAC – un-slotted ALOHA with random frequency division multiplexing (UA-RFDM) shown in Figure 2.5. This MAC, based on the well-known un-slotted ALOHA (UA) [40], has a key characteristic that each radar's initial chirp transmission time is random, and after that, each radar transmits periodically with a fixed inter-chirp duration T_g. We combine UA with random frequency division multiplexing (RFDM), whereby each radar independently and randomly transmits on one of the multiple sub-bands over a CPI and the initial chirp phases of each radar are the same over a CPI. The resulting MAC does not require any time synchronization and control overhead.

We now consider the simplest random access protocol: UA-RFDM, which operationally requires no changes to a typical FMCW radar in Figure 1.1. To understand the conditions for false alarm $E_{fa,k,j}$ and target misdetection $E^n_{md,k,j}$, $n \in \{1, 2, \ldots, N\}$, we first run simulations for UA-RFDM under the setup in Table 2.1.

Our simulations show that a ghost in a range bin always leads to a false alarm (a false target and a high-power interference side-lobe) on at least one range-velocity bin (see two examples in Figure 2.6 and Figure 2.7). Thus, if radar k falls into the interference range of radar 0, and the time and frequency conditions are satisfied, radar k causes false alarm at radar 0. That is, if $k \in \mathcal{K}_0$, then $E_{fa,k,0} = F_{k,0}^1 \cap \left(\bigcup_{n=1}^N G_{k,0}^n\right)$.

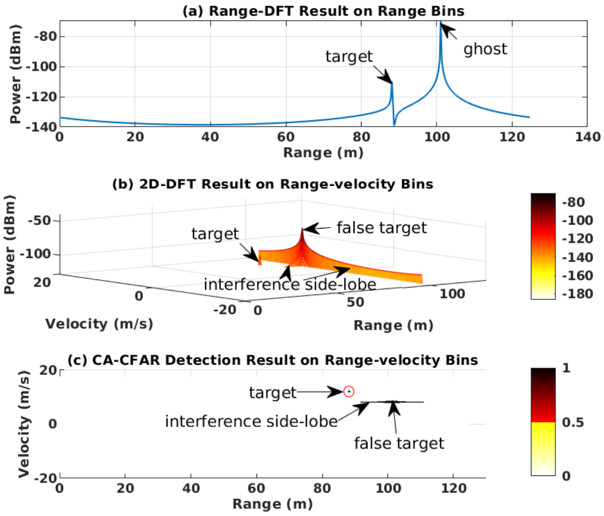

Figure 2.6: PHY layer simulation under UA-RFDM with 1 target (real range: 88.13m, real velocity: 12.10m/s) falls into range bin $n = 318$ (88.06m - 88.33m) and 1 ghost (real range: 60m, real velocity: 16.40m/s) falls into range bin $n = 365$ (101.39m - 101.67m). (© 2021 IEEE)

As shown in Figure 2.7, when a high-power ghost and a target fall into the same range bin, the target after velocity DFT may be mis-detected due to the interference side-lobe. At radar 0's range bin n, the target misdetection caused by radar k happens if and only if the following two events occur. (a) The range $d_{k,0}$ between radar k and radar 0 is smaller than a range bin dependent threshold r_n, and we denote such event as $R_{k,0}^n$. (b) As shown in Figure 2.7, on range bin n, a target can be misdetected only when it falls into certain velocity bins near a false target, which happens with probability p_n. We let $I_{k,0}^n$ denote the event that at least one target falls into such velocity bins. Then, conditioned on $k \in \mathcal{K}_0$, we model $E_{md,k,0}^n = F_{k,0}^1 \cap R_{k,0}^n \cap G_{k,0}^n \cap I_{k,0}^n$. Focus on analyzing the performance of a reference

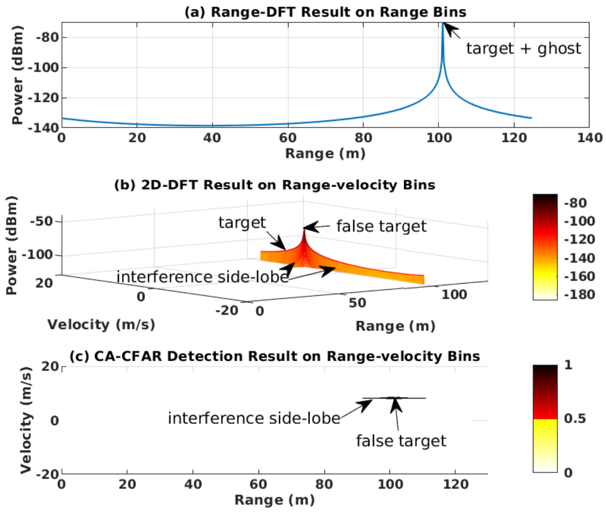

Figure 2.7: PHY layer simulation under UA-RFDM with 1 target (real range: 101.50m, real velocity: 12.10m/s) and 1 ghost (real range: 60m, real velocity: 16.40m/s) fall into the same range bin $n = 365$ (101.39m - 101.67m). (© 2021 IEEE)

victim radar 0, we have the following result.

Proposition 1 (PHY and MAC Layer Properties of UA-RFDM) *UA-RFDM is a fair MAC with target misdetection probability at range bin* n

$$\Pr\left[E^n_{md}\right] = 1 - \exp\left[-\frac{2\lambda r_n f_H/h}{MNT_g}\left(1-(1-p_n\frac{1}{N})^x\right)\right], \tag{2.5}$$

and multiple access capacity

$$C_{UA-RFDM} = \lambda \exp\left[-2\lambda d_{i,max}\frac{f_H/h}{T_g M}\right], \tag{2.6}$$

conditioned on the number of targets seen by each radar is x.

Proof 1 *Under RFDM, we have* $\Pr\left[F^1_{k,0}\right] = \frac{1}{M}$. *As radar topology is homogeneous, we have* $\Pr\left[R^n_{k,0}\right] = \frac{r_n}{d_{i,max}}$. *Under UA, for a fixed* t_0 *(radar* 0*'s transmit start instant is known by itself), we have* $\Delta t_{k,0} = t_0 - t_k \sim U[-\frac{f_H}{h}, T_g - \frac{f_H}{h}]$. *By the uniform distribution of* $\Delta t_{k,0}$

and (2.3)*, we have* $\Pr\left[G^n_{k,0}\middle|k\in\mathcal{K}_0\right]=\frac{f_H/h}{NT_g}$*,* $\forall n\in\{1,2,\ldots,N\}$*. This implies that the ghost power is the same for all range bins. As each target independently and randomly falls into one of range-velocity bins,* $\Pr\left[I^n_{k,0}|F^1_{k,0},R^n_{k,0},G^n_{k,0}\right]=1-(1-p_n\frac{1}{N})^x$*. Thus,*

$$\Pr\left[E^n_{md,k,0}|k\in\mathcal{K}_0\right]=\Pr\left[F^1_{k,0},R^n_{k,0},G^n_{k,0},I^n_{k,0}|k\in\mathcal{K}_0\right]=\frac{r_nf_H/h}{d_{i,max}MNT_g}\left(1-(1-p_n\frac{1}{N})^x\right),$$

and

$$\Pr\left[E_{fa,k,0}\middle|k\in\mathcal{K}_0\right]=\Pr\left[F^1_{k,0},\bigcup_{n=1}^{N}G^n_{k,0}\middle|k\in\mathcal{K}_0\right]=\frac{f_H/h}{MT_g}.$$

By assumption, the radars in $\mathcal{K}_0$ *independently cause target misdetection and false alarm at radar* 0*. Thus,* $\Pr\left[\bigcup_{k\in\mathcal{K}_0}E^n_{md,k,0}\middle||\mathcal{K}_0|=K_0\right]=1-\left(1-\frac{r_n}{d_{i,max}}\frac{f_H/h}{MNT_g}\left(1-(1-p_n\frac{1}{N})^x\right)\right)^{K_0}$ *and* $\Pr\left[\bigcup_{k\in\mathcal{K}_0}E_{fa,k,0}\middle||\mathcal{K}_0|=K_0\right]=1-\left(1-\frac{f_H/h}{MT_g}\right)^{K_0}$*. As the average number of radars falling into radar* 0*'s interference range is* $\mathbb{E}[|\mathcal{K}_0|]=2\lambda d_{i,max}$*, we have* $|\mathcal{K}_0|=K_0\sim$ *Pois*$(2\lambda d_{i,max})$*. By definition, we have* $\Pr\left[E^n_{md}\right]$ *given in* (2.5)*, and*

$$\Pr\left[E_{fa}\right]=1-\exp\left[-2\lambda d_{i,max}\frac{f_H/h}{T_gM}\right]. \tag{2.7}$$

As the above (2.5) *and* (2.7) *are the same for all radar, UA is a fair MAC. By* (2.4) *and* (2.7) *we have* (2.6)*.*

The term $\frac{f_H/h}{T_g}$ in (2.5) and (2.6) represents the fraction of time that a victim radar can dechirp interference into its IF band within a chirp repetition duration T_g. The term M in (2.6) is due to RFDM, and hence is called the RFDM gain. Under the setup in Table 2.1, we have $r_{230}=170$m, $r_{365}=435$m, and $p_{230}=p_{365}=0.221$ for UA-RFDM. Under this setup, we simulate $\Pr\left[E^n_{md}\right]$, $n\in\{1,2,\ldots,N\}$ and $C_{UA-RFDM}$ in Figure 2.21, Figure 2.22 and Figure 2.23. From Figure 2.21, we can see that $\Pr\left[E^n_{md}\right]$ is very small and increases linearly with λ under the considered setup. Further, $\Pr\left[E^n_{md}\right]$ increases with n as the target power decreases with n; $\Pr\left[E^n_{md}\right]$ increases with x as the probability that targets fall into interference side-lobes increases with x. Figure 2.22 and Figure 2.23 show UA-RFDM achieves poor capacity when λ or $\Pr\left[E^n_{md}\right]$ is moderately large. For example, when $\lambda = 2$ (2 radars/m), the capacity of UA-RFDM is close to 0. The maximum capacity of UA-RFDM $C^*_{UA-RFDM}$ is achieved at $\lambda^*_{UA-RFDM} = \frac{1}{2d_{i,max}} \frac{MT_g}{f_H/h} = 0.066$ radars/m, and $C^*_{UA-RFDM} = \frac{\lambda^*_{UA-RFDM}}{e} = 0.024$ radars/m.

2.5 UA-FH

To enhance the performance of UA-RFDM, we next modify the RFDM into frequency hopping (FH), an idea previously considered in [42] and [59] to suppress the interference peak power on range-velocity bins. Such a scheme is called UA-FH shown in Figure 2.8. When multiple sub-bands are available, each radar randomly and independently chooses one of the sub-bands for transmission in each chirp cycle. Over a CPI, the radar targets always appear in the same range bin, while the de-chirped ghosts randomly appear in range bins due to FH. For example, in Figure 2.8, radar 1 and radar 2 randomly and independently hop on 2 sub-bands in each chirp cycle, and they only choose the same sub-band in the first chirp cycle. Thus, in Figure 2.9, radar 1's ghost only appears at radar 2's receiver in the first chirp cycle. Compared to [42] and [59], the key innovation in our scheme is that we propose to use the random appearance of ghosts as a characteristic to distinguish ghosts from targets. This innovation, called detect-and-classify, avoids the identified ghosts passing for velocity DFT and reduces the probability of false alarm on range-velocity bins.

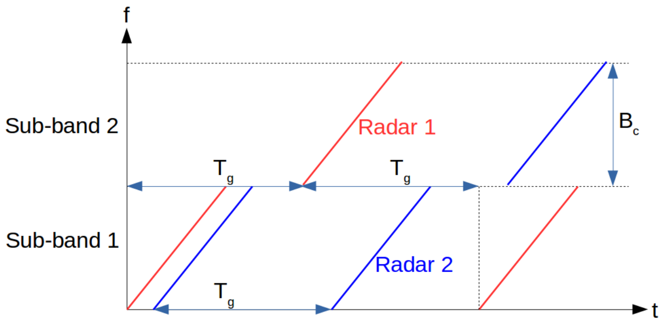

Figure 2.8: UA-FH on 2 sub-bands. (© 2021 IEEE)

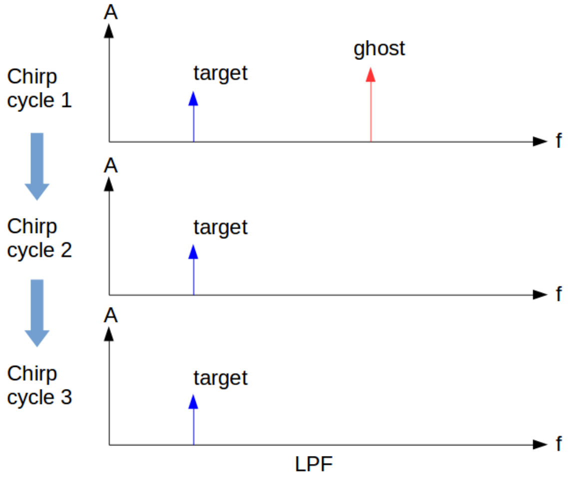

Figure 2.9: Detect-and-classify using frequency hopping: a ghost can be distinguished from a target as it randomly appears on a range bin over different chirp cycles. (© 2021 IEEE)

The FMCW radar block diagram under UA-FH is shown in Figure 2.10. The detect-and-classify block in Figure 2.10 counts the appearance of a signal on each range bin over a CPI. The radar conducts velocity DFT on a range bin only if the signal on that range bin appears in every chirp cycle (i.e., L times) over a CPI. Compared to [42] and [59] which also propose FH, the key novelty in our FH scheme is that we propose to use the random appearance of ghosts caused by FH as a characteristic to distinguish ghosts from targets. When a ghost and target do not fall into the same range bin, the ghost can be distinguished from a target and not putted into velocity DFT with probability $1 - \frac{1}{M^L} \approx 1$, thereby mitigating false alarm, as verified in Figure 2.11. However, when a ghost and a target fall into the same range bin of a victim radar, the persistently appearing target causes the detect-and-classify block to fail. In this case, under the setup in Table 2.1, if the sub-band choice of the interfering radar and the victim radar overlap more than 6% in a CPI, which happens with probability very close to 1, the ghost from the interfering radar can cause false alarm at the victim radar (see Figure 2.12). Thus, if $G_{k,0}^n \cap H_0^n$ happens, where H_0^n is the event that there exists at least a target at range bin n of the victim radar 0, radar k's ghost at range bin n causes false alarm at radar 0. Hence, conditioned on $k \in \mathcal{K}_0$, $E_{fa,k,0} = \bigcup_{n=1}^{N} \left(G_{k,0}^{n} \cap H_0^{n} \right)$.

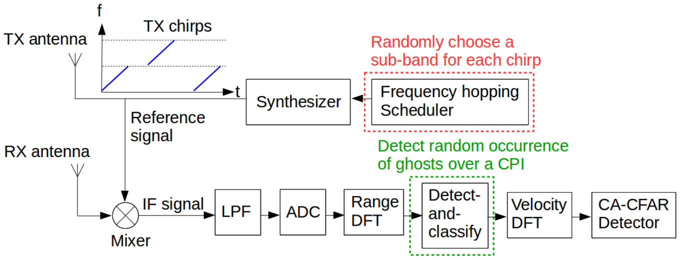

Figure 2.10: FMCW radar block diagram under UA-FH. (© 2021 IEEE)

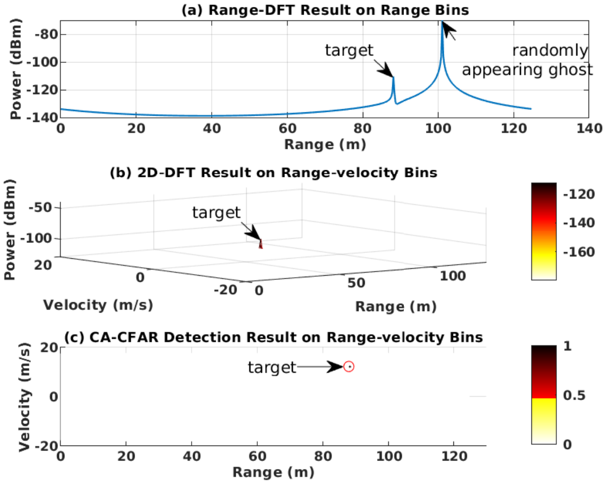

Figure 2.11: PHY layer simulation under UA-FH with the same setup as in Figure 2.6. (© 2021 IEEE)

Our simulations find that when a high-power ghost and a target fall into the same range bin, the target may be mis-detected on range-velocity bins due to the noise floor elevation caused by the randomly appearing interference as shown in Figure 2.12. This happens with a high probability when the ghost is strong enough. Then, conditioned on $k \in \mathcal{K}_0$, we model

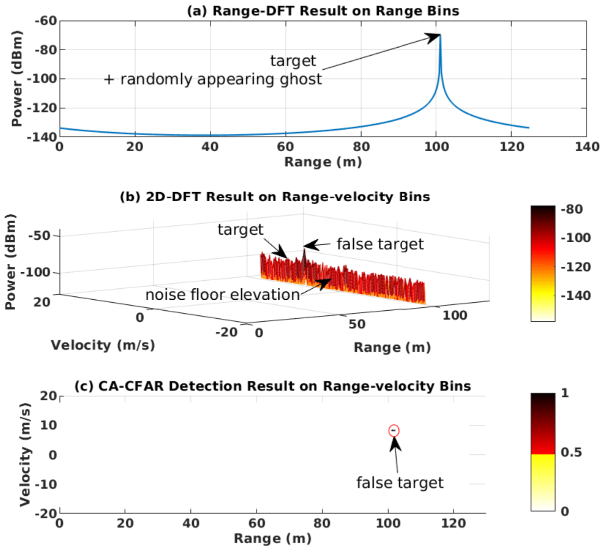

Figure 2.12: PHY layer simulation under UA-FH with the same setup as in Figure 2.7. (© 2021 IEEE)

$E^n_{md,k,0} = R^n_{k,0} \cap G^n_{k,0} \cap H^n_0$, where $R^n_{k,0}$ is the event that the range $d_{k,0}$ between radar k and radar 0 is smaller than a threshold r_n. Focus on analyzing the performance of a reference victim radar 0, we have the following result.

Proposition 2 (PHY and MAC Layer Properties of UA-FH) *UA-FH is a fair MAC with target misdetection probability at range bin n*

$$\Pr\left[E^n_{md}\right] = 1 - \exp\left[-\frac{2\lambda r_n f_H/h}{NT_g}\left(1-(1-\frac{1}{N})^x\right)\right], \tag{2.8}$$

and multiple access capacity

$$C_{UA-FH} = \lambda \exp\left[-2\lambda d_{i,max}\frac{f_H/h}{T_g\left(1-(1-\frac{1}{N})^x\right)^{-1}}\right], \tag{2.9}$$

conditioned on the number of targets seen by each radar is x.

Proof 2 *As each target independently and randomly falls into radar's range-velocity bins,* $\Pr[H_0^n] = 1 - (1 - \frac{1}{N})^x$. *As each ghost can only fall into one range bin, we have*

$$\Pr\left[E_{fa,k,0} \middle| k \in \mathcal{K}_0\right] = \Pr\left[\bigcup_{n=1}^{N} \left(G_{k,0}^n \cap H_0^n\right) | k \in \mathcal{K}_0\right]$$

$$= \sum_{n=1}^{N} \Pr\left[G_{k,0}^n | k \in \mathcal{K}_0\right] \Pr\left[H_0^n\right] = \frac{f_H/h}{T_g}(1 - (1 - \frac{1}{N})^x).$$

Also, by proof of Proposition 1, $\Pr\left[R_{k,0}^n\right] = \frac{r_n}{d_{i,max}}$. *Thus,*

$$\Pr\left[E_{md,k,0}^n | k \in \mathcal{K}_0\right] = \frac{r_0}{d_{i,max}} \frac{f_H/h}{NT_g} \left(1 - (1 - \frac{1}{N})^x\right).$$

Then, using the similar steps as the proof of Proposition 1, we arrive at (2.8) *and* (2.9).

The term $\left(1 - (1 - \frac{1}{N})^x\right)^{-1}$ in (2.9) can be regarded as the FH gain that must be weighed against the loss of RFDM gain M, when compared with (2.6) for UA-RFDM. When the number of targets $x < \frac{\ln(1-1/M)}{\ln(1-1/N)}$, we have $\left(1 - (1 - \frac{1}{N})^x\right)^{-1} > M$, and in this case, $C_{UA-FH} > C_{UA-RFDM}$. For example, under the setup in Table 2.1, $C_{UA-FH} > C_{UA-RFDM}$ if $x < 312$. As this happens in most cases, when x is small to moderate (e.g., $x < 50$), we have $\left(1 - (1 - \frac{1}{N})^x\right)^{-1} \gg M$, and hence $C_{UA-FH} \gg C_{UA-RFDM}$. However, when $x > \frac{\ln(1-1/M)}{\ln(1-1/N)}$, we have $C_{UA-FH} < C_{UA-RFDM}$. Thus, when the number of targets seen by each radar is not very large, the UA-FH capacity is larger than UA-RFDM capacity, and vice versa. Under the setup in Table 2.1, we have $r_{230} = 100$m and $r_{365} = 265$m for UA-FH. Under this setup, we simulate $\Pr[E_{md}^n]$, $n \in \{1, 2, \ldots, N\}$ and C_{UA-FH} in Figure 2.21, Figure 2.22 and Figure 2.23. From Figure 2.21, we can see that $\Pr[E_{md}^n]$ of UA-FH is larger than $\Pr[E_{md}^n]$ of UA-RFDM. However, $\Pr[E_{md}^n]$ of UA-FH is in general small, and increases linearly with λ under the considered setup. From Figure 2.22 and Figure 2.23, we see that C_{UA-FH} is much larger than $C_{UA-RFDM}$ for all the considered x, λ and most region of $\Pr[E_{md}^n]$. The maximum capacity of UA-FH C_{UA-FH}^* is achieved at $\lambda_{UA-FH}^* = \frac{1}{2d_{i,max}} \frac{T_g}{f_H/h} \frac{1}{1-(1-\frac{1}{N})^x}$, and $C_{UA-FH}^* = \frac{\lambda_{UA-FH}^*}{e}$, which is shown in Figure 2.22 under different x.

2.6 UA-RFDM-PC

Another method to enhance UA-RFDM is to combine it with phase coding (PC) proposed in [55, 63, 75]. Such scheme is called UA-RFDM-PC shown in Figure 2.13. In each chirp cycle, the radar transmitter adds a random binary phase rotation 0 or π on the chirp before transmitting, where 0 and π are chosen with equal probability. At the radar receiver, the random binary phase rotation is compensated back after de-chirping the received signal. As shown in Figure 2.14, after the phase compensation, the target phase increases linearly over different chirp cycles as normal. In contrast, as the code of an interfering radar does not match the code of a victim radar, the phase increment of the ghost seen at the victim radar receiver is random. Thus, after velocity DFT, ghosts are spread into pseudo-noise at the victim radar's detector input. This scheme can achieve much better multiple access capacity than UA-RFDM, as ghosts appear as incoherent noise and infrequently cause false alarms.

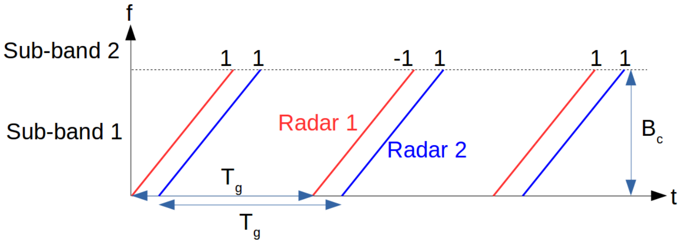

Figure 2.13: UA-RFDM-PC with 2 radars independently choosing sub-band 1. (© 2021 IEEE)

The FMCW radar block diagram under UA-RFDM-PC is shown in Figure 2.15. After phase decoding, the additional phase rotations on a typical radar 0's target signals are 0, while the additional phase rotations of radar k's ghosts are random. After velocity DFT, the ghost is spread as pseudo-noise into radar 0's velocity bins, due to its random phase in a CPI. This is verified in Figure 2.16 and Figure 2.17.

Our simulations find that the pseudo-noise on any range bin can occasionally cause false alarm; an example is shown in Figure 2.16. Also, when the number of ghosts in a range bins

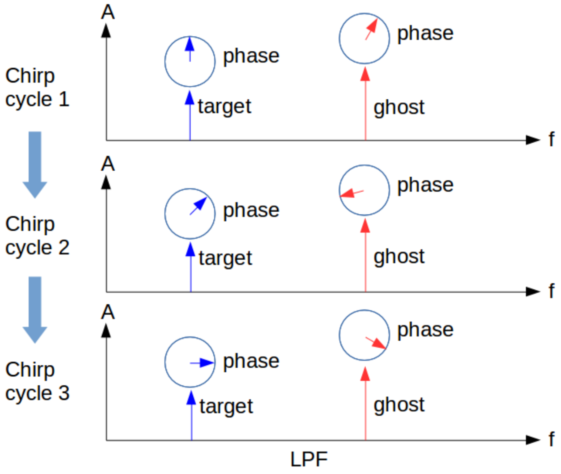

Figure 2.14: Detect-and-classify using phase coding: a ghost can be distinguished from a target due to it's random phase over different chirp cycles. (© 2021 IEEE)

is smaller than 4 (holds with high probability under the considered setup), the probability of false alarm caused by the ghost-spread pseudo-noise is insensitive to the ghost power and the range bin that the ghost falls into. Thus, we denote $J_{k,0}$ as the event that radar k's ghost-spread pseudo-noise causes false alarm at radar 0, which happens with probability p_0. Then, conditioned on $k \in \mathcal{K}_0$, we model that $E_{fa,k,0} = F^1_{k,0} \cap \left(\bigcup_{n=1}^N G^n_{k,0}\right) \cap J_{k,0}$. Furthermore, when a high-power ghost and a target fall into the same range bin of the victim radar, the target can be mis-detected due to the high-power pseudo-noise, as shown in Figure 2.17. This happens with high probability when the ghost is strong enough. For $k \in \mathcal{K}_0$, we model $E^n_{md,k,0} = R^n_{k,0} \cap F^1_{k,0} \cap G^n_{k,0} \cap H^n_0$, where $R^n_{k,0}$ denotes the event that the range between radar k and radar 0 is smaller than a threshold r_n, and H^n_0 denotes the event that there exists at least a target falls into the range bin n of radar 0. Then, we have the following result.

Proposition 3 (PHY and MAC Layer Properties of UA-RFDM-PC) *UA-RFDM-PC is a fair MAC with target misdetection probability at range bin n*

$$\Pr\left[E^n_{md}\right] = 1 - \exp\left[\frac{-2\lambda r_n f_H/h}{MNT_g}(1-(1-\frac{1}{N})^x)\right], \tag{2.10}$$

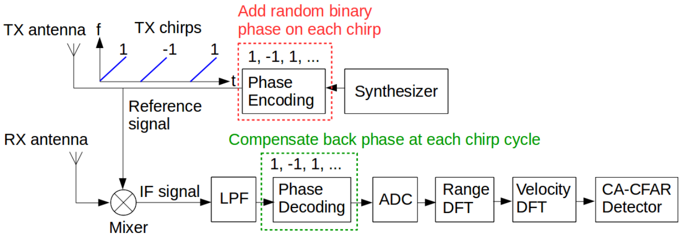

Figure 2.15: FMCW radar block diagram under UA-RFDM-PC. (© 2021 IEEE)

and multiple access capacity

$$C_{UA-RFDM-PC} = \lambda \exp\left[-2\lambda d_{i,max} \frac{f_H/h}{T_g M p_0^{-1}}\right], \tag{2.11}$$

conditioned on the number of targets seen by each radar is x*.*

Proof 3 *By proof of Propositions 1 and 2, we have* $\Pr\left[R_{k,0}^n\right] = \frac{r_n}{d_{i,max}}, \Pr\left[F_{k,0}^1\right] = \frac{1}{M}$*,* $\Pr\left[G_{k,0}^n \middle| k \in \mathcal{K}_0\right] = \frac{f_H/h}{NT_g}$*,* $\forall n \in \{1,2,\ldots,N\}$*, and* $\Pr\left[H_0^n\right] = 1-(1-\frac{1}{N})^x$*. We also have* $\Pr\left[J_{k,0}\right] = p_0$*. Thus,* $\Pr\left[E_{md,k,0}^n \middle| k \in \mathcal{K}_0\right] = \frac{r_0}{d_{i,max}} \frac{f_H/h}{MNT_g}\left(1-(1-\frac{1}{N})^x\right)$*,* $\Pr\left[E_{fa,k,0} \middle| k \in \mathcal{K}_0\right] = \frac{f_H/h}{MT_g} p_0$*. Then, using the similar steps as the proof of Proposition 1, we arrive at* (2.10) *and* (2.11)*.*

The term p_0^{-1} in (2.11) can be regarded as the PC gain. Since UA-RFDM-PC also keeps the RFDM gain M, it follows that $C_{UA-RFDM-PC} \gg C_{UA-RFDM}$. Under the setup in Table 2.1, we have $p_0 = 0.033$, $r_{230} = 130$m and $r_{365} = 265$m for UA-RFDM-PC. Under this setup, we simulate $\Pr\left[E_{md}^n\right]$, $n \in \{1,2,\ldots,N\}$ and $C_{UA-RFDM-PC}$ in Figure 2.21, Figure 2.22 and Figure 2.23. From Figure 2.21, we can see that $\Pr\left[E_{md}^n\right]$ of UA-RFDM-PC is smaller than that of UA-FH, but is larger than that of UA-RFDM. From Figure 2.22 and Figure 2.23, we see that $C_{UA-RFDM-PC}$ is much larger than $C_{UA-RFDM}$ for all the considered x, λ and most region of $\Pr\left[E_{md}^n\right]$. The maximum capacity of UA-RFDM-PC $C_{UA-RFDM-PC}^*$ is achieved at $\lambda_{UA-RFDM-PC}^* = \frac{1}{2d_{i,max}} \frac{MT_g}{f_H/h} \frac{1}{p_0} = 2$ radars/m, and $C_{UA-RFDM-PC}^* = \frac{\lambda_{UA-RFDM-PC}^*}{e} = 0.736$ radars/m.

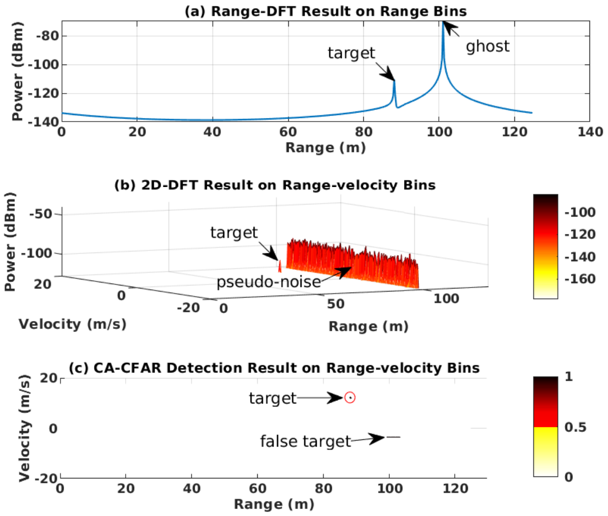

Figure 2.16: PHY layer simulation under UA-RFDM-PC with the same setup as in Figure 2.6 and Figure 2.11. (© 2021 IEEE)

2.7 UA-FH-PC

In UA-FH, a persistently appearing target can make randomly appearing ghosts on the same range bin unidentified and cause false alarms. PC can spread these unidentified ghosts into pseudo-noise and further reduce false alarm probability. In UA-RFDM-PC, ghosts on any range bin are spread into pseudo-noise that has the potential to cause false alarms on any range bin. FH helps to identify ghosts and reduces the occurrence of pseudo-noise when the ghosts do not fall into the same range bin as a target. These motivate us to combine UA, FH and PC into UA-FH-PC shown in Figure 2.18. In UA-FH-PC, each chirp is added with binary random phase rotation and is transmitted on a randomly picked subband. This scheme can achieve much better multiple access capacity than UA-FH and UA-RFDM-PC, as FH and PC remedy the disadvantage of each other.

The corresponding FMCW receiver block diagram is shown in Figure 2.19. Due to FH, when a ghost and target do not fall into the same range bin, the ghost can be distinguished

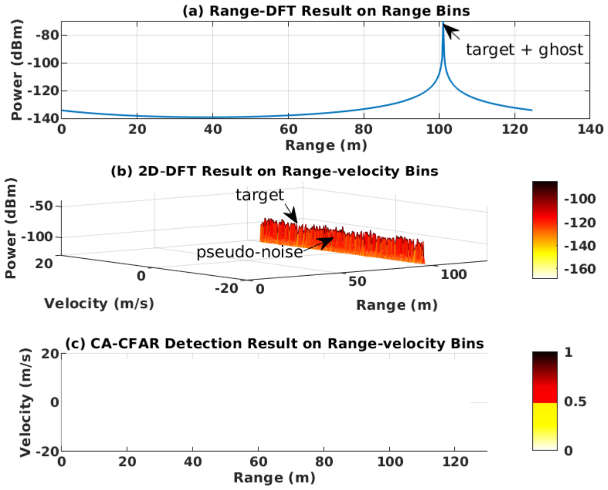

Figure 2.17: PHY layer simulation under UA-RFDM-PC with the same setup as in Figure 2.7 and Figure 2.12. (© 2021 IEEE)

from a target with probability $1 - \frac{1}{M^L} \approx 1$ and not passed into velocity DFT to avoid a false alarm. But when a ghost and a target fall into the same range bin of a victim radar, the persistently appearing target causes the detect-and-classify block to fail. However, with PC, the non-classified ghost is spread into pseudo-noise (see Figure 2.20) that only infrequently causes a false alarm. When the number of ghosts in a range bin is smaller than 4 (holds with high probability under the considered setup), the probability of false alarm caused by the ghost-spread pseudo-noise is insensitive to the ghost power and the range bin that the ghost falls into. Thus, we denote $J_{k,0}$ as the event that radar k's ghost-spread pseudo-noise causes false alarm at radar 0, which happens with probability p_0. Then, conditioned on $k \in \mathcal{K}_0$, we model that $E_{fa,k,0} = \bigcup_{n=1}^{N} \left(G^n_{k,0} \cap H^n_0\right) \cap J_{k,0}$, where $G^n_{k,0}$ is the time condition that radar k's ghost falls into radar 0's range bin n, and H^n_0 denotes the event that there exists at least a target falls into the range bin n of radar 0. When a strong enough ghost and a target fall into the same range bin of the victim radar, the target can be mis-detected with high probability due to the high-power pseudo-noise. Thus, for $k \in \mathcal{K}_0$, we model $E^n_{md,k,0} = R^n_{k,0} \cap G^n_{k,0} \cap H^n_0$,

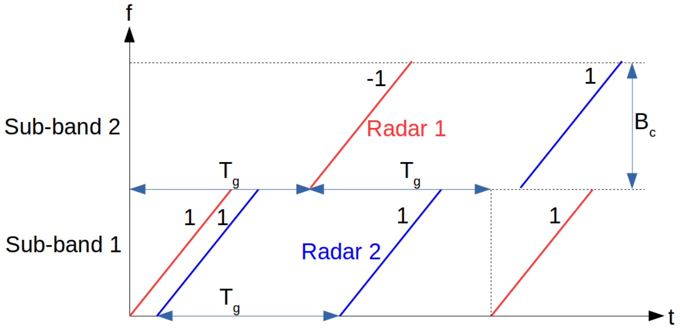

Figure 2.18: UA-FH-PC on 2 sub-bands. (© 2021 IEEE)

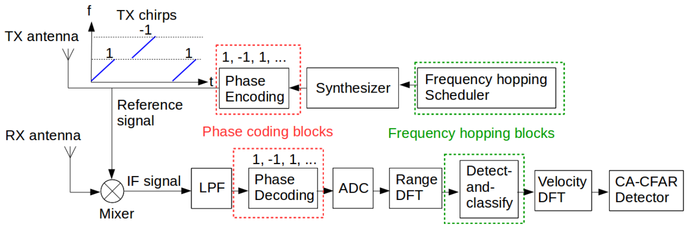

Figure 2.19: FMCW radar block diagram under UA-FH-PC. (© 2021 IEEE)

where $R^n_{k,0}$ denotes the event that the range between radar k and radar 0 is smaller than a threshold r_n. Then, we have the following result.

Proposition 4 (PHY and MAC Layer Properties of UA-FH-PC) *UA-FH-PC is a fair MAC with target misdetection probability at range bin n*

$$\Pr\left[E^n_{md}\right] = 1 - \exp\left[\frac{-2\lambda r_n f_H/h}{NT_g}\left(1-(1-\frac{1}{N})^x\right)\right], \tag{2.12}$$

and multiple access capacity

$$C_{UA-FH-PC} = \lambda \exp\left[-2\lambda d_{i,max}\frac{f_H/h}{T_g p_0^{-1}\left(1-(1-\frac{1}{N})^x\right)^{-1}}\right], \tag{2.13}$$

conditioned on the number of targets seen by each radar is x.

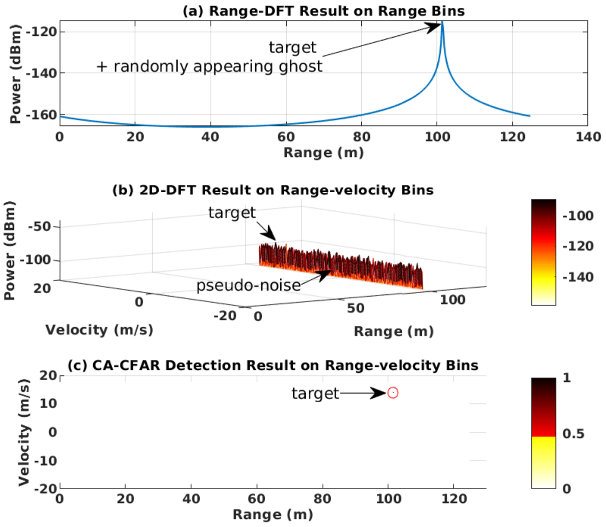

Figure 2.20: PHY layer simulation under UA-FH-PC with the same setup as in Figure 2.7, Figure 2.12 and Figure 2.17. (© 2021 IEEE)

Proof 4 *The proof of* (2.12) *is similar to the proof of* (2.8) *in Proposition 2. By proof of Propositions 3, we have* $\Pr\left[G_{k,0}^{n} \middle| k \in \mathcal{K}_0\right] = \frac{f_H/h}{NT_g}$, $\forall n \in \{1, 2, \ldots, N\}$, $\Pr\left[J_{k,0}\right] = p_0$ *and* $\Pr\left[H_0^n\right] = 1 - (1 - \frac{1}{N})^x$. *Thus,* $\Pr\left[E_{fa,k,0} \middle| k \in \mathcal{K}_0\right] = \frac{f_H/h}{T_g} p_0 \big(1 - (1 - \frac{1}{N})^x\big)$. *Then, using the similar steps as the proof of Proposition 1, we arrive at* (2.13).

Under the setup in Table 2.1, when x is small to moderate (e.g., $x < 50$), the FH gain $\big(1 - (1 - \frac{1}{N})^x\big)^{-1}$ is much larger than the RFDM gain M, and hence $C_{UA-FH-PC} \gg C_{UA-RFDM-PC}$. Compared to UA-FH, UA-FH-PC has an additional PC gain p_0^{-1}, and hence $C_{UA-FH-PC} \gg C_{UA-FH}$. For the system scenario in Table 2.1, we further have $r_{230} = 85$m and $r_{365} = 200$m for UA-FH-PC, which are smaller than those of UA-RFDM-PC, as FH reduces the ghost-spread pseudo-noise power. Our PHY layer simulation finds that $p_0 = 0.03$. Based on these, we simulated $\Pr\left[E_{md}^n\right]$, $n \in \{1, 2, \ldots, N\}$ and $C_{UA-FH-PC}$ in Figure 2.21, Figure 2.22 and Figure 2.23. From Figure 2.21, we see that $\Pr\left[E_{md}^n\right]$ of UA-FH-PC is smaller than that of UA-FH, but larger than that for UA-RFDM-PC and UA-

RFDM. From Figure 2.22 and Figure 2.23, we see that the capacity of UA-FH-PC is achieves the largest capacity for all the considered x, λ and most region of $\Pr\left[E_{md}^n\right]$. The maximum capacity of UA-FH-PC $C_{UA-FH-PC}^*$ is achieved at $\lambda_{UA-FH-PC}^* = \frac{1}{2d_{i,max}} \frac{T_g}{p_0 f_H/h} \frac{1}{1-(1-\frac{1}{N})^x}$, and $C_{UA-FH-PC}^* = \frac{\lambda_{UA-FH-PC}^*}{e}$, which is large. For example, when $x = 10$, we have $C_{UA-FH-PC}^* = 18.393$ radars/m achieved at density $\lambda_{UA-FH-PC}^* = 49.997$ radars/m.

We finally compare the capacities of the considered four distributed MAC schemes with the capacity of the state-of-the-art synchronous cooperative MAC scheme - RadChat [7]. RadChat uses time division multiple access (TDMA) for mitigating radar interference. By [7], the upper bound of the maximum number of non-false-alarmed radar is $\frac{MB_c}{f_H + d_{i,max}h/c}$. Thus, the upper bound of the capacity of RadChat is $\frac{MB_c}{2(f_H + d_{i,max}h/c)d_{i,max}}$. Since it's not clear in [7] how RadChat handles the case when radar density is larger than this upper bound, we assume the capacity upper bound of RadChat saturates at $\frac{MB_c}{2(f_H + d_{i,max}h/c)d_{i,max}}$ after reaching this value, and do not calculate the probability of target misdetection of RadChat. Under the setup in Table 2.1, the capacity upper bound of RadChat is 0.011 radars per meter, which is plotted in Figure 2.22. The capacities of UA-FH, UA-RFDM-PC and UA-FH-PC are significantly larger than the capacity of RadChat. This indicates that 1) orthogonal TDMA scheduling may not achieve desired scaling of multiple access capacity; 2) it is possible to design radar MAC schemes with large multiple access capacity even without synchronization and coordination, by using detect-and-classify approaches such as FH and PC. These results can serve as potential guides to any future radar standardization activities.

2.8 Summary

Under coherent mutual radar interference, the main issue is the difficulty to classify interference from targets, which leads to false alarms. In this chapter, we considered using radar MACs to help radars finish this classification and reduce false alarms. The main contribution of this chapter lies in the cross-layer analysis of radar coherent interference networks using proposed 2 metrics: target misdetection probabilities and multiple access capacities.

As a baseline scheme, we first analyzed UA-RFDM. UA-RFDM achieves a poor trade-off

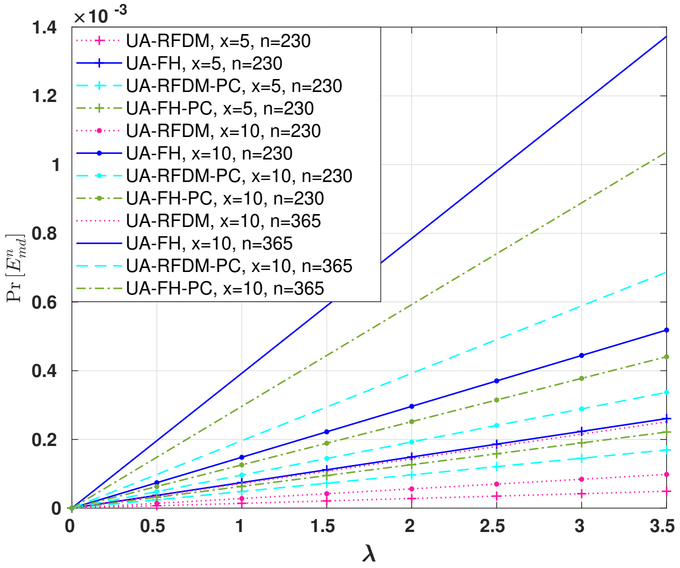

Figure 2.21: Probability of target misdetection versus λ under different range bins. (© 2021 IEEE)

between multiple access capacity and probability of target misdetection (see Figure 2.23), due to its low multiple access capacity. The key reason for the poor multiple access capacity of UA-RFDM is that each radar's sub-band choice and chirp's initial phase are unchanged over a CPI. This makes ghosts appear as targets, and hence cannot be distinguished. Thus, UA-RFDM is not a promising candidate for scaling to high-density vehicular radar scenarios.

FH helps each radar to distinguish targets and ghosts on range bins. The target misdetection and false alarm happen only when the target and ghosts fall into the same range bin. Compared with UA-RFDM, UA-FH obtains FH gain at the cost of losing RFDM gain. When the number of targets seen by each radar is not very large, the capacity of UA-FH is much larger than the capacity of UA-RFDM. The target misdetection probabilities of UA-FH are larger than those of UA-RFDM, but in most regions, UA-FH achieves better trade-offs between multiple access capacity and target misdetection probability.

UA-RFDM-PC adopts PC to help each radar to distinguish targets and interference on

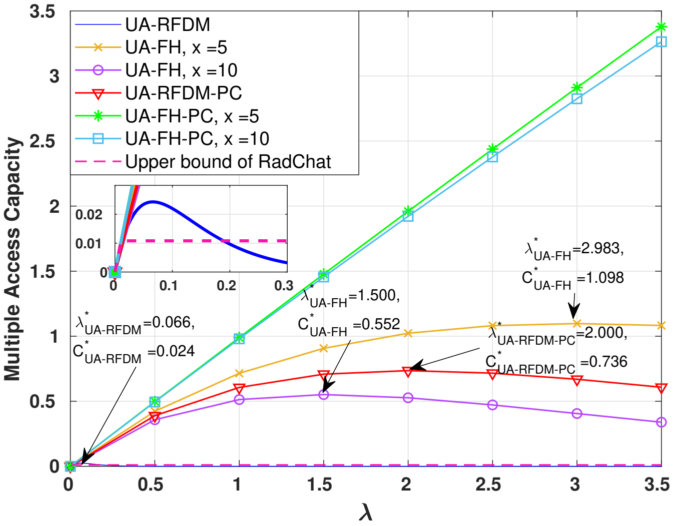

Figure 2.22: Multiple access capacity versus λ. (© 2021 IEEE)

range-velocity bins. Target misdetection happens only when the target and ghosts fall into the same range bin. False alarm occasionally happens when a ghost falls into any range bin. Compared with UA-RFDM, UA-RFDM-PC keeps RFDM gain and has an additional PC gain, which makes the capacity of UA-RFDM-PC much larger than the capacity of UA-RFDM. The target misdetection probability of UA-RFDM-PC is better than that of UA-FH under the setup in Table 2.1.

UA-FH-PC adopts both FH and PC to help each radar to distinguish targets and interference on range-velocity bins. The target misdetection and false alarm happen only when the target and ghosts fall into the same range bin. UA-FH-PC has FH gain and PC gain that can be multiplied together to achieve significant capacity gain. This makes the capacity of UA-FH-PC much larger than the capacities of UA-RFDM, UA-FH and UA-RFDM-PC. The target misdetection probability of UA-FH-PC is better than UA-FH, but is worse than UA-RFDM-PC and UA-RFDM.

Finally, we compare the performance of the considered MAC schemes in Table 2.2. The coherent interference under UA-RFDM can lead to a very low multiple access capacity. In

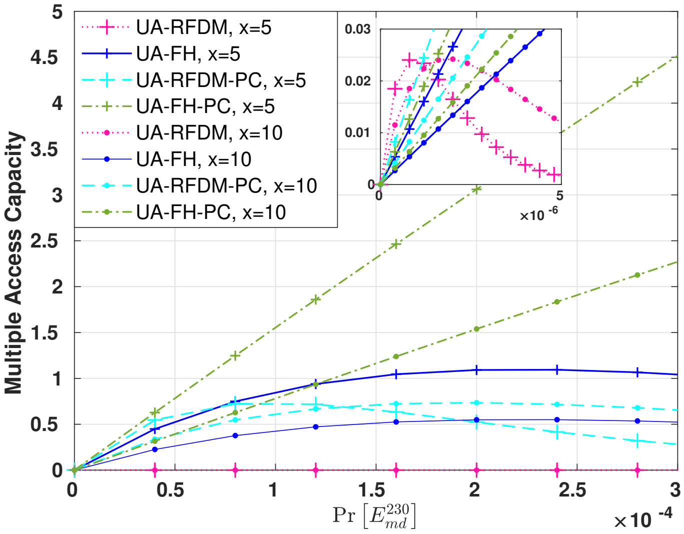

Figure 2.23: Multiple access capacity versus probability of target misdetection at range bin 230 (at around half of the maximum detectable range). (© 2021 IEEE)

contrast, the detect-and-classify schemes, such as FH and PC, significantly increase multiple access capacity and achieve good trade-offs between multiple access capacity and probability of target misdetection. These detect-and-classify schemes do not require any synchronization and coordination, and can be implemented with low cost, especially for UA-RFDM-PC.

Table 2.1: PHY layer simulation setup. (© 2021 IEEE)

Simulation platform	MATLAB
Transmit power	$P_t = 12$dBm [50]
Transmit/receive antenna gain	$G_t = G_r = 12$dBi [50]
Minimum receive power	$P_r^{min} = -128$dBm [50]
RF frequency	$f_c = 77$GHz [50]
Chirp bandwidth	$B_c = 540$MHz [19]
IF cutoff frequency	$f_H = 10$MHz [19]
Chirp slope	$h = 12$MHz/us [19]
Number of range bins	$N = 450$ [19]
Inter-chirp duration	$T_g = 55$us [19]
Interference range	$d_{i,max} = 1000$m
Number of chirps in a CPI	$L = 200$
Number of sub-bands	$M = 2$
Target's RCS	$20m^2$
CA-CFAR operating domain	Doppler domain
Number of noise window in CA-CFAR	20
Number of guard window in CA-CFAR	2
CFAR threshold	10dB

Table 2.2: Summary of 4 Considered MACs. (© 2021 IEEE)

MACs	Prob. of target misdetection	Capacity gain	Multiple access capacity
UA-RFDM	Very low	RFDM	Very small
UA-FH	Low	FH	Moderate
UA-RFDM-PC	Low	RFDM & PC	Moderate
UA-FH-PC	Low	FH & PC	Large

Chapter 3

FAST-TIME-FREQUENCY MODE RETRIEVAL FOR MITIGATING INCOHERENT INTERFERENCE

3.1 Motivation

In this chapter, we are interested in the fast-time domain MIM for incoherent FMCW interference. Incoherent FMCW interference exhibits unique signatures in the fast-time-frequency (fTF) representation, as shown in Figure 3.1 (a), where the sinusoidal-like target is focused on one range frequency bin while the power-dominating interference intersects the target in a form of a chirp. Previous approaches exploit the linear chirp feature of the interference and set detected interference to zero in the short-time Fourier transform (STFT) domain (as referred to as STFT-Zeroing) [71]. However, errors in the interference detection and zeroing steps easily propagate to the fast-time domain and it results in strong residuals, as shown in blue lines in Figure 3.1 (b). This effect becomes worse when the low-resolution STFT is used [18].

Instead of focusing on nulling interference like the most fast-time MIM methods, this chapter proposes to directly recover fast-time target signals via a direct fTF mode retrieval (fTFMR). Key challenges are 1) to identify weaker target ridges among significantly stronger interference ridges that spread linearly over the fTF representation and 2) to enable high-precision fTFMR that maps the identified target-inclusive fTF representation into the fast-time sample. This is achieved by a cascade of high-resolution fTF representation, robust ridge detection using sequential pulses, and direct fTFMR. The advantages of the proposed method are listed below:

- First, a high-resolution fTF representation enables higher-degree separation between the target signals and interference signals. This is particularly important to the case

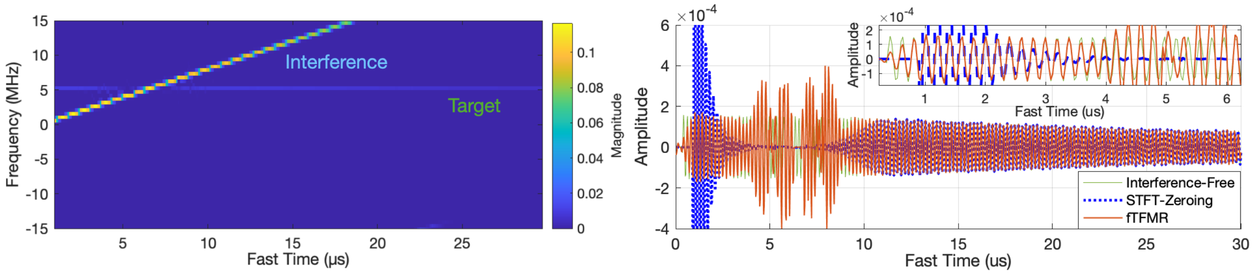

(a) High-resolution fast-time-frequency representation using the FSST

(b) Recovered fast-time target signal

Figure 3.1: Fast-time-frequency (fTF) representation of targets and interference and a direct fTF mode retrieval (fTFMR) of underwhelmed target signals. (© 2022 IEEE)

that the interference beat frequency crosses over that of the target; see Figure 3.1 (a). To this end, we make use of a frequency reassignment-based Fourier synchrosqueezing transform (FSST) [5, 48, 64, 65] that enables high-resolution fTF representation.

- Second, the proposed ridge detection exploits the fact that the target signature over the fTF domain is consistent over multiple pulses, while the interference signature is highly likely to vary due to the incoherent nature between the interfering and victim radars. This results in a robust ridge detection of underwhelmed two-way attenuated target signals among one-way attenuated interference.

- Third, the fTFMR is guaranteed to converge to the target signal in fast-time intervals with sufficient separation between the target and interference in the fTF domain. As the FSST highly focuses on sinusoidal-like target signals, the fTFMR can directly recover target signals in the time-domain by integrating the fTR representation over the target-only region and, at the same time, filtering out interference and noise.

Major materials of this chapter is presented the author's accepted paper [34][1].

---

[1] © 2022 IEEE. Reprinted, with permission, from [34].

3.2 Target and Interference Signal Model

Assuming an FMCW automotive radar, indexed by u, transmits a sequence of chirp pulses with carrier frequency modulated at the radio frequency (RF) bands and a pulse repetition interval (PRI) $\widetilde{T}_u$ [6]

$$x_u^{RF}(t) = a_u^{RF} e^{j2\pi(f_0 t + 0.5 h_u t^2)},\ \forall t \in [0, T_u] \tag{3.1}$$

where a_u^{RF} is the RF amplitude, f_0 is the central frequency, h_u is the chirp rate, T_u is the chirp sweep duration, and $\widetilde{T}_u - T_u$ is the inter-pulse idle duration. Without loss of generality, all automotive radars operate at the same central frequency f_0, e.g., $f_0 = 77$ GHz, but with with different chirp sweep duration T_u, PRI $\tilde{T}_u$, and chirp rate h_u. Furthermore, the victim radar is referred to as the radar 0, i.e., $u = 0$. For the l-th chirp pulse, the dechirped signal of the victim radar is a multi-component signal

$$x_l(t) = x_l^o(t) + x_l^i(t) = \sum_{k=1}^{K^o} x_{l,k}^o(t) + \sum_{u=1}^{U_l^i} x_{l,u}^i(t), \tag{3.2}$$

where $x_l^o(t)$ consists of K^o target components, and $x_l^i(t)$ is the sum of U_l^i interference components. Note that the number of interference U_l^i may vary over the pulse.

For the *target component* $x_{l,k}^o(t)$, one can derive its expression by multiplying the attenuated and delayed copy with the transmitted signal in (3.1) at the local oscillator, and

$$x_{l,k}^o(t) = a_k^o e^{j2\pi\phi_{l,k}^o(t)},\ \forall t \in [0, T_0], \tag{3.3}$$

where a_k^o is the intermediate frequency (IF) amplitude of target k, and the phase term is given as

$$\phi_{l,k}^o(t) = (f_{r,k}^o + f_{D,k}^o)t + f_{D,k}^o(l-1)T_0, \tag{3.4}$$

with $f_{r,k}^o$ and $f_{D,k}^o$ denoting the beat frequency and, respectively, the Doppler frequency of the k-th target.

On the other hand, the *interference component* may or may not be dechirped into the IF band of the victim radar, depending on FMCW configurations between the victim radar

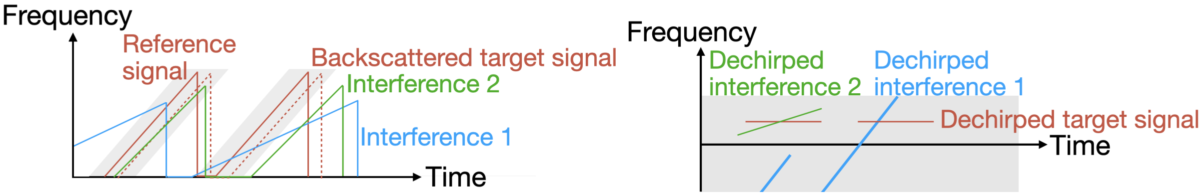

(a) RF band signal

(b) IF band signal

Figure 3.2: FMCW radar interference over multiple pulses. (© 2022 IEEE)

$\{f_0, h_0, T_0, \tilde{T}_0\}$ and the u-th interfering radar $\{f_0, h_u, T_u, \tilde{T}_u\}$ as well as their relative time offset at l-th chirp cycle $\tau_{u,l}$. The u-th interference at the l-th pulse turns out to be a chirp signal [69]

$$x^i_{l,u}(t) = a^i_u e^{j2\pi\phi^i_{l,u}(t)},\ \forall t \in \mathcal{T}^i_{l,u}, \tag{3.5}$$

where a^i_u is the IF amplitude of interference u, the phase term is given as

$$\phi^i_{l,u}(t) = 0.5(h_u - h_0)t^2 - (h_u\tau_{u,l} - f^i_{D,u})t + \phi^i_{l,u,0}, \tag{3.6}$$

with $f^i_{D,u}$ denoting the Doppler frequency of interference u and $\phi^i_{l,u,0}$ denoting initial phase difference between interferer and victim radar at the l-th pulse, and $\mathcal{T}^i_{l,u}$ denotes the contaminated fast-time interval of the l-th pulse due to the u-th interference

$$\mathcal{T}^i_{l,u} = \left\{ t \,\middle|\, \left|(h_u - h_0)t - (h_u\tau_{u,l} - f^i_{D,u})\right| \le f_L \right\}, \tag{3.7}$$

which is determined from the fact that the interference signal $x^i_{l,u}(t)$ must lie in the IF band of the victim radar with IF bandwidth f_L. Figure 3.2 provides an illustrative example of two FMCW pulses where the interfering radars yield different chirp-like interference patterns, while the target signatures in the fast-time-frequency domain remain the same.

3.3 Proposed Target Reconstruction Method under Incoherent Interference

Our goal is to find an estimator $\hat{x}^o_{l,k}(t)$ to estimate each target component $x^o_{l,k}(t)$ from the multi-component signal $x_l(t)$ in (3.2). Our target signal estimation is achieved by separating the targets from the interference in the fTF domain via high-resolution time-frequency tools, identifying the target ridge by utilizing the consistent patterns of the target and varying patterns of the interference, and directly reconstructing target signals via the fTFMR. After each target signal's estimation, we estimate and detect the target's range and velocity using the conventional range-velocity DFT and CFAR detection introduced in Chapter 2.

3.3.1 High-Resolution Fast-Time-Frequency Representation

For the l-th pulse, the fast-time samples of the received signal $x_l(t)$ can be transformed to the fTF representation $X_l(t,\omega)$ via standard time-frequency analysis such as the STFT as adopted by several fast-time MIM methods [47, 57, 71, 72]. In contrast to these methods focusing on the interference patterns, we propose to use the FSST [5, 48, 64, 65] that highly focuses on the target pattern and allows fTFMR, and directly reconstruct the fast-time target signals from the focused target portions of the fTF representation with limited inclusion of interference and noise.

The FSST can be considered as a frequency-domain reassignment of the STFT. Given the STFT of $x_l(t)$

$$V_{x_l}^{g}(t,\omega) = \int_{\mathbb{R}} x_l(\tau) g^*(\tau - t) e^{-i\omega\tau} d\tau, \tag{3.8}$$

where $g(t)$ is the time-domain window function, $(\cdot)^*$ denotes the complex conjugate, and ω is the frequency variable, its centroid (local energy) of the spectrogram, i.e., $|V_{x_l}^{g}(t,\omega)|^2$, can be computed as [4]

$$\hat{\omega}_{x_l}(t,\omega) = \omega - \Im\left\{ \frac{V_{x_l}^{g'}(t,\omega)}{V_{x_l}^{g}(t,\omega)} \right\}, \tag{3.9}$$

where $V_{x_l}^{g'}(t,\omega)$ denotes the STFT with the window function give by the derivative of $g(t)$, and $\Im\{\cdot\}$ takes the imaginary part of the input. The FSST reassigns the STFT from the point of computation to its centroid along the frequency (ω) domain over each fast-time instant t [5, 48]

$$X_l(t,\omega) = \frac{\int_{\mathbb{R}} V_{x_l}^{g}(t,v) e^{i\omega t} \delta\left(\omega - \hat{\omega}_{x_l}(t,v)\right) dv}{2\pi g^*(0)}, \tag{3.10}$$

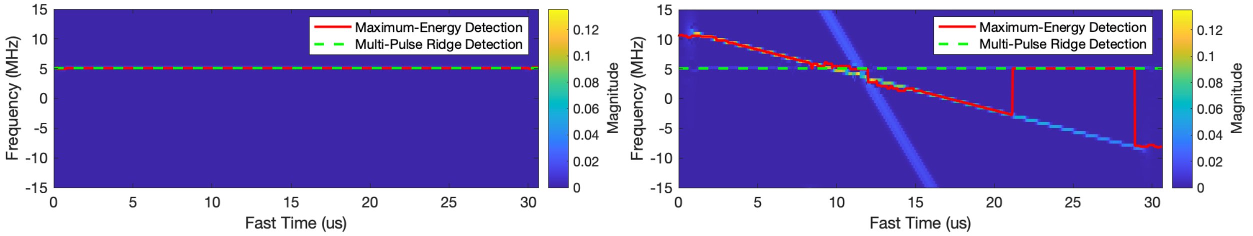

(a) fTF representation and ridge detection in a pulse

(b) fTF representation and ridge detection in another pulse

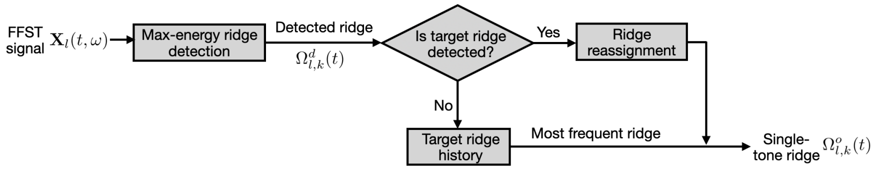

(c) Flow chart of multi-pulse ridge detection

Figure 3.3: Robust ridge detection exploits consistent target signatures and varying interference signatures from multiple pulses. (© 2022 IEEE)

where $\delta(\cdot)$ denotes the Dirac function. As detailed analyzed in [65], the FSST-based fTFR highly focuses on sinusoid-like target signals; see Figure 3.1 (a) for an illustration.

3.3.2 Robust Ridge Detection of Underwhelmed Targets

Reconstructing the target $x^o_{l,k}(t) = a^o_{l,k}e^{j2\pi\phi^o_{l,k}(t)}$ requires separating it from interference and other target signals. This can be done by detecting its ridge $\Omega^o_{l,k}(t)$ in the fTF domain, i.e., the estimation of its instantaneous frequency $d\phi^o_{l,k}(t)/dt$. As each target is a single-tone signal (as shown in (3.4)), the target ridge $\Omega^o_{l,k}(t)$ is a constant function of t and is a straight line in the fTF representation. As shown in Figure 3.3 (a) and (b), the target ridge stays the same over the multiple pulses within a coherent processing interval (CPI), while the FMCW interference ridges are likely to vary over multiple pulses due to the non-coherence between the interfering and victim radars.

The above observation leads us to propose a multi-pulse ridge detection method, given in Figure 3.3 (c). It first deploys, at each pulse, a maximum-energy ridge detector that uses a penalized forward-backward greedy algorithm [15] to sequentially detect the strongest signal ridge. The detected target ridges are denoted as $\Omega^d_{l,k}(t)$. Figure 3.3 (a) and (b) show the detected target ridges when there is only a target in a pulse and, respectively, when there are two interference signals and one target in another pulse. It is noted that the detected ridges may be a mixture of targets and interference.

Next, we validate whether the detected ridges indeed correspond to the target, and correct them using confirmed target ridges from other pulses in the same CPI if necessary. We first validate the detected ridges by checking if

$$\sum_{n=1}^{N} \mathbf{1}\big(\Omega^d_{l,k}(n\Delta T) = \mathrm{mode}(\{\Omega^d_{l,k}(n\Delta T), n = 1, \ldots, N\})\big) > N^{TH}, \tag{3.11}$$

where N is the number of time bins in the fTF domain, ΔT is the time resolution of the fTF such that $N\Delta T = T_0$, mode$(\cdot)$ means the value that appears the most often in a set of values, N^{TH} is a threshold.

- If the target ridge is *detected*, we reassign the target ridge to be a constant function over the fast time with the beat frequency equal to the most frequent bin of the detected ridge:

$$\Omega^o_{l,k}(t) = \mathrm{mode}(\{\Omega^d_{l,k}(n\Delta T), n = 1, \ldots, N\}). \tag{3.12}$$

- If the target ridge is *not* detected, we resort to the history of the most frequent ridge over multiple pulses in the same CPI and assign it to the target ridge in this pulse l,

$$\Omega^o_{l,k}(t) = \mathrm{mode}(\{\Omega^o_{l',k}(t), l' = [1, \ldots, L]\backslash\{l\}\}), \tag{3.13}$$

  where L is the number of pulses in a CPI. For instance of Figure 3.3 (b), the detected ridge $\Omega^d_{l,k}(t)$ fails to pass the validation of (3.11) and the target ridge is re-assigned by looking into the target ridges from other pulses.

3.3.3 Fast-Time-Frequency Mode Retrieval of Targets

The final step is to directly reconstruct the target signal $x^o_{l,k}(t)$ from its fTF representation $X_l(t,\omega)$ and the detected target ridge $\Omega^o_{l,k}(t), k = 1, 2, \ldots, K^o$. To avoid introducing interference component on the target ridge $\Omega^o_{l,k}(t)$, the tTFMR uses the interference-free time region along the detected ridges

$$\hat{X}_{l,k}(t,\omega) = \begin{cases} X_l(t,\omega), & t \in \hat{\mathcal{T}}^o_{l,k}(\omega), |\omega - \Omega^o_{l,k}(t)| < \epsilon, \\ 0, & \text{otherwise,} \end{cases}$$

where $\hat{\mathcal{T}}^o_{l,k}(\omega)$ is the estimated interference-free time region of the target ridge k. Then, the fTFMR directly integrates $\hat{X}_{l,k}(t,\omega)$ over a small frequency interval around $\Omega^o_{l,k}(t)$:

$$\hat{x}^o_{l,k}(t) = \frac{1}{g(0)} \int_{|\omega - \Omega^o_{l,k}(t)| < \epsilon} \hat{X}_{l,k}(t,\omega) d\omega, \tag{3.14}$$

where $\hat{x}^o_{l,k}(t)$ is the reconstructed fast-time signal of target k.

To obtain $\hat{\mathcal{T}}^o_{l,k}(\omega)$, one can estimate the interference-free time bins on

$$\mathcal{X}_l(\omega) \triangleq \{|X_l(n\Delta T,\omega)|^2, n = 1, 2, \ldots, N\}$$

for each frequency bin satisfying $\{\omega : |\omega - \Omega^o_{l,k}(t)| < \epsilon\}$ using the median absolute deviation (MAD) detector [60]. The MAD detector estimates the interference-free time bin $o \in \mathcal{O}_{l,k}$ if

$$\begin{aligned} &||X_l(o\Delta T,\omega)|^2 - \text{median}(\mathcal{X}_l(\omega))| < \\ &\gamma^{MAD} \underset{i=1,2,\ldots,N}{\text{median}}(||X_l(i\Delta T,\omega)|^2 - \text{median}(\mathcal{X}_l(\omega))|). \end{aligned}$$

The MAD detector is used to ensure the outliers on the target ridge (regarded as interference) are excluded as much as possible. Then, the interference-free time region of the target k is estimated as

$$\hat{\mathcal{T}}^{MAD}_{l,k}(\omega) = \bigcup_{o \in \mathcal{O}_{l,k}} [(o-1)\Delta T, o\Delta T]. \tag{3.15}$$

Furthermore, to retain the target portion as much as possible, one can compare each element in $\mathcal{X}_l(\omega)$ with the power profile of target k, i.e., $\mathcal{P}_{l,k} = \{|X_{l'}(n\Delta T,\omega)|^2, n =$

$1, \ldots, N,\ l' = 1, \ldots, l-1\}$, and determine the set of time bins corresponding to target k

$$\mathcal{Q}_{l,k} = \{q : |X_l(q\Delta T, \omega)|^2 < \gamma^{His}\text{median}(\mathcal{P}_{l,k})\}, \tag{3.16}$$

where γ^{His} is the target detection threshold in the power profile. Then, the interference-free portion of the target k is estimated as

$$\hat{\mathcal{T}}_{l,k}^{His}(\omega) = \bigcup_{q \in \mathcal{Q}_{l,k}} [(q-1)\Delta T, q\Delta T]. \tag{3.17}$$

Finally, we combine the results in (3.15) and (3.17), and obtain the estimated interference-free portion for target k as

$$\hat{\mathcal{T}}_{l,k}^{o}(\omega) = \hat{\mathcal{T}}_{l,k}^{MAD}(\omega) \cup \hat{\mathcal{T}}_{l,k}^{His}(\omega). \tag{3.18}$$

Denoting $\mathcal{T}_{l,k}^{o}(\omega)$ as the true interference-free time region of the target k on frequency ω, we have the following performance guarantee of the mode reconstruction.

Theorem 1 (Reconstruction Performance Guarantee) *There exists a constant* C *such that for all* $t \in \bigcap_{\omega : \left|\omega - \frac{d\phi_{l,k}^{o}(t)}{dt}\right| < \epsilon} \mathcal{T}_{l,k}^{o}(\omega)$,

$$\left| \frac{1}{g(0)} \int_{\left|\omega - \frac{d\phi_{l,k}^{o}(t)}{dt}\right| < \epsilon} X_l(t, \omega) d\omega - x_{l,k}^{o}(t) \right| \leq C\epsilon. \tag{3.19}$$

Proof 5 *By [48], for all interference-free time* $\bigcap_{\omega : \left|\omega - \frac{d\phi_{l,k}^{o}(t)}{dt}\right| < \epsilon} \mathcal{T}_{l,k}^{o}(\omega)$, (3.19) *holds for target* k.

Theorem 1 indicates that, when the detected ridge $\Omega_{l,k}^{o}(t)$ is close to the instantaneous frequency $d\phi_{l,k}^{o}(t)/dt$ and the estimated interference-free time region $\hat{\mathcal{T}}_{l,k}^{o}(\omega)$ is close to the real interference-free time region $\mathcal{T}_{l,k}^{o}(\omega)$, the reconstructed signal $\hat{x}_{l,k}^{o}(t)$ given by (3.14) is a good estimator of original target signal $x_{l,k}^{o}(t)$.

3.4 Performance Evaluation

In this section, we provide a numerical evaluation of the proposed fTFMR-based MIM method using synthetic data generated corresponding to a typical medium-range automotive radar configurations [51]. Moreover, we include the following baseline methods for performance comparison.

- Time-domain zeroing (Time-Zeroing) [66, 68]: The victim radar detects interference in the fast-time domain and nulls the interference.
- Iterative method with adaptive thresholding (IMAT) [11]: IMAT is based on Time-Zeroing and employs a sparse sampling procedure to reconstruct the contaminated fast-time samples from the uncontaminated portion.
- STFT-Zeroing [71]: STFT-Zeroing detects interference in the STFT-based fTF representation using a cell-average constant false alarm rate (CA-CFAR) detector, removes the interference, and finally transforms the modified fTF representation back to the fast-time domain.

We also include the interference-free and no mitigation to set the best and worse performance benchmarks.

3.4.1 Simulation Setup

We consider a scenario of 1 non-fluctuating target and 1 victim radar with FMCW configuration parameters given in Table 3.1 for a typical automotive radar operating in 77 GHz [51]. In the same scenario, we include 5 interferers with relative distances to the victim radar, chirp rates, and inter-chirp idle duration randomly (uniformly) distributed according to the last three rows of Table 3.1.

The synthetic data is generated using a system-level simulator based on MATLAB Phased Array System Toolbox. It consists of the FMCW waveform generation, the backscattering

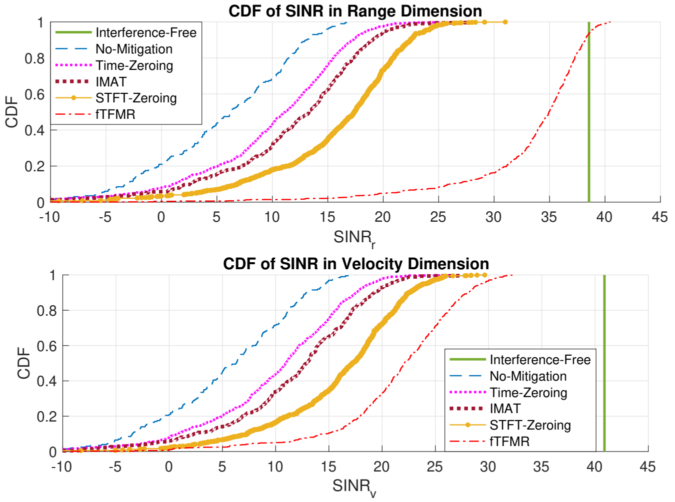

Figure 3.4: CDFs of SINR$_r$ and SINR$_v$. (© 2022 IEEE)

of the FMCW waveform from a target, interference channel propagation, and a standard FMCW signal processing (e.g., dechirping, low-pass filtering, range-velocity processing, and CFAR detection, etc.) at the receiver.

Simulation parameters are chosen as follows. For the proposed fTFMR method, the FSST uses a Kaiser window of length 256 and shape parameter 10 and an overlapping size of 255, while $N^{TH} = 3/8N$, $\gamma^{His} = 2.5$, ϵ is the width of 4 frequency bins in fTF domain, and the threshold for the MAD detection is 1.2. For the considered baseline methods, the threshold of the MAD detection is 4.4 for the Time-Zeroing and IMAT methods. The STFT-Zeroing uses a Hann window of length 128, an overlapping size of 96, and an FFT length of 256.

3.4.2 Performance Measures

The following performance measures are used for performance comparison.

- SINR in range dimension, $SINR_r$:

$$SINR_r = \frac{|\mathbf{S}^{RV}[n_o, m_o]|^2}{\sum\limits_{n \in \mathcal{N}_r \setminus \{n_o\}} |\mathbf{S}^{RV}[n, m_o]|^2 / (N_r - 1)}, \tag{3.20}$$

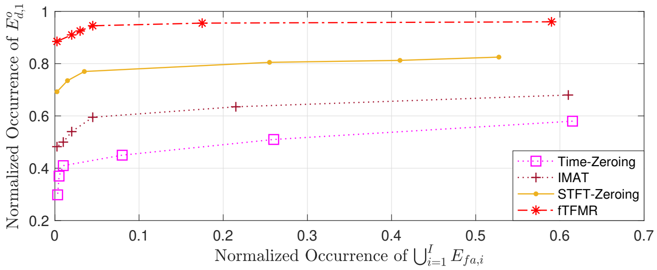

Figure 3.5: Target detection counts on target bins and false detection counts on non-target bins normalized over 200 Monte-Carlo runs. (© 2022 IEEE)

where $\mathbf{S}^{RV}$ is the RV spectrum after RV FFT, $\mathcal{N}_r$ is the set of range bins and $N_r = |\mathcal{N}_r|$.

- SINR in velocity dimension, $SINR_v$:

$$SINR_v = \frac{|\mathbf{S}^{RV}[n_o, m_o]|^2}{\sum\limits_{m \in \mathcal{M}_v \backslash \{m_o\}} |\mathbf{S}^{RV}[n_o, m]|^2/(M_v - 1)}, \tag{3.21}$$

  where $\mathcal{M}_v$ is the set of velocity bins and $M_v = |\mathcal{M}_v|$.

- *Target detection counts* on target bins are defined as the occurrence of $\bigcap_{k=1}^{K^o} E^o_{d,k}$ over Monte-Carlo runs, where $E^o_{d,k}$ is the event that the radar's CFAR detector detects a peak on its range-velocity bin, given that target k exists on this range-velocity bin.

- *False detection counts* on non-target bins are defined as the occurrence of $\bigcup_{i=1}^{I} E_{fa,i}$ over Monte-Carlo runs, where I is the total number of detected peaks, and $E_{fa,i}$ is defined similarly as $E^o_{d,k}$ except that the peak i does not corresponds to a target.

It is worth noting that $SINR_r$ and $SINR_v$ are the two measures widely used in the literature [66].

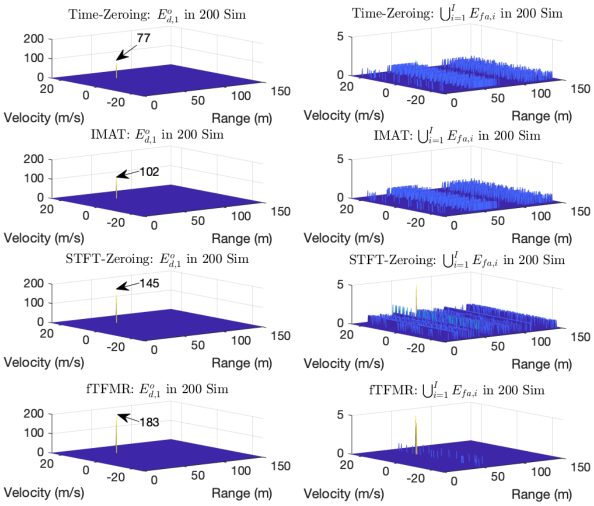

Figure 3.6: Heatmap of detection counts on the range-velocity domain over 200 Monte-Carlo runs. (© 2022 IEEE)

3.4.3 SINR Comparison

Figure 3.4 shows the cumulative distribution function (CDF) of $SINR_r$ and $SINR_v$ over 1000 Monte-Carlo runs. It is seen that all considered MIM methods outperform the case of No-Mitigation. The Time-Zeroing and IMAT methods provide similar performance, as previously observed in [66] and [68]. It is clear to see that the proposed fTFMR method achieves higher $SINR_r$ and $SINR_v$ than all baseline methods. It is interesting to note that the fTFMR also filters out the noise that spreads over the fTF domain as (3.14) integrates only the fTF portion confined to the target. This may lead to a higher $SINR_r$ than that of the Interference-Free case as the denominator of (3.20) is smaller for the fTFMR method. Comparing Figure 3.4 (a) and Figure 3.4 (b) reveals that the SINR gain in the range domain is larger than that in the velocity domain as the current fTFMR method only mitigates the interference in the fast-time (range) domain.

3.4.4 Detection Performance Comparison

Figure 3.5 plots the normalized occurrence of $E^o_{d,1}$ versus the normalized occurrence of $\bigcup_{i=1}^{I} E_{fa,i}$ over 200 Monte-Carlo runs of randomly simulated interference. For each method, the curve is obtained by changing the threshold used in the 2D (range-velocity) CA-CFAR detection. The result shows that the fTFMR method outperforms the baseline methods to achieve the highest probability of detection among all considered methods.

To visualize the detection and false alarm performance, Figure 3.6 plot the heatmap of the occurrence of $E^o_{d,1}$ and $\bigcup_{i=1}^{I} E_{fa,i}$ over the range-velocity domain. For each method, we run the 2D CA-CFAR detection over all range-velocity bins and report the total counts of detection as a 2D heatmap. In the left column, the total counts over the true target bin are reported, where the fTFMR method gives the highest counts of detection. The right column, on the other hand, reports the total counts over all non-target bins which represents a qualitative assessment of the false detection distribution over the RV domain. It is clear to see that the fTFMR method shows a cleaner false alarm heatmap than other methods.

3.5 Summary

In this chapter, we considered using the fTFMR to improve range-velocity (Doppler) detection performance. The idea is totally different from the existing fast-time domain schemes which focus on detect-and-cancel interference. In contrast, we focused on directly recovering target signals. Specifically, we proposed to use a high-resolution fast-time-frequency transform to have a better separation between the target and interference, robust ridge detection of underwhelmed target by using information from multiple chirp pulses, and a direct fast-time-frequency mode retrieval. Comprehensive performance comparison confirms significant performance gain of the proposed method over a long list of fast-time domain baseline methods, including the state-of-the-art STFT-Zeroing scheme [71], under strong interference.

Table 3.1: Simulation setup parameters. (© 2022 IEEE)

Transmit power (noise figure)	5dBm (4.5dB)
Transmit (receive) antenna gain	36(42)dBi
RF frequency	77GHz
Chirp bandwidth	460MHz
Victim radar's chirp sweep duration	30.7us
Victim radar's inter-chirp idle duration	7us
Victim radar's chirp slope	15MHz/us
IF bandwidth (ADC complex sample rate)	15MHz (16.7 MHz)
Number of chirps in a CPI	256
Range (Velocity) DFT size	512 (256)
Radar detector	2D CA-CFAR
CA-CFAR training (guard) size	5 (3) for row & column
Target model	Non-fluctuating
Target's RCS	20dBsm
Target's distance (velocity)	50m (12.1m/s)
Target (interference) channel	Free-space two-way (one-way) channel
Interferer's distance	$U(0, 10)$m
Interferer's chirp rate	$U(10, 20)$MHz/us
Interferer's inter-chirp idle duration	$U(6, 8)$us

Chapter 4

SPATIAL DETECTOR DESIGN FOR MITIGATING INCOHERENT INTERFERENCE

4.1 Motivation

Very few existing papers focus on MIMO-FMCW radar MIM. [10] shows that a virtual array can be used for detecting targets but only beamforming at Rx array can be used for interference suppression. [16] suggests adopting hybrid beamforming at Rx array to reduce beamforming costs while improving signal-to-interference-plus-noise ratio (SINR). [13] designs slow-time pseudo-random phase code to mitigate interference assuming interferers' slow-time pseudo-random phase codes are known. Despite these prior arts, there is no interference signal formulation of the state-of-the-art MIMO-FMCW radar. The signal processing based on the MIMO-FMCW signal modeling can be very important but is missing. In addition, for the next-generation massive MIMO radar [22], the analysis of its advantage on mutual automotive FMCW radar interference mitigation is also missing.

In this chapter, we investigate MIMO-FMCW radar incoherent interference from the spatial MIMO detection perspective. We consider adopting slow-time pseudo-random phase-code-based DDM waveform separation for MIMO-FMCW radar because this scheme does not suffer from reducing maximum unambiguous detectable velocity, which is important for automotive radar [61]. Furthermore, under the MIMO-FMCW mutual radar interference scenario, we also extend our investigation on the next-generation massive MIMO radar.

Our contributions are listed below.

- We are the first to derive the interfered signal model in the existence of mutual MIMO-FMCW interference and formulate a hypothesis testing problem considering the interference structure.

- We derive a subspace-based generalized likelihood ratio test (GLRT) solution of the proposed hypothesis testing problem, obtain a closed-form detection performance of the proposed subspace-based detector, and show that the proposed subspace-based detector is a constant false alarm rate (CFAR) detector.

- We extend our analysis to the FMCW based massive MIMO radar, which achieves perfect detection performance under interference when the Tx or Rx array size goes to infinity. In practice, we derive the closed-form massive MIMO regime where the proposed subspace-based detector is guaranteed to achieve a high enough detection probability under the interference.

- We validate the proposed subspace-based detector in MATLAB Phased Array System Toolbox, which considers real-world impairments, and we show that the proposed subspace-based detector achieves great interference suppression performance even with these impairments. Further, the simulator also validates the effectiveness of massive MIMO for MIM.

Major materials of this chapter will be presented in the author's forthcoming papers [35, 36].

4.2 Radar Signal Model under Interference

4.2.1 Target Signal Model

As shown in Fig. 1.1, we consider a victim radar of M Tx antennas and N Rx antennas with K pulses on each Tx antenna per coherent processing interval (CPI). The FMCW waveform of the victim radar is

$$s(t) = e^{j\pi\beta t^2} D_{0,T}(t), \tag{4.1}$$

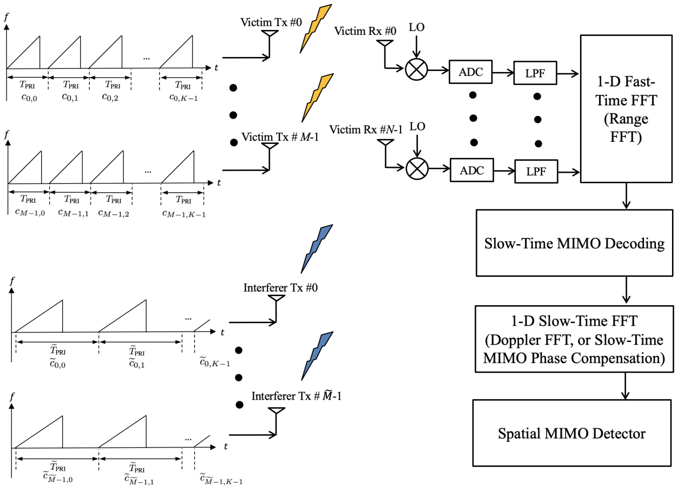

Figure 4.1: The slow-time MIMO-FMCW automotive radar architecture in existence of MIMO-FMCW interference.

where β is the chirp slope of the victim radar, T is the chirp duration of the victim radar, and

$$D_{a,b}(t) = \begin{cases} 1, & a \leq t \leq b \\ 0, & \text{otherwise.} \end{cases} \tag{4.2}$$

The RF waveform on Tx antenna m over K pulses is [73]

$$s_m(t) = \sum_{k=0}^{K-1} c_{k,m} s(t - kT_{\text{PRI}}) e^{j2\pi f_c (t - kT_{\text{PRI}})}, \tag{4.3}$$

where $c_{k,m}$ is the slow-time MIMO code on m-th Tx antenna and k-th pulse, T_{PRI} is the pulse repetition interval of the victim radar and f_c is the carrier frequency. For a target of range R and relative radial velocity v, the round-trip propagation delay from victim radar's m-th Tx antenna to its n-th receiving antenna is [73]

$$\tau_{m,n}(t) = 2\frac{R + vt}{c} + m\frac{d_t \sin(\phi_t)}{c} + n\frac{d_r \sin(\phi_r)}{c}, \tag{4.4}$$

where d_t and d_r are the Tx and Rx antenna element spacings, ϕ_t and ϕ_r are the Tx and Rx angles for the target, and c is the speed of propagation. If the target is in the far field, we have the approximation $\phi_t = \phi_r$. The n-th receiver of the victim radar in Fig. 1.1 receives the backscattered RF signal [73]

$$\begin{aligned} s_n^s(t) =& \alpha \sum_{m=0}^{M-1} s_m(t - \tau_{m,n}(t)) \\ \approx& \alpha e^{-j2\pi f_c \tau} \sum_{m=0}^{M-1} \sum_{k=0}^{K-1} c_{k,m} s(t - kT_{\text{PRI}} - \tau) \\ &\times e^{j2\pi f_c (t-kT_{\text{PRI}})} e^{-j2\pi(f_{\phi_t} m + f_{\phi_r} n)} e^{-j2\pi f_c \frac{2vt}{c}}, \end{aligned} \tag{4.5}$$

where α is the received complex amplitude of the target, $\tau = \frac{2R}{c}$ is the reference round-trip propagation delay, $\lambda = \frac{c}{f_c}$ is the RF wavelength, $f_{\phi_t} = d_t \frac{\sin(\phi_t)}{\lambda}$ and $f_{\phi_r} = d_r \frac{\sin(\phi_r)}{\lambda}$ are the normalized spatial frequency at the transmitting and receiving antennas [73]. After mixing $s_n^s(t)$ with the local oscillator (LO) signal in Fig. 1.1, we obtain the analog beat signal from the n-th Rx antenna

$$\begin{aligned} a_n^s(t) =& s_n^s(t) \sum_{k=0}^{K-1} s^*(t - kT_{\text{PRI}}) e^{-j2\pi f_c (t-kT_{\text{PRI}})} \\ =& \alpha_\tau \sum_{m=0}^{M-1} e^{-j2\pi f_c \frac{2vt}{c}} e^{-j2\pi(f_{\phi_t} m + f_{\phi_r} n)} \\ &\times \sum_{k=0}^{K-1} c_{k,m} e^{-j2\pi\beta(t-kT_{\text{PRI}})\tau} D_{\tau,T}(t - kT_{\text{PRI}}), \end{aligned} \tag{4.6}$$

where $\alpha_\tau \triangleq \alpha e^{-j2\pi f_c \tau} e^{j\pi\beta\tau^2}$. Next, passing $a_n^s(t)$ into a low-pass filter (LPF) of bandwidth f_L, and we consider the beat frequency of the target $\beta\tau < f_L$, we have the low-pass filtered signal $a_n^{s,low}(t) = a_n^s(t)$. Then, the low-pass filtered signal $a_n^{s,low}(t)$ signal is sampled by an analog-to-digital converter (ADC) at $t = kT_{\text{PRI}} + l\Delta T$ with ΔT and T_{PRI} denoted as the fast-time and slow-time sample intervals [73]:

$$\begin{aligned} a_n^s(l,k) =& a_n^{s,low}(kT_{\text{PRI}} + l\Delta T) \\ =& \alpha_\tau e^{-j2\pi f_r l} \mathbf{1}[l \in \mathcal{L}^s] \\ &\times \sum_{m=0}^{M-1} c_{k,m} e^{-j2\pi f_d k} e^{-j2\pi(f_{\phi_t} m + f_{\phi_r} n)}, \end{aligned} \tag{4.7}$$

where $\mathcal{L}^s \triangleq [\frac{\tau}{\Delta T}, \frac{T}{\Delta T}]$ is the set of signal sample indices, $f_r \triangleq (\beta\tau + \frac{2v}{\lambda})\Delta T$ is the normalized fast-time frequency, and $f_d \triangleq 2f_c T_{\mathrm{PRI}} v/c$ is the normalized target Doppler frequency [73]. Post L-length fast-time FFT (range FFT) on $a_n^s(l,k)$, we obtain the range spectrum of the received target signal on victim radar's n-th Rx antenna, l'-th range bin and k-th pulse

$$\begin{aligned} x_n^s(l',k) &= \sum_{l=0}^{L-1} a_n^s(l,k) e^{-j2\pi \frac{l'}{L} l} \\ &= \alpha_{l'} \sum_{m=0}^{M-1} c_{k,m} e^{-j2\pi f_d k} e^{-j2\pi (f_{\phi_t} m + f_{\phi_r} n)}, \end{aligned} \tag{4.8}$$

where $\alpha_{l'} \triangleq \sum_{l=0}^{L-1} \alpha_\tau \mathbf{1}[l \in \mathcal{L}^s] e^{-j2\pi (f_r + \frac{l'}{L}) l}$ is the complex amplitude of the target on range bin l'. If $M \leq K$, the slow-time MIMO code, e.g., the Chu sequence, has the near-orthogonal property [61]: $c_{k,m} c_{k,m}^* = 1$ and

$$\max_f \left| \sum_{k=0}^{K-1} c_{k,m} c_{k,m'}^* e^{-j2\pi f k} \right| \ll K, \ \forall m' \neq m. \tag{4.9}$$

Thus, the signal from m-th Tx antenna to target received by n-th Rx antenna on pulse k is decoded as

$$\begin{aligned} \widehat{x}_{m,n}^s(l',k) &= x_n^s(l',k) c_{k,m}^* \\ &= \alpha_{l'} \sum_{m'=0}^{M-1} c_{k,m'} c_{k,m}^* e^{-j2\pi f_d k} e^{-j2\pi (f_{\phi_t} m' + f_{\phi_r} n)}. \end{aligned} \tag{4.10}$$

Then, as shown in Fig. 1.1, applying K-length slow-time FFT (Doppler FFT), which aims at compensating the Doppler component $e^{-j2\pi f_d k}$ in $\widehat{x}_{m,n}^s(l',k)$ and separating target signals from different antennas, we obtain the spectrum on l'-th range bin and k'-th Doppler bin

$$\begin{aligned} y_{m,n}^s(l',k') &= \sum_{k=0}^{K-1} \widehat{x}_{m,n}^s(l',k) e^{-j2\pi \frac{k'}{K} k} \\ &= \alpha_{l'} \sum_{m' \neq m} \left(\sum_{k=0}^{K-1} c_{k,m'} c_{k,m}^* e^{-j2\pi (f_d + \frac{k'}{K}) k} \right) e^{-j2\pi (f_{\phi_t} m' + f_{\phi_r} n)} \\ &\quad + b(l',k') e^{-j2\pi (f_{\phi_t} m + f_{\phi_r} n)}, \end{aligned} \tag{4.11}$$

where $b(l',k') \triangleq \alpha_{l'} \left(\sum_{k=0}^{K-1} e^{-j2\pi(f_d+\frac{k'}{K})k}\right)$. Notice that when $f_d + \frac{k'}{K} = 0$, i.e., when the normalized target Doppler frequency just fall on the Doppler bin k', then $b(l',k') = K\alpha_{l'}$ indicating a peak on Doppler spectrum, and in this case

$$y^s_{m,n}(l',k') \approx b(l',k')e^{-j2\pi(f_{\phi_t}m+f_{\phi_r}n)} \tag{4.12}$$

due to (4.9). Thus, when $f_d + \frac{k'}{K} = 0$, stacking $\{y^s_{m,n}(l',k')\}$ into a vector, the $MN \times 1$ virtual array for target on range bin l' and Doppler bin k' is approximated by

$$\mathbf{y}^s(l',k') = b(l',k')\mathbf{a}_t \otimes \mathbf{a}_r. \tag{4.13}$$

where

$$\mathbf{a}_t \triangleq [1, e^{-j2\pi f_{\phi_t}}, \ldots, e^{-j2\pi f_{\phi_t}(M-1)}]^T, \tag{4.14}$$

is the $M \times 1$ victim radar's Tx steering vector to the target, and

$$\mathbf{a}_r \triangleq [1, e^{-j2\pi f_{\phi_r}}, \ldots, e^{-j2\pi f_{\phi_r}(N-1)}]^T \tag{4.15}$$

is the $N \times 1$ victim radar's Rx steering vector from the target.

4.2.2 Interference Signal Model

As shown in Fig. 4.1, we consider an interfering radar also using the MIMO-FMCW signaling scheme with $\widetilde{M}$ Tx antennas, and in general, $\widetilde{M} \neq M$. Similar to (4.3), the $\tilde{m}$-th interfering antenna sends slow-time coded (different from those codes at the victim radar) $\tilde{K}$ pulses

$$\widetilde{s}_{\widetilde{m}}(t) = \sum_{\widetilde{k}=0}^{\widetilde{K}-1} \widetilde{c}_{\widetilde{k},\widetilde{m}} \widetilde{s}(t - \widetilde{k}\widetilde{T}_{\text{PRI}} - \widetilde{\tau}_{syn}) e^{j2\pi f_c(t-\widetilde{k}\widetilde{T}_{\text{PRI}}-\widetilde{\tau}_{syn})}, \tag{4.16}$$

where the base FMCM waveform $\widetilde{s}(t)$ shares the same expression as (4.1) but with different chirp rate $\widetilde{\beta}$ and pulse duration $\widetilde{T}$, $\widetilde{\tau}_{syn}$ is the transmit synchronization delay (initial time offset) between the reference Tx antennas of the victim radar and the interfering radar, $\widetilde{c}_{\widetilde{k},\widetilde{m}}$ is the slow-time code of the interfering radar, and $\widetilde{T}_{\text{PRI}}$ is the PRI at the interfering radar.

For an interfering radar of range $\widetilde{R}$ and radial velocity $\widetilde{v}$ relative to the victim radar, the one-way propagation delay from its $\widetilde{m}$-th Tx antenna to the n-th receiving antenna of victim radar is

$$\widetilde{\tau}_{\widetilde{m},n}(t) = \frac{\widetilde{R}+\widetilde{v}t}{c} + \widetilde{m}\frac{\widetilde{d}_t\sin(\widetilde{\phi}_t)}{c} + n\frac{d_r\sin(\widetilde{\phi}_r)}{c}, \tag{4.17}$$

where $\widetilde{d}_t$ is the Tx antenna element spacing at the interferer, and $\widetilde{\phi}_t$ and $\widetilde{\phi}_r$ are the interferer's Tx and Rx angles for the victim radar. The n-th receiver of the victim radar in Fig. 1.1 receives the RF signal from the interferer

$$\begin{aligned} s_n^i(t) &= \widetilde{\alpha}\sum_{\widetilde{m}=0}^{\widetilde{M}-1}\widetilde{s}_{\widetilde{m}}(t-\widetilde{\tau}_{\widetilde{m},n}(t)) \\ &\approx \widetilde{\alpha}e^{-j2\pi f_c\widetilde{\tau}}\sum_{\widetilde{m}=0}^{\widetilde{M}-1}\sum_{\widetilde{k}=0}^{\widetilde{K}-1}\widetilde{c}_{\widetilde{k},\widetilde{m}}\widetilde{s}(t-\widetilde{k}\widetilde{T}_{\text{PRI}}-\widetilde{\tau}_{syn}-\widetilde{\tau}) \\ &\quad \times e^{j2\pi f_c(t-\widetilde{k}\widetilde{T}_{\text{PRI}}-\widetilde{\tau}_{syn})}e^{-j2\pi(\widetilde{f}_{\phi_t}\widetilde{m}+\widetilde{f}_{\phi_r}n)}e^{-j2\pi f_c\frac{\widetilde{v}t}{c}}, \end{aligned} \tag{4.18}$$

where $\widetilde{\alpha}$ is the received complex amplitude of the interference, $\widetilde{\tau} = \frac{\widetilde{R}}{c}$ is the reference one-way propagation delay from interferer to the victim radar, and $\widetilde{f}_{\phi_t} = \widetilde{d}_t\frac{\sin(\widetilde{\phi}_t)}{\lambda}$ and $\widetilde{f}_{\phi_r} = d_r\frac{\sin(\widetilde{\phi}_r)}{\lambda}$ are the normalized spatial frequency at the interferer transmitting antennas and victim receiving antennas.

Using victim radar's time as the reference time, we rewrite $\widetilde{k}\widetilde{T}_{\text{PRI}}+\widetilde{\tau}_{syn}, \widetilde{k} = 0, 1, \ldots, \widetilde{K}-1$ using the victim radar's slow-time index k. Define $\widetilde{\tau}'_{k,\widetilde{k}}$ as the time offset between the $\widetilde{k}$-th pulse of the interfering radar relative to the k-th LO pulse at the victim radar. Notice that each pulse duration PRI includes the chirp duration and the inter-chirp idle duration. Two necessary conditions for the $\widetilde{k}$-th pulse of the interfering radar be dechirped by the k-th pulse of victim radar are $-\widetilde{\tau}'_{k,\widetilde{k}} - \widetilde{T}_{\text{PRI}} < 0$ and $\widetilde{\tau}'_{k,\widetilde{k}} < T_{\text{PRI}}$, which in combination lead to $-\widetilde{T}_{\text{PRI}} < \widetilde{\tau}'_{k,\widetilde{k}} < T_{\text{PRI}}$. If any of these two conditions does not satisfy, as shown in Fig. 4.2, the $\widetilde{k}$-th pulse of the interfering radar cannot be dechirped by the k-th pulse of victim radar.

Define

$$\mathcal{K}_{\widetilde{k}} \triangleq \Big\{k : \widetilde{k}\widetilde{T}_{\text{PRI}} + \widetilde{\tau}_{syn} = kT_{\text{PRI}} + \widetilde{\tau}'_{k,\widetilde{k}}, -\widetilde{T}_{\text{PRI}} < \widetilde{\tau}'_{k,\widetilde{k}} < T_{\text{PRI}}, \\ k = 0, 1, \ldots, K-1\Big\},\ \widetilde{k} = 0, 1, \ldots, \widetilde{K}-1, \tag{4.19}$$

as a set that groups all pulses of the victim radar that intercept with the $\tilde{k}$ pulse by checking whether any time instant of the victim pulse falls within the $\tilde{k}$ interfering pulse.

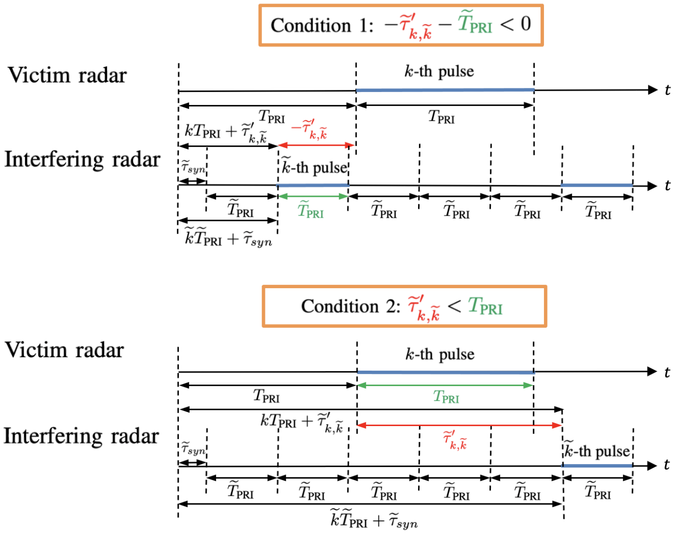

Figure 4.2: Two necessary conditions for the $\widetilde{k}$-th pulse of the interfering radar to be dechirped by the k-th pulse of the victim radar with a counterexample for each condition shown in the figure.

Let

$$\widetilde{c}^{\,\widetilde{k}}_{k,\widetilde{m}} \triangleq \begin{cases} \widetilde{c}_{\widetilde{k},\widetilde{m}}, & k \in \mathcal{K}_{\widetilde{k}} \\ 0, & \text{otherwise} \end{cases} \tag{4.20}$$

denote the slow-time code of the interfering radar observed at k-th victim radar pulse. Then, we rewrite $s_n^i(t)$ as

$$s_n^i(t) = \widetilde{\alpha} e^{-j2\pi f_c \widetilde{\tau}} \sum_{\widetilde{m}=0}^{\widetilde{M}-1} \sum_{\widetilde{k}=0}^{\widetilde{K}-1} \sum_{k \in \mathcal{K}_{\widetilde{k}}} \widetilde{c}^{\widetilde{k}}_{k,\widetilde{m}} \widetilde{s}(t - kT_{\mathrm{PRI}} - \widetilde{\tau}'_{k,\widetilde{k}} - \widetilde{\tau})$$
$$\times e^{j2\pi f_c (t - kT_{\mathrm{PRI}} - \widetilde{\tau}'_{k,\widetilde{k}})} e^{-j2\pi(\widetilde{f}_{\phi_t} \widetilde{m} + \widetilde{f}_{\phi_r} n)} e^{-j2\pi f_c \frac{\widetilde{v}t}{c}}. \tag{4.21}$$

The victim radar mixes $s_n^i(t)$ with its LO signal, and obtains the analog beat signal from the n-th Rx antenna

$$\begin{aligned} a_n^i(t) = {} & s_n^i(t) \sum_{k=0}^{K-1} s^*(t - kT_{\mathrm{PRI}}) e^{-j2\pi f_c (t - kT_{\mathrm{PRI}})} \\ = {} & \widetilde{\alpha} e^{-j2\pi f_c \widetilde{\tau}} \sum_{\widetilde{m}=0}^{\widetilde{M}-1} \sum_{\widetilde{k}=0}^{\widetilde{K}-1} \sum_{k \in \mathcal{K}_{\widetilde{k}}} \widetilde{c}^{\widetilde{k}}_{k,\widetilde{m}} e^{j\pi(\widetilde{\beta} - \beta)(t - kT_{\mathrm{PRI}})^2} \\ & \times e^{j\pi\widetilde{\beta}(\widetilde{\tau}'_{k,\widetilde{k}} + \widetilde{\tau})^2} e^{-j2\pi\widetilde{\beta}(t - kT_{\mathrm{PRI}})(\widetilde{\tau}'_{k,\widetilde{k}} + \widetilde{\tau})} \\ & \times e^{-j2\pi f_c \widetilde{\tau}'_{k,\widetilde{k}}} e^{-j2\pi(\widetilde{f}_{\phi_t} \widetilde{m} + \widetilde{f}_{\phi_r} n)} e^{-j2\pi f_c \frac{\widetilde{v}t}{c}} \\ & \times D_{\widetilde{\tau}'_{k,\widetilde{k}} + \widetilde{\tau}, \min\left\{T, \widetilde{\tau}'_{k,\widetilde{k}} + \widetilde{\tau} + \widetilde{T}\right\}}(t - kT_{\mathrm{PRI}}) \end{aligned} \tag{4.22}$$

From (4.22), we can see that the instantaneous frequency of interference at pulse k is $\widetilde{\beta}(\widetilde{\tau}'_{k,\widetilde{k}} + \widetilde{\tau}) - (\widetilde{\beta} - \beta)(t - kT_{\mathrm{PRI}})$. Then, passing $a_n^i(t)$ into the LPF of bandwidth f_L, the interference residential time on pulse k with interference is

$$0 < \widetilde{\beta}(\widetilde{\tau}'_{k,\widetilde{k}} + \widetilde{\tau}) - (\widetilde{\beta} - \beta)(t - kT_{\mathrm{PRI}}) < f_L. \tag{4.23}$$

Fig. 4.3 provides an illustrative example showing the interference residential time. The

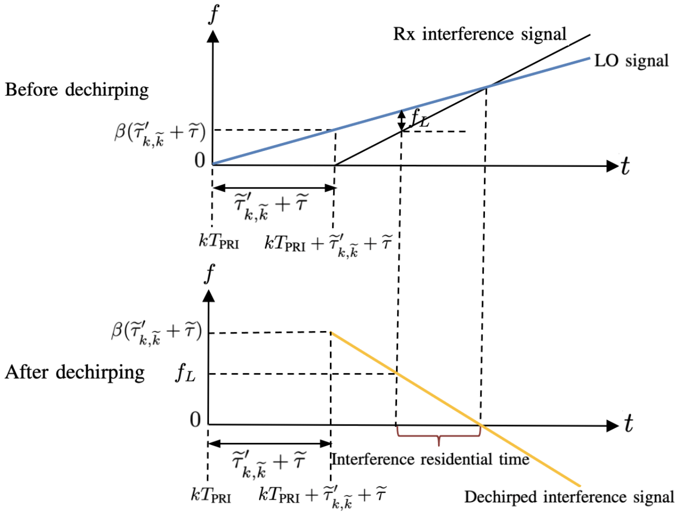

Figure 4.3: Interference at victim radar's pulse k.

low-pass filtered IF interference signal is

$$\begin{aligned}
a_n^{i,low}(t) = {} & \widetilde{\alpha} e^{-j2\pi f_c \widetilde{\tau}} \sum_{\widetilde{m}=0}^{\widetilde{M}-1} \sum_{\widetilde{k}=0}^{\widetilde{K}-1} \sum_{k \in \mathcal{K}_{\widetilde{k}}} \widetilde{c}_{k,\widetilde{m}}^{\widetilde{k}} e^{j\pi(\widetilde{\beta}-\beta)(t-kT_{\mathrm{PRI}})^2} \\
& \times e^{j\pi\widetilde{\beta}(\widetilde{\tau}'_{k,\widetilde{k}}+\widetilde{\tau})^2} e^{-j2\pi\widetilde{\beta}(t-kT_{\mathrm{PRI}})(\widetilde{\tau}'_{k,\widetilde{k}}+\widetilde{\tau})} \\
& \times e^{-j2\pi f_c \widetilde{\tau}'_{k,\widetilde{k}}} e^{-j2\pi(\widetilde{f}_{\phi_t}\widetilde{m}+\widetilde{f}_{\phi_r}n)} e^{-j2\pi f_c \frac{\widetilde{v}t}{c}} \\
& \times \mathbf{1}\left[0 < \widetilde{\beta}(\widetilde{\tau}'_{k,\widetilde{k}}+\widetilde{\tau}) - (\widetilde{\beta}-\beta)(t-kT_{\mathrm{PRI}}) < f_L\right] \\
& \times D_{\widetilde{\tau}'_{k,\widetilde{k}}+\widetilde{\tau},\min\left\{T,\widetilde{\tau}'_{k,\widetilde{k}}+\widetilde{\tau}+\widetilde{T}\right\}}(t-kT_{\mathrm{PRI}}). \qquad (4.24)
\end{aligned}$$

The low-pass filtered signal $a_n^{s,low}(t)$ signal is sampled by the ADC at $t = kT_{\mathrm{PRI}} + l\Delta T$:

$$\begin{aligned}
& a_n^i(l,k) = a_n^{i,low}(kT_{\mathrm{PRI}}+l\Delta T) \\
= & \widetilde{\alpha} e^{-j2\pi f_c \widetilde{\tau}} \sum_{\widetilde{m}=0}^{\widetilde{M}-1} \sum_{\widetilde{k}=0}^{\widetilde{K}-1} \widetilde{c}_{k,\widetilde{m}}^{\widetilde{k}} e^{j\pi\widetilde{\beta}(\widetilde{\tau}'_{k,\widetilde{k}}+\widetilde{\tau})^2} e^{-j2\pi f_c \widetilde{\tau}'_{k,\widetilde{k}}} \\
& \times e^{j\pi(\widetilde{\beta}-\beta)(l\Delta T)^2} e^{-j2\pi \widetilde{f}_{r,k,\widetilde{k}} l} \mathbf{1}\left[l \in \mathcal{L}_{k,\widetilde{k}}^i\right] \\
& \times e^{-j2\pi \widetilde{f}_d k} e^{-j2\pi(\widetilde{f}_{\phi_t}\widetilde{m}+\widetilde{f}_{\phi_r}n)} \qquad (4.25)
\end{aligned}$$

where $\mathcal{L}^i_{k,\widetilde{k}} \triangleq \left\{l : 0 < \widetilde{\beta}(\widetilde{\tau}'_{k,\widetilde{k}} + \widetilde{\tau}) - (\widetilde{\beta} - \beta) l \Delta T < f_L, (\widetilde{\tau}'_{k,\widetilde{k}} + \widetilde{\tau}) < l\Delta T < \min\left\{T, \widetilde{\tau}'_{k,\widetilde{k}} + \widetilde{\tau} + \widetilde{T}\right\}\right\}$ is the set of interference sample indices, $\widetilde{f}_{r,k,\widetilde{k}} \triangleq (\widetilde{\beta}(\widetilde{\tau}'_{k,\widetilde{k}} + \widetilde{\tau}) + \frac{\widetilde{v}}{\lambda})\Delta T$ is the normalized interference initial fast-time frequency, and $\widetilde{f}_d = f_c \frac{\widetilde{v} T_{\text{PRI}}}{c}$ is the normalized interference Doppler frequency. Post L-length fast-time FFT (range FFT) on $a^i_n(l,k)$, we obtain the range spectrum of the received interference signal on victim radar's n-th Rx antenna, l'-th range bin and k-th pulse

$$\begin{aligned} x^i_n(l',k) &= \sum_{l=0}^{L-1} a^i_n(l,k) e^{-j2\pi \frac{l'}{L} l} \\ &= \sum_{\widetilde{m}=0}^{\widetilde{M}-1} \widetilde{\alpha}_{l',k,\widetilde{m}} e^{-j2\pi \widetilde{f}_d k} e^{-j2\pi(\widetilde{f}_{\phi_t} \widetilde{m} + \widetilde{f}_{\phi_r} n)} \end{aligned} \tag{4.26}$$

where

$$\begin{aligned} \widetilde{\alpha}_{l',k,\widetilde{m}} \triangleq\ & \widetilde{\alpha} e^{-j2\pi f_c \widetilde{\tau}} \sum_{\widetilde{k}=0}^{\widetilde{K}-1} \widetilde{c}^{\widetilde{k}}_{k,\widetilde{m}} e^{j\pi \widetilde{\beta} (\widetilde{\tau}'_{k,\widetilde{k}} + \widetilde{\tau})^2} e^{-j2\pi f_c \widetilde{\tau}'_{k,\widetilde{k}}} \\ & \times \sum_{l=0}^{L-1} e^{j\pi(\widetilde{\beta} - \beta)(l\Delta T)^2} \mathbf{1}\left[l \in \mathcal{L}^i_{k,\widetilde{k}}\right] e^{-j2\pi(\widetilde{f}_{r,k,\widetilde{k}} + \frac{l'}{L}) l} \end{aligned} \tag{4.27}$$

is the coded complex amplitude of the interference on range bin l' and pulse k. Notice that $\widetilde{\alpha}_{l',k,\widetilde{m}}$ varies with pulse index k because $\widetilde{\tau}'_{k,\widetilde{k}}$ varies with k. Also, as $\widetilde{\beta}$ and $\widetilde{\tau}'_{k,\widetilde{k}}$ are unknown by the victim radar, $\widetilde{\alpha}_{l',k,\widetilde{m}}$ is unknown by the victim radar. The signal from m'-th interferer's Tx antenna to n-th victim radar's Rx antenna on victim radar's pulse k follows the same MIMO Tx signal separation procedure as the target. Thus, the interference spectrum on victim radar's l'-th range bin and k'-th Doppler bin is

$$\begin{aligned} y^i_{m,n}(l',k') &= \sum_{k=0}^{K-1} x^i_n(l',k) c^*_{k,m} e^{-j2\pi \frac{k'}{K} k} \\ &= \sum_{\widetilde{m}=0}^{\widetilde{M}-1} \sum_{k=0}^{K-1} \widetilde{\alpha}_{l',k,\widetilde{m}} c^*_{k,m} e^{-j2\pi(\widetilde{f}_d + \frac{k'}{K})k} e^{-j2\pi(\widetilde{f}_{\phi_t} \widetilde{m} + \widetilde{f}_{\phi_r} n)} \\ &= \widetilde{a}'_{t,m} e^{-j2\pi \widetilde{f}_{\phi_r} n}, \end{aligned} \tag{4.28}$$

where

$$\widetilde{a}'_{t,m} = \sum_{\widetilde{m}=0}^{\widetilde{M}-1} \sum_{k=0}^{K-1} \widetilde{\alpha}_{l',k,\widetilde{m}} c^*_{k,m} e^{-j2\pi(\widetilde{f}_d + \frac{k'}{K})k} e^{-j2\pi \widetilde{f}_{\phi_t} \widetilde{m}}. \tag{4.29}$$

Stacking $\{y^i_{m,n}(l', k')\}_{m,n}$ into a vector, we obtain the interference range-Doppler spectrum on a $MN \times 1$ virtual array

$$\mathbf{y}^i(l', k') = \widetilde{\mathbf{a}}'_t \otimes \widetilde{\mathbf{a}}_r. \tag{4.30}$$

where

$$\widetilde{\mathbf{a}}'_t \triangleq [\widetilde{a}'_{t,0}, \widetilde{a}'_{t,1}, \ldots, \widetilde{a}'_{t,M-1}]^T, \tag{4.31}$$

is the $M \times 1$ interferer's Tx steering vector decoded by the victim radar, and

$$\widetilde{\mathbf{a}}_r \triangleq [1, e^{-j2\pi \widetilde{f}_{\phi_r}}, \ldots, e^{-j2\pi \widetilde{f}_{\phi_r}(N-1)}]^T \tag{4.32}$$

is the $N \times 1$ victim radar's Rx steering vector from the interferer. Notice that although the interferer's Tx antenna number $\widetilde{M}$ may be different than the victim Tx antenna number M, $\widetilde{\mathbf{a}}'_t$ in (4.31) has dimension of M because the victim radar uses the conjugate of it's own MIMO code $\{c_{k,m}\}$ for decoding and MIMO Tx signal separation, as shown in (4.29).

4.2.3 Discussion

In this part, we validate that when interferer and victim radar are synchronized ($\widetilde{\tau}_{syn} = 0$), have the same waveform parameters ($\widetilde{\beta} = \beta$, $\widetilde{T}_{\text{PRI}} = T_{\text{PRI}}$, $\widetilde{T} = T$, $\widetilde{K} = K$), number of Tx antennas ($\widetilde{M} = M$) and slow-time MIMO code ($\{\widetilde{c}_{\widetilde{k},\widetilde{m}}\} = \{c_{k,m}\}$), the received interference signal, referred to as the coherent interference signal, has the same structure as the target signal [33].

Under the coherent interference step, by (4.19), we have $\tau'_{k,\widetilde{k}} = 0$ and $\mathcal{K}_{\widetilde{k}} = \{\widetilde{k}\}$. Then, by (4.20), we have $\widetilde{c}^{\widetilde{k}}_{k,\widetilde{m}} = \widetilde{c}_{k,\widetilde{m}} = c_{k,\widetilde{m}}$ if $k = \widetilde{k}$, and otherwise $\widetilde{c}^{\widetilde{k}}_{k,\widetilde{m}} = 0$; as here we consider the coherent interference is dechirped into the victim radar, i.e., $0 < \widetilde{\beta}\widetilde{\tau} < f_L$, we have $\mathcal{L}^i_{k,\widetilde{k}} = [\frac{\widetilde{\tau}}{\Delta T}, \frac{T}{\Delta T}]$; the normalized interference initial fast-time frequency reduces to $\widetilde{f}_{r,k,\widetilde{k}} = (\widetilde{\beta}\widetilde{\tau} + \frac{\widetilde{v}}{\lambda})\Delta T$. Based on these $\widetilde{\alpha}_{l',k,\widetilde{m}}$ in (4.27) becomes $\widetilde{\alpha}_{l',k,\widetilde{m}} = \widetilde{\alpha}_{l'} c_{k,\widetilde{m}}$, where $\widetilde{\alpha}_{l'} = \widetilde{\alpha} e^{-j2\pi f_c \widetilde{\tau}} e^{j\pi\widetilde{\beta}\widetilde{\tau}^2} \sum_{l=0}^{L-1} \mathbf{1}\left[l \in \mathcal{L}^i_{k,\widetilde{k}}\right] e^{-j2\pi(\widetilde{f}_{r,k,\widetilde{k}} + \frac{l'}{L})l}$. Then, the range-Doppler interference spectrum in (4.28) reduces to

$$\begin{aligned} & y^i_{m,n}(l',k') \\ =& \widetilde{\alpha}_{l'} \sum_{\widetilde{m} \neq m} \left(\sum_{k=0}^{K-1} c_{k,\widetilde{m}} c^*_{k,m} e^{-j2\pi(\widetilde{f}_d + \frac{k'}{K})k} \right) e^{-j2\pi(\widetilde{f}_{\phi_t}\widetilde{m} + \widetilde{f}_{\phi_r} n)} \\ & + \widetilde{b}(l',k') e^{-j2\pi(\widetilde{f}_{\phi_t} m + \widetilde{f}_{\phi_r} n)}, \end{aligned} \tag{4.33}$$

where $\widetilde{b}(l',k') \triangleq \widetilde{\alpha}_{l'} \left(\sum_{k=0}^{K-1} e^{-j2\pi(\widetilde{f}_d + \frac{k'}{K})k} \right)$. Notice that when $\widetilde{f}_d + \frac{k'}{K} = 0$, i.e., when the normalized interference Doppler frequency just fall on the Doppler bin k', then $\widetilde{b}(l',k') = K\widetilde{\alpha}_{l'}$ indicating a peak on Doppler spectrum, and in this case

$$y^i_{m,n}(l',k') \approx \widetilde{b}(l',k') e^{-j2\pi(\widetilde{f}_{\phi_t} m + \widetilde{f}_{\phi_r} n)} \tag{4.34}$$

due to (4.9). Comparing the target signal $y^s_{m,n}(l',k')$ in (4.12) and the interference signal $y^i_{m,n}(l',k')$ in (4.34), we validate that under the coherent interference case, the interference model derived in Section 4.2.2 has a similar structure compared to the target signal model derived in Section 4.2.1.

4.3 MIMO Detection under Interference

4.3.1 Hypothesis Testing

On each range-Doppler bin, we formulate MIMO radar detection under single interference and complex white Gaussian noise $\mathbf{z} \sim \mathcal{CN}(\mathbf{0}, \sigma^2 \mathbf{I}_{MN})$, where $\mathbf{I}_{MN}$ is the identity matrix of size MN[1]. The target's complex amplitude is unknown. We assume the victim radar's Rx steering vector from the interferer $\widetilde{\mathbf{a}}_r$ in (4.32) is known because a victim radar can

---

[1] For more general correlated noise with the covariance matrix $\mathbf{R}$, one can estimate $\mathbf{R}$ from homogeneous training data at neighboring range-Doppler cells. The object detection using whitened signal is equivalent to the problem here.

passively receive pure interference signal and estimate the normalized spatial frequency $\widetilde{f}_{\phi_r}$ in its idle time between 2 CPIs. As $\widetilde{\alpha}_{l',k,\widetilde{m}}$ in (4.27) is not known by the victim radar, we model $\widetilde{\mathbf{a}}_t'$ in (4.31) as an unknown vector. Omitting the range-Doppler bin index (l', k') in the following, we formulate the angle detection problem on any range bin l' and target Doppler bin $k' = -Kf_d$ as follows

Problem 1 (Target Detection with Interference)

$$\begin{cases} H_0, & \mathbf{y} = \widetilde{\mathbf{a}}_t' \otimes \widetilde{\mathbf{a}}_r + \mathbf{z} \\ H_1, & \mathbf{y} = b\mathbf{a}_t \otimes \mathbf{a}_r + \widetilde{\mathbf{a}}_t' \otimes \widetilde{\mathbf{a}}_r + \mathbf{z}. \end{cases} \tag{4.35}$$

4.3.2 Classic Correlation-based Detector

In the interference-free case, i.e., $\widetilde{\mathbf{a}}_t' = \mathbf{0}$, the GLRT detection statistics of Problem 1 is [37]

$$T^c(\mathbf{y}) = \frac{2}{\sigma^2}\frac{1}{MN}|\mathbf{y}^H(\mathbf{a}_t \otimes \mathbf{a}_r)|^2. \tag{4.36}$$

$T^c(\mathbf{y})$ suggests correlating $\mathbf{y}$ and target's virtual array steering vector $\mathbf{a}_t \otimes \mathbf{a}_r$, which can be easily realized using angle FFT and is widely adopted in current automotive radar systems [49,61]. In the following, we evaluate the performance of (4.36) under the interference case shown in Problem 1.

Lemma 1 *In Problem 1, the false alarm probability and probability of detection performance for the classic correlation solution in* (4.36) *are*

$$P_{FA}^c = Q_1\left(\sqrt{\lambda_0^c}, \sqrt{\gamma}\right), \tag{4.37}$$

$$P_D^c = Q_1\left(\sqrt{\lambda_1^c}, \sqrt{\gamma}\right), \tag{4.38}$$

where

$$\lambda_0^c = \frac{2}{MN\sigma^2}|g_t g_r|^2, \tag{4.39}$$

$$\lambda_1^c = \frac{2MN|b|^2}{\sigma^2}\left|1+\frac{g_t^* g_r^*}{bMN}\right|^2, \tag{4.40}$$

γ is the detection threshold,

$$g_t = \widetilde{\mathbf{a}}_t'^H \mathbf{a}_t \text{ and } g_r = \widetilde{\mathbf{a}}_r^H \mathbf{a}_r. \tag{4.41}$$

Proof 6 *Under H_0, we have $(\mathbf{a}_t \otimes \mathbf{a}_r)^H \mathbf{y} = (\mathbf{a}_t \otimes \mathbf{a}_r)^H (\widetilde{\mathbf{a}}_t' \otimes \widetilde{\mathbf{a}}_r) + (\mathbf{a}_t \otimes \mathbf{a}_r)^H \mathbf{z} \sim \mathcal{CN}((\mathbf{a}_t \otimes \mathbf{a}_r)^H (\widetilde{\mathbf{a}}_t' \otimes \widetilde{\mathbf{a}}_r), MN\sigma^2)$. By (4.36), we have*

$$T^c(\mathbf{y}) \sim \chi_2'^2(\lambda_0^c), \text{ under } H_0, \tag{4.42}$$

where $\lambda_0^c = \frac{2}{MN\sigma^2}|(\mathbf{a}_t \otimes \mathbf{a}_r)^H (\widetilde{\mathbf{a}}_t' \otimes \widetilde{\mathbf{a}}_r)|^2 = \frac{2}{MN\sigma^2}|g_t g_r|^2$.

Under H_1, we have $(\mathbf{a}_t \otimes \mathbf{a}_r)^H \mathbf{y} = bMN + (\mathbf{a}_t \otimes \mathbf{a}_r)^H (\widetilde{\mathbf{a}}_t' \otimes \widetilde{\mathbf{a}}_r) + (\mathbf{a}_t \otimes \mathbf{a}_r)^H \mathbf{z} \sim \mathcal{CN}(bMN + (\mathbf{a}_t \otimes \mathbf{a}_r)^H (\widetilde{\mathbf{a}}_t' \otimes \widetilde{\mathbf{a}}_r), MN\sigma^2)$. By (4.36), we have

$$T^c(\mathbf{y}) \sim \chi_2'^2(\lambda_1^c), \text{ under } H_1, \tag{4.43}$$

where $\lambda_1^c = \frac{2}{MN\sigma^2}|bMN + (\mathbf{a}_t \otimes \mathbf{a}_r)^H (\widetilde{\mathbf{a}}_t' \otimes \widetilde{\mathbf{a}}_r)|^2 = \frac{2MN|b|^2}{\sigma^2}\left|1+\frac{g_t^* g_r^*}{bMN}\right|^2$.

Because (4.37) depends on the unknown parameter g_t, the classic correlation detector is not a CFAR detector if the interference exists. When g_t is unknown, the theoretical performance shown in Lemma 1 assuming the knowledge of g_t can hardly be achieved.

Lemma 1 implies the following corollary.

Corollary 1 *In the interference-free case, the false alarm probability and probability of detection for the classic correlation solution in (4.36) are*

$$P_{FA}^c = e^{-\frac{1}{2}\gamma}, \tag{4.44}$$

$$P_D^c = Q_1\left(\sqrt{\lambda_1^c}, \sqrt{\gamma}\right). \tag{4.45}$$

where

$$\lambda_1^c = \frac{2MN|b|^2}{\sigma^2}. \tag{4.46}$$

Proof 7 *In the interference-free case, we have* $\widetilde{\mathbf{a}}_t' = \mathbf{0}$*, and hence* $g_t = 0$*. Substituting* $g_t = 0$ *into* (4.39) *and* (4.40)*, we have* $\lambda_0^c = 0$ *and* $\lambda_1^c = \frac{2MN|b|^2}{\sigma^2}$*. By* (4.37) *and* (4.38)*, we have the above corollary.*

Corollary 1 can also be derived by directly solving the performance of (4.36) when $\widetilde{\mathbf{a}}_t' = \mathbf{0}$ [37]. Corollary 1 shows that the classic correlation leads to a CFAR detector when there is no interference.

4.3.3 Proposed Subspace-based Detector

For achieving a better performance than classic correlation in the existence of interference, we solve the GLRT solution for Problem 1. Define

$$\boldsymbol{\theta}_0 \triangleq \widetilde{\mathbf{a}}_t', \quad \boldsymbol{\theta}_1 \triangleq [b, \boldsymbol{\theta}_0^T]^T \tag{4.47}$$

$$\mathbf{H}_0 \triangleq \mathbf{I}_M \otimes \widetilde{\mathbf{a}}_r, \quad \mathbf{H}_1 \triangleq [\mathbf{a}_t \otimes \mathbf{a}_r, \mathbf{H}_0], \tag{4.48}$$

where $\boldsymbol{\theta}_0$ ($\boldsymbol{\theta}_1$) is the unknown vector under H_0 (H_1) and $\mathbf{H}_0$ ($\mathbf{H}_1$) is the known matrix under H_0 (H_1). Then, we have $\mathbf{y} = \mathbf{H}_0\boldsymbol{\theta}_0 + \mathbf{z}$ under H_0 and $\mathbf{y} = \mathbf{H}_1\boldsymbol{\theta}_1 + \mathbf{z}$ under H_1. The likelihood function under H_0 is

$$p(\mathbf{y}; H_0) = \frac{\exp\left[-\frac{1}{\sigma^2}(\mathbf{y} - \mathbf{H}_0\boldsymbol{\theta}_0)^H(\mathbf{y} - \mathbf{H}_0\boldsymbol{\theta}_0)\right]}{(\pi\sigma^2)^{MN}}, \tag{4.49}$$

and the likelihood function under H_1 is

$$p(\mathbf{y}; H_1) = \frac{\exp\left[-\frac{1}{\sigma^2}(\mathbf{y} - \mathbf{H}_1\boldsymbol{\theta}_1)^H(\mathbf{y} - \mathbf{H}_1\boldsymbol{\theta}_1)\right]}{(\pi\sigma^2)^{MN}}. \tag{4.50}$$

The GLRT test statistics is

$$T(\mathbf{y}) = 2\ln\frac{\max_{\boldsymbol{\theta}_1} p(\mathbf{y}; H_1)}{\max_{\boldsymbol{\theta}_0} p(\mathbf{y}; H_0)}. \tag{4.51}$$

Via least square estimation, we have

$$\max_{\boldsymbol{\theta}_0} p(\mathbf{y}; H_0) = \frac{\exp[-\frac{1}{\sigma^2}\mathbf{y}^H\mathbf{P}_{\mathbf{H}_0}^{\perp}\mathbf{y}]}{(\pi\sigma^2)^{MN}}, \tag{4.52}$$

$$\max_{\boldsymbol{\theta}_1} p(\mathbf{y}; H_1) = \frac{\exp[-\frac{1}{\sigma^2}\mathbf{y}^H \mathbf{P}_{\mathbf{H}_1}^{\perp}\mathbf{y}]}{(\pi\sigma^2)^{MN}}, \tag{4.53}$$

where the projection matrices

$$\mathbf{P}_{\mathbf{H}_0}^{\perp} = \mathbf{I}_M \otimes \mathbf{P}_{\tilde{\mathbf{a}}_r}^{\perp}, \tag{4.54}$$

$$\mathbf{P}_{\mathbf{H}_1}^{\perp} = \mathbf{P}_{\mathbf{H}_0}^{\perp} - \frac{\mathbf{P}_{\mathbf{H}_0}^{\perp}(\mathbf{a}_t \otimes \mathbf{a}_r)(\mathbf{a}_t \otimes \mathbf{a}_r)^H \mathbf{P}_{\mathbf{H}_0}^{\perp H}}{(\mathbf{a}_t \otimes \mathbf{a}_r)^H \mathbf{P}_{\mathbf{H}_0}^{\perp H}(\mathbf{a}_t \otimes \mathbf{a}_r)}. \tag{4.55}$$

By (4.51), (4.52), (4.53), (4.54) and (4.55), the GLRT test statistics is

$$T(\mathbf{y}) = \frac{2}{\sigma^2}\frac{\left|\mathbf{y}^H\left(\mathbf{a}_t \otimes (\mathbf{P}_{\tilde{\mathbf{a}}_r}^{\perp}\mathbf{a}_r)\right)\right|^2}{\left|\mathbf{a}_t \otimes (\mathbf{P}_{\tilde{\mathbf{a}}_r}^{\perp}\mathbf{a}_r)\right|^2} \tag{4.56}$$

$$= \frac{2}{\sigma^2}\frac{1}{MN}\frac{|\mathbf{y}^H(\mathbf{a}_t \otimes \mathbf{a}_r) - g_r\frac{1}{N}\mathbf{y}^H(\mathbf{a}_t \otimes \widetilde{\mathbf{a}}_r)|^2}{1 - |g_r/N|^2}. \tag{4.57}$$

(4.56) indicates to project the target Rx steering vector $\mathbf{a}_r$ to the orthogonal subspace of the interfering Rx steering vector $\tilde{\mathbf{a}}_r$ via $\mathbf{P}_{\tilde{\mathbf{a}}_r}^{\perp}\mathbf{a}_r$. In other words, the GLRT test statistics of Problem 1 suggests subtracting the classic correlation result $\mathbf{y}^H(\mathbf{a}_t \otimes \mathbf{a}_r)$ by an estimated interference component $g_r\frac{1}{N}\mathbf{y}^H(\mathbf{a}_t \otimes \widetilde{\mathbf{a}}_r)$, as indicated in (4.57).

Lemma 2 *In Problem 1, the false alarm probability and probability of detection performance for the GLRT solution in* (4.56) *or* (4.57) *are*

$$P_{FA} = e^{-\frac{1}{2}\gamma}, \tag{4.58}$$

$$P_D = Q_1\left(\sqrt{\lambda}, \sqrt{\gamma}\right), \tag{4.59}$$

where

$$\lambda = \frac{2MN|b|^2}{\sigma^2}(1 - |g_r/N|^2), \tag{4.60}$$

γ *is the detection threshold.*

Proof 8 *Under* H_0*, we have* $(\mathbf{a}_t \otimes (\mathbf{P}^{\perp}_{\widetilde{\mathbf{a}}_r}\mathbf{a}_r))^H\mathbf{y} = (\mathbf{a}_t \otimes (\mathbf{P}^{\perp}_{\widetilde{\mathbf{a}}_r}\mathbf{a}_r))^H\mathbf{z}$*, where we have used the property that* $\left(\mathbf{a}_t \otimes (\mathbf{P}^{\perp}_{\widetilde{\mathbf{a}}_r}\mathbf{a}_r)\right)^H (\widetilde{\mathbf{a}}'_t \otimes \widetilde{\mathbf{a}}_r) = 0$*. As* $(\mathbf{a}_t \otimes (\mathbf{P}^{\perp}_{\widetilde{\mathbf{a}}_r}\mathbf{a}_r))^H\mathbf{z} \sim \mathcal{CN}(0, \sigma^2|\mathbf{a}_t \otimes (\mathbf{P}^{\perp}_{\widetilde{\mathbf{a}}_r}\mathbf{a}_r)|^2)$*, by* (4.56)*, we have*

$$T(\mathbf{y}) \sim \chi^2_2, \ \textit{under } H_0. \tag{4.61}$$

Under H_1*, we have* $(\mathbf{a}_t \otimes (\mathbf{P}^{\perp}_{\widetilde{\mathbf{a}}_r}\mathbf{a}_r))^H\mathbf{y} = (\mathbf{a}_t \otimes (\mathbf{P}^{\perp}_{\widetilde{\mathbf{a}}_r}\mathbf{a}_r))^H(b\mathbf{a}_t \otimes \mathbf{a}_r) + (\mathbf{a}_t \otimes (\mathbf{P}^{\perp}_{\widetilde{\mathbf{a}}_r}\mathbf{a}_r))^H\mathbf{z} \sim \mathcal{CN}((\mathbf{a}_t \otimes (\mathbf{P}^{\perp}_{\widetilde{\mathbf{a}}_r}\mathbf{a}_r))^H(b\mathbf{a}_t \otimes \mathbf{a}_r), \sigma^2|\mathbf{a}_t \otimes (\mathbf{P}^{\perp}_{\widetilde{\mathbf{a}}_r}\mathbf{a}_r)|^2)$*, by* (4.56)*, we have*

$$T(\mathbf{y}) \sim {\chi'}^2_2(\lambda), \ \textit{under } H_1, \tag{4.62}$$

where $\lambda = 2\frac{|(\mathbf{a}_t \otimes (\mathbf{P}^{\perp}_{\widetilde{\mathbf{a}}_r}\mathbf{a}_r))^H(b\mathbf{a}_t \otimes \mathbf{a}_r)|^2}{\sigma^2|\mathbf{a}_t \otimes (\mathbf{P}^{\perp}_{\widetilde{\mathbf{a}}_r}\mathbf{a}_r)|^2)} = \frac{2MN|b|^2}{\sigma^2}(1 - |g_r/N|^2)$*. By* $P_{FA} = F^c_{\chi^2_2}(\gamma)$ *and* $P_D = F^c_{{\chi'}^2_2(\lambda)}(\gamma)$*, we have* (4.58) *and* (4.59)*.*

As $Q_1\left(\sqrt{\lambda}, \sqrt{\gamma}\right)$ strictly increases with λ [62], P_D strictly increases with M. Further, as (4.58) does not depend on any unknown parameters, the GLRT detector is a CFAR detector in the existence of interference. Finally, as (4.60) does not depend on $\widetilde{\mathbf{a}}'_t$, P_D does not change with the change of the interference power, which is a benefit of the GLRT detector in (4.56) when the interference power is large. However, when the interference power is small, GLRT detector in (4.56) may perform worse than the classic correlation. For example, in the interference-free case, the performance loss of adopting the GLRT detector in (4.56) compared to adopting the classic correlation in (4.36) is represented in $\lambda = \lambda^c_1(1 - |g_r/N|^2)$ given by (4.46) and (4.60). Such performance loss can be reduced in general by increasing the size of receive array N, which will be illustrated in more detail in the next section.

4.3.4 Performance Validation and Evaluation

We define signal-to-noise ratio (SNR) and interference-to-signal ratio (ISR) as

$$\mathrm{SNR} = \frac{|b|^2}{\sigma^2}, \tag{4.63}$$

$$\mathrm{ISR} = \frac{\frac{1}{M}\widetilde{\mathbf{a}}'^H_t\widetilde{\mathbf{a}}_r}{|b|^2}. \tag{4.64}$$

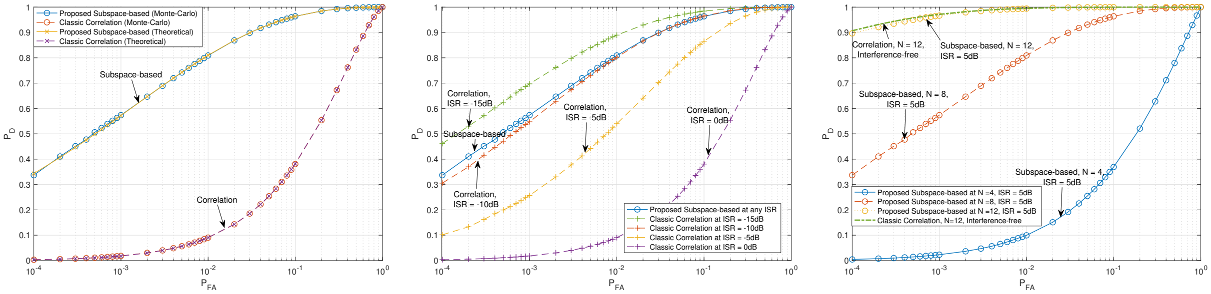

(a) Validation: $N = 8$ and ISR $= 0$dB.

(b) Evaluation: $N = 8$ and change ISR.

(c) Evaluation: change N.

Figure 4.4: Performance validation and evaluation of ROC curves under classical correlation and proposed GLRT when $M = 4$, target at 30°, interferer at 40°, and SNR $= -5$dB.

In the numerical performance validation and evaluation of this part, we consider the ideal case, where b, σ^2, $\widetilde{\mathbf{a}}_t'$, SNR and ISR are known.

The theoretical detection performance is validated and evaluated using receiver operating characteristics (ROC), which shows the probability of detection versus probability of false alarm, in Fig. 4.4. Fig. 4.4 (a) validates the theoretical performance of the classic correlator in (4.37) and (4.38) and the theoretical performance of the proposed subspace-based GLRT solution in (4.58) and (4.59) using Monte-Carlo simulation over 10^6 runs. Fig. 4.4 (b) shows that the theoretical ROC performance of the proposed subspace-based GLRT solution outperforms that of the classic correlator with known $\widetilde{\mathbf{a}}_t'$ when ISR is moderately large. Fig. 4.4 (c) shows that the ROC performance of the proposed subspace-based detector, in general, performs better with the increase of N, and is close to that of the performance of the GLRT detector under interference-free case when N is moderately large. This result inspires us to evaluate the performance scaling with respect to the Tx and Rx array sizes, which will be presented in the next section.

4.4 Massive MIMO Detection under Interference

In massive MIMO radar, an asymptotically perfect probability of detection can be achieved when the virtual array size goes to infinity [22]. The following lemma shows a similar result.

Lemma 3 *When the number of receive antennas* $N \to \infty$*, we have* $\lim_{N\to\infty} P_D \to 1$*. When the number of transmit antennas* $M \to \infty$*, we have* $\lim_{M\to\infty} P_D \to 1$.

Proof 9 *When the number of receive antennas* $N \to \infty$*, we have*

$$\lim_{N\to\infty} \frac{g_r}{N} = \lim_{N\to\infty} \frac{1}{N} \frac{1 - e^{-j2\pi N(f_{\phi_r} - \widetilde{f}_{\phi_r})}}{1 - e^{-j2\pi(f_{\phi_r} - \widetilde{f}_{\phi_r})}} \to 0.$$

Thus,

$$\lim_{N\to\infty} (1 - |g_r/N|^2) \to 1, \tag{4.65}$$

and hence $\lim_{N\to\infty} \lambda \to \infty$ *and* $\lim_{N\to\infty} P_D \to 1$*. Similarly,* $\lim_{M\to\infty} \lambda \to \infty$ *and* $\lim_{M\to\infty} P_D \to 1$.

(4.65) indicates that the performance of the subspace-based detector under interference shown in Lemma 2 is close to the performance of the GLRT solution without interference shown in Corollary 1. Lemma 3 also shows that when $N \to \infty$ or $M \to \infty$, the victim radar can achieve perfect target detection under interference. These results provide an insight for radar manufacturers that scaling up Tx and Rx array sizes can eliminate the impact of interference.

In realistic case, however, we cannot let $N \to \infty$ or $M \to \infty$. To guarantee slow-time code orthogonality for MIMO radar in (4.9), the number of transmit antennas should be smaller than the number of pulses in a CPI, i.e., $M \leq K$. Considering practical hardware implementation cost, M and N also cannot be very large. Motivated by these realistic constraints, we would like to find the region of N, such that when $N \geq N_{TH}$, we have a large enough detection probability P_D using the proposed subspace-based method. Thanks to the closed-form performance shown in Lemma 2, we have the following closed-form result.

Lemma 4 *For all*

$$N \geq N_{TH} \triangleq \frac{N_{TH}^c + \sqrt{(N_{TH}^c)^2 + (4/\delta)^2}}{2}, \tag{4.66}$$

we have the detection probability for the proposed subspace-based solution $P_D \geq P_{D,min}$ *for any fixed number of transmit antennas* M*, SNR* $\frac{|b|^2}{\sigma^2}$*, false alarm probability* $\bar{P}_{FA}$*, and any* $|1 - e^{-j2\pi(f_{\phi_r} - \widetilde{f}_{\phi_r})}| \geq \delta$*, where*

$$N_{TH}^c \triangleq \frac{1}{2|b|^2/\sigma^2} \frac{1}{M} \left(Q_1^{-1} \left(P_{D,min}, \sqrt{-2 \ln \bar{P}_{FA}} \right) \right)^2 \tag{4.67}$$

is the number of Rx array elements for achieving $P_{D,min}$ *under the interference-free case.*

Proof 10 (4.67) *can be easily obtained by solving* (4.44) *and* (4.45)*.* $P_D \geq P_{D,min}$ *is equivalent to*

$$\sqrt{\lambda} \geq Q_1^{-1} \left(P_{D,min}, \sqrt{-2 \ln \bar{P}_{FA}} \right), \tag{4.68}$$

which is further equivalent to

$$N(1 - |g_r/N|^2) \geq N_{TH}^c, \tag{4.69}$$

While for any $|1 - e^{-j2\pi(f_{\phi_r} - \widetilde{f}_{\phi_r})}| \geq \delta$*, we have*

$$|g_r| = \frac{|1 - e^{-j2\pi N(f_{\phi_r} - \widetilde{f}_{\phi_r})}|}{|1 - e^{-j2\pi(f_{\phi_r} - \widetilde{f}_{\phi_r})}|} \leq \frac{2}{\delta}. \tag{4.70}$$

Combining (4.69) *and* (4.70)*, we have* (4.66)*.*

We formally define the regime $N \geq N_{TH}$ as the *massive MIMO regime* for any M, $\frac{|b|^2}{\sigma^2}$, $\bar{P}_{FA}$, $P_{D,min}$, and δ. Lemma 4 shows that as long as the victim radar operates at the massive MIMO regime, the target detection performance is guaranteed, regardless of the interference power using the proposed subspace-based detector. (4.66) and (4.67) suggest that the larger number of Tx array size M or the higher SNR $\frac{|b|^2}{\sigma^2}$, the faster the victim radar entering into the massive MIMO regime.

In Fig. 4.5, we evaluate the theoretical detection performance when we change M and N. If we choose $P_{D,min} = 0.95$ and the setup in Fig. 4.5, by (4.66) and (4.67), we obtain the theoretical bounds for entering into the massive MIMO regime as follows. When $M = 4$, we have $\lceil N_{TH} \rceil = 14$ and $\lceil N_{TH}^c \rceil = 15$; when $M = 8$, we have $\lceil N_{TH} \rceil = 7$ and $\lceil N_{TH}^c \rceil = 9$. Fig. 4.5 shows that the massive MIMO bound N_{TH}^c is approximately tight in the considered setup, and the performance of the proposed subspace-based solution under any interference power is close that in the interference-free case when N is moderately large. In addition, Fig. 4.5 validates that larger M leads to larger P_D. In addition, the larger M, the faster the victim radar enters into the massive MIMO regime.

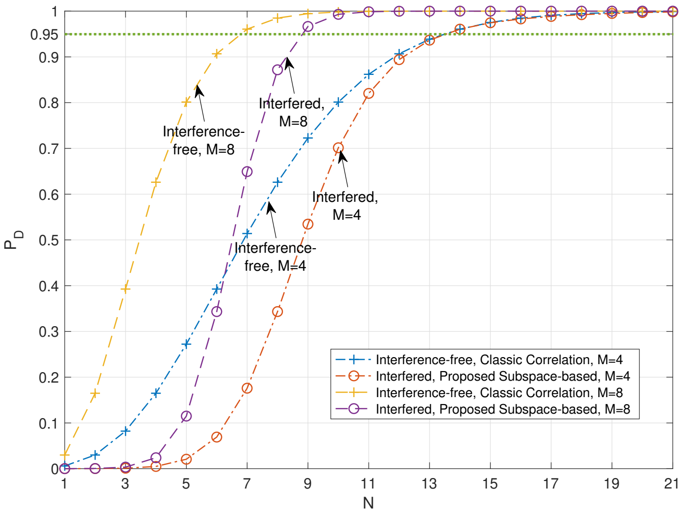

Figure 4.5: P_D VS. N under different M when $P_{FA} = 10^{-4}$, target at 30°, interferer at 40°, and SNR $= -5$dB.

4.5 Simulator Performance Evaluation

In this section, we simulate the detection performance of the detectors under a more realistic scenario that considers antenna beampattern, imperfect orthogonality of the MIMO code, multiple targets, and unknown noise power. This realistic scenario can be simulated based on MATLAB Phased Array System Toolbox, which consists of MIMO-FMCW waveform generation, antenna array modeling, target/interference channel propagation, and FMCW signal processing chain (e.g., dechirping, ADC sampling, low-pass filtering, MIMO radar encoding and decoding, etc.). Notice that it's hard to obtain noise power information from MATLAB Phased Array System Toolbox. Thus, it's hard to obtain detection statistics of $T^c(\mathbf{y})$ in (4.36) and $T(\mathbf{y})$ in (4.57). In the following, we evaluate the corresponding detection map of the classic correlator $|\mathbf{y}^H(\mathbf{a}_t \otimes \mathbf{a}_r)|^2$ and the detection map of the proposed solution $\frac{|\mathbf{y}^H(\mathbf{a}_t\otimes\mathbf{a}_r)-\frac{g_r}{N}\mathbf{y}^H(\mathbf{a}_t\otimes\widetilde{\mathbf{a}}_r)|^2}{1-|g_r/N|^2}$ which do not require the knowledge of the noise power.

To visualize the strength of the proposed subspace-based solution and massive MIMO under the proposed subspace-based solution, we evaluate the detection map of the classic correlator $|\mathbf{y}^H(\mathbf{a}_t \otimes \mathbf{a}_r)|^2$ and the detection map of the proposed solution $\frac{|\mathbf{y}^H(\mathbf{a}_t\otimes\mathbf{a}_r)-\frac{g_r}{N}\mathbf{y}^H(\mathbf{a}_t\otimes\widetilde{\mathbf{a}}_r)|^2}{1-|g_r/N|^2}$. We adopt the basic simulation setup in Table 4.1. We simulate 2 targets and 1 interferer case as shown in Table 4.2, and show the simulation results in Fig. 4.6. Fig. 4.6 (a)-(c) show the detection map performance using the classic correlator $|\mathbf{y}^H(\mathbf{a}_t \otimes \mathbf{a}_r)|^2$ and Fig. 4.6 (d)-(f) show the detection map performance using the proposed subspace-based solution $\frac{|\mathbf{y}^H(\mathbf{a}_t\otimes\mathbf{a}_r)-\frac{g_r}{N}\mathbf{y}^H(\mathbf{a}_t\otimes\widetilde{\mathbf{a}}_r)|^2}{1-|g_r/N|^2}$. Fig. 4.6 (a)-(c) show that the classic correlation leads to high noise-floor elevation and false peaks on the range-angle heatmap, even when the Rx array size is large, e.g., $N = 32$. In contrast, Fig. 4.6 (d)-(f) show that when the Rx array size is not large enough, e.g., $N = 8$, we can observe the suppressed interference, whose power is smaller than the power of all the targets; when the Rx array size is large, e.g., $N = 32$, the interference can nearly be fully suppressed. The performance difference in Fig. 4.6 (c) and (f) indicate that the proposed subspace-based solution is easier to enter into the massive MIMO regime compared to the classic correlation. Fig. 4.6 also shows that the proposed subspace-based detector works well in the multi-target scenario.

We finally simulate the ROC performance of the classic correlator and the proposed subspace-based detector using MATLAB Phased Array System Toolbox under the basic setup in Table 4.1 with 1 target and 1 interferer setup in Table 4.3. Notice that without knowing the exact noise power, we can still simulate the detection map of the classic correlator

$|\mathbf{y}^H(\mathbf{a}_t \otimes \mathbf{a}_r)|^2$ and the detection map of the proposed solution $\frac{|\mathbf{y}^H(\mathbf{a}_t \otimes \mathbf{a}_r) - \frac{g_r}{N}\mathbf{y}^H(\mathbf{a}_t \otimes \widetilde{\mathbf{a}}_r)|^2}{1-|g_r/N|^2}$, under null hypothesis H_0 and alternative hypothesis H_1. Via obtaining 1000 sets of the detection results under the two hypotheses with $\mathbf{y}$ generated from MATLAB Phased Array System Toolbox, we can obtain the ROC curves shown in Fig. 4.7. From Fig. 4.7, we can see that the proposed subspace-based detector still outperforms the classic correlator in terms of the ROC performance with the consideration of the antenna beampattern, imperfect orthogonality of the MIMO code, and unknown noise power.

4.6 Summary

In this chapter, we considered spatial-time domain incoherent FMCW radar interference mitigation to improve spatial detection performance. One of our main contributions is that we are the first to formulate the MIMO-FMCW radar interference signal model and a spatial MIMO detection problem that accounts for the interference structure. We proposed a subspace-based detector in the existence of mutual MIMO-FMCW radar interference. We showed that the proposed subspace-based detector holds the desired property of CFAR and performs better than the classic correlation-based detector when the interference power is moderately large.

Our another main contribution is evaluating the impact of antenna array size to the interference mitigation, which involves the analysis of the next-generation massive MIMO radar. Specifically, we showed that the detection performance of the proposed subspace-based detector strictly increases with the size of the Tx array and in general improves with the size of the Rx array. When the Tx or Rx array size goes to infinity, we showed that the victim radar can achieve perfect detection performance under interference. We defined and analyzed the effect of massive MIMO for interference suppression. We showed that when the size of the Rx array is moderately large, the proposed subspace-based solution under interference achieves approximately the same performance under the interference-free case. We also derived a closed-form massive MIMO regime and showed that the larger size of the Tx array leads to a larger detection probability and faster convergence to the massive MIMO regime. We validated and evaluated our result using Monte-Carlo simulations and MATLAB Phased Array System Toolbox.

Table 4.1: Basic simulation setup in MATLAB Phased Array System Toolbox.

RF wavelength	3.9 mm
TX power (RX noise figure)	5 dBm (4.5 dB)
TX (RX) antenna gain	36(42) dB
TX (RX) antenna element type	Backbaffled isotropic
TX (RX) array structure	Uniform linear array
MIMO slow-time code type	Chu sequence
Chirp bandwidth	460 MHz
IF bandwidth (ADC complex sample rate)	15 MHz (16.7 MHz)
Number of chirps in a CPI	256
Range (Velocity) DFT size	512 (256)
Angle processing size (zero-padded length)	128
Target model	Non-fluctuating
Target (interference) channel	Free-space two-way (one-way) channel
Victim radar's chirp slope	15 MHz/us
Victim radar's chirp sweep duration	30.7 us
Victim radar's inter-chirp idle duration	7 us
Victim radar's TX (RX) element spacing	15.6 mm (1.95 mm)
Victim radar's TX antenna number	4
Interferer's TX element spacing	3.9 mm
Interferer's TX antenna number	8

Table 4.2: Targets and interferer setup for Fig. 4.6.

Targets' RCS	20dBsm
Target 1's distance, velocity, angle	50 m, 1.6 m/s, $-26°$
Target 2's distance, velocity, angle	10 m, -2.4 m/s, 40°
Interferer's distance, velocity, angle	14.7 m, 7.2 m/s, 18°
Interferer's chirp slope	19.7 MHz/us
Interferer's chirp sweep duration	23.4 us
Interferer's inter-chirp idle duration	7.4 us
Initial time offset between interferer and victim radar	5.7 us

Table 4.3: Target and interferer setup for Fig. 4.7.

Target's RCS	0dBsm
Target's distance, velocity, angle	50 m, 1.6 m/s, $-26°$
Interferer's distance, velocity, angle	2.5 m, -20.3 m/s, 18°
Interferer's chirp slope	16.3 MHz/us
Interferer's chirp sweep duration	28.3 us
Interferer's inter-chirp idle duration	7.9 us
Initial time offset between interferer and victim radar	8.8 us

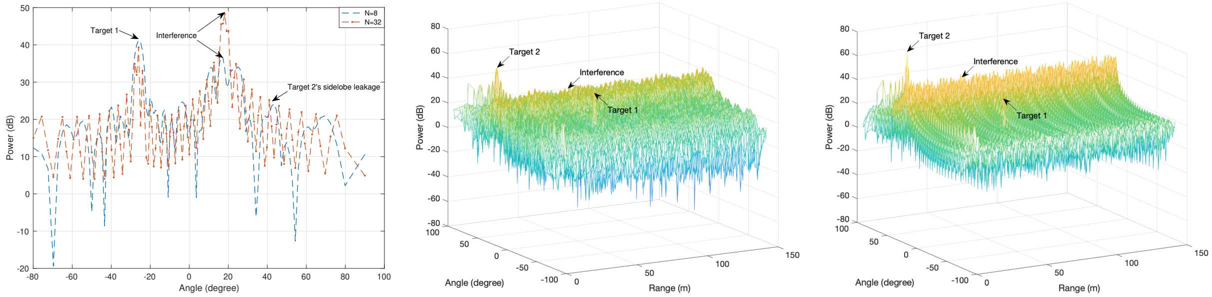

(a) Angle profile at target 1's range-Doppler bin using classic correlator $|\mathbf{y}^H(\mathbf{a}_t \otimes \mathbf{a}_r)|^2$.

(b) Range-angle heatmap at target 1's Doppler bin and $N = 8$ using classic correlator $|\mathbf{y}^H(\mathbf{a}_t \otimes \mathbf{a}_r)|^2$.

(c) Range-angle heatmap at target 1's Doppler bin and $N = 32$ using classic correlator $|\mathbf{y}^H(\mathbf{a}_t \otimes \mathbf{a}_r)|^2$.

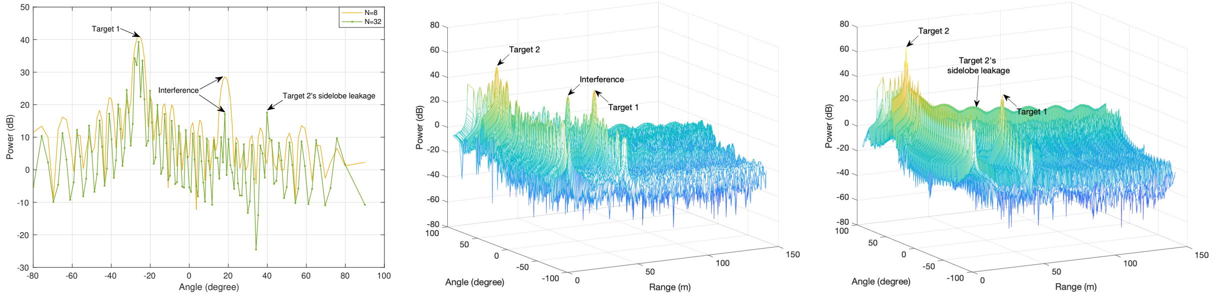

(d) Angle profile at target 1's range-Doppler bin using proposed subspace-based solution $\frac{|\mathbf{y}^H(\mathbf{a}_t \otimes \mathbf{a}_r) - \frac{g_r}{N}\mathbf{y}^H(\mathbf{a}_t \otimes \tilde{\mathbf{a}}_r)|^2}{1 - |g_r/N|^2}$.

(e) Range-angle heatmap at target 1's Doppler bin and $N = 8$ using proposed subspace-based solution $\frac{|\mathbf{y}^H(\mathbf{a}_t \otimes \mathbf{a}_r) - \frac{g_r}{N}\mathbf{y}^H(\mathbf{a}_t \otimes \tilde{\mathbf{a}}_r)|^2}{1 - |g_r/N|^2}$.

(f) Range-angle heatmap at target 1's Doppler bin and $N = 32$ using proposed subspace-based solution $\frac{|\mathbf{y}^H(\mathbf{a}_t \otimes \mathbf{a}_r) - \frac{g_r}{N}\mathbf{y}^H(\mathbf{a}_t \otimes \tilde{\mathbf{a}}_r)|^2}{1 - |g_r/N|^2}$.

Figure 4.6: Detection map performance using MATLAB Phased Array System Toolbox under the basic setup in Table 4.1 with 2 targets and 1 interferer setup in Table 4.2.

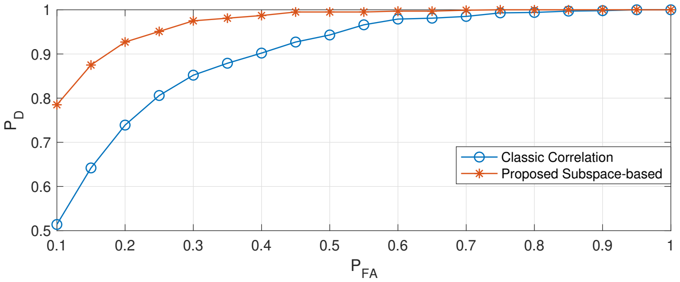

Figure 4.7: Angle domain detection ROC curves at target range-Doppler bin over 1000 Monte-Carlo runs using MATLAB Phased Array System Toolbox under the basic setup in Table 4.1 with 1 target and 1 interferer setup in Table 4.3.

Chapter 5

CONCLUSION

In this thesis, we considered mutual FMCW automotive radar coherent and incoherent interference issues and the related interference mitigation methods. The following conclusions are the main takeaway for automotive radar manufacturers and standardization. Under coherent mutual radar interference, the main issue is the difficulty to classify interference from targets, and we can use randomization radar MACs. e.g., slow-time phase coding and frequency hopping, to help radars finish this classification and reduce false alarm. These randomization radar MACs do not require any synchronization and mutual-radar coordination and are thus easy to be implemented on current non-cooperative radar networks. Under incoherent mutual radar interference, the main issue is the noise floor elevation caused by the interference. We need advanced target recovery or interference suppression methods to deal with incoherent interference. We can use the time-frequency mode reconstruction proposed in this work to directly recover targets and improve performance in the range-velocity domain. This time-frequency mode reconstruction method works under strong incoherent interference and can be implemented on SISO-FMCW radars and MIMO-FMCW radars. For MIMO-FMCW radar, we can also use a subspace-based interference detector to project interference in the angle domain to cancel interference. And we can use massive MIMO to project a large part of the target signal to orthogonal interference subspace in the angle domain. We derived a massive MIMO bound, which provides a bound of the required number of Rx antennas for achieving a guaranteed detection performance with a given number of Tx antennas. This massive MIMO bound can be a practical calculation of the required number of Tx and Rx antennas for radar manufacturers to refer to.

The original contributions of this thesis include 1) introduced 2 cross-layer performance metrics to radar networks, multiple access capacity and probability of target misdetection, analyzed the two metrics under coherent interference and 4 radar MACs, and showed that detect-and-classify schemes, such as slow-time phase coding and frequency hopping, can achieve very large multiple access capacity without requiring mutual-radar synchronization and coordination; 2) proposed a fast-time-frequency mode reconstruction method to recover target under strong incoherent interference; 3) provided the first model of MIMO-FMCW interference, formulated the spatial MIMO interference cancellation problem as a hypothesis testing problem, and obtained a subspace-based MIMO detector which is a CFAR detector under interference; 4) analyzed the interference mitigation performance under massive MIMO, and derived a massive MIMO bound, which can be realistic reference for radar manufacturers in selecting number of Tx and Rx antennas for MIMO radars.

For future work, we can consider the combination of the schemes proposed in this thesis. We already have used slow-time phase coding in the second chapter on the MIMO-FMCW radars in the fourth chapter. As a future extension, we can see how fast-time-frequency mode reconstruction in the third chapter impacts the MIMO-FMCW radar detection. A joint scheme that improves range-Doppler detection and spatial detection under interference using fast-time domain scheme (e.g., the proposed fast-time-frequency mode reconstruction), slow-time domain scheme (e.g., the radar MACs in this thesis), and spatial domain scheme (e.g., the proposed subspace-based MIMO radar detector) will be promising. For example, formulating a space-time adaptive processing (STAP) [46] problem for MIMO-FMCW mutual interference mitigation can help both Doppler detection and spatial detection. Furthermore, there is a trend in using automotive radar for object recognition using the deep learning method [26]. Investigating how radar interference impacts radar object recognition and how deep learning can help improve object detection under interference will be a promising future direction.

BIBLIOGRAPHY

[1] Nabeel Akhtar, Sinem Coleri Ergen, and Oznur Ozkasap. Vehicle mobility and communication channel models for realistic and efficient highway VANET simulation. *IEEE Transactions on Vehicular Technology*, 64(1):248–262, 2015.

[2] Akram Al-Hourani, Robin J. Evans, Sithamparanathan Kandeepan, Bill Moran, and Hamid Eltom. Stochastic geometry methods for modeling automotive radar interference. *IEEE Transactions on Intelligent Transportation Systems*, 19(2):333–344, 2018.

[3] Stephen Alland, Wayne Stark, Murtaza Ali, and Manju Hegde. Interference in automotive radar systems: Characteristics, mitigation techniques, and current and future research. *IEEE Signal Processing Magazine*, 36(5):45–59, 2019.

[4] F. Auger and P. Flandrin. Improving the readability of time-frequency and time-scale representations by the reassignment method. *IEEE Transactions on Signal Processing*, 43(5):1068–1089, 1995.

[5] Francois Auger, Patrick Flandrin, Yu-Ting Lin, Stephen McLaughlin, Sylvain Meignen, Thomas Oberlin, and Hau-Tieng Wu. Time-frequency reassignment and synchrosqueezing: An overview. *IEEE Signal Processing Magazine*, 30(6):32–41, 2013.

[6] Canan Aydogdu, Musa Furkan Keskin, Gisela K. Carvajal, Olof Eriksson, Hans Hellsten, Hans Herbertsson, Emil Nilsson, Mats Rydstrom, Karl Vanas, and Henk Wymeersch. Radar interference mitigation for automated driving: Exploring proactive strategies. *IEEE Signal Processing Magazine*, 37(4):72–84, 2020.

[7] Canan Aydogdu, Musa Furkan Keskin, Nil Garcia, Henk Wymeersch, and Daniel W. Bliss. Radchat: Spectrum sharing for automotive radar interference mitigation. *IEEE Transactions on Intelligent Transportation Systems*, 22(1):416–429, 2021.

[8] Michael Barjenbruch, Dominik Kellner, Klaus Dietmayer, Jens Klappstein, and Juergen Dickmann. A method for interference cancellation in automotive radar. In *2015 IEEE MTT-S International Conference on Microwaves for Intelligent Mobility (ICMIM)*, pages 1–4, 2015.

[9] Jonathan Bechter, Amarilda Demirlika, Philipp Hügler, Fabian Roos, and Christian Waldschmidt. Blind adaptive beamforming for automotive radar interference suppression. In *2018 19th International Radar Symposium (IRS)*, pages 1–10, 2018.

[10] Jonathan Bechter, Muhammad Rameez, and Christian Waldschmidt. Analytical and experimental investigations on mitigation of interference in a DBF MIMO radar. *IEEE Transactions on Microwave Theory and Techniques*, 65(5):1727–1734, 2017.

[11] Jonathan Bechter, Fabian Roos, Mahfuzur Rahman, and Christian Waldschmidt. Automotive radar interference mitigation using a sparse sampling approach. In *2017 European Radar Conference (EURAD)*, pages 90–93, 2017.

[12] Igal Bilik, Oren Longman, Shahar Villeval, and Joseph Tabrikian. The rise of radar for autonomous vehicles: Signal processing solutions and future research directions. *IEEE Signal Processing Magazine*, 36(5):20–31, 2019.

[13] Arindam Bose, Bo Tang, Mojtaba Soltanalian, and Jian Li. Mutual interference mitigation for multiple connected automotive radar systems. *IEEE Transactions on Vehicular Technology*, 70(10):11062–11066, 2021.

[14] Graham M. Brooker. Mutual interference of millimeter-wave radar systems. *IEEE Transactions on Electromagnetic Compatibility*, 49(1):170–181, 2007.

[15] R.A. Carmona, W.L. Hwang, and B. Torresani. Characterization of signals by the ridges of their wavelet transforms. *IEEE Transactions on Signal Processing*, 45(10):2586–2590, 1997.

[16] Hossein Chahrour, Sreeraman Rajan, Richard Dansereau, and Bhashyam Balaji. Hybrid beamforming for interference mitigation in MIMO radar. In *2018 IEEE Radar Conference (RadarConf18)*, pages 1005–1009, 2018.

[17] Shengyi Chen, Wangyi Shangguan, Jalal Taghia, Uwe Kühnau, and Rainer Martin. Automotive radar interference mitigation based on a generative adversarial network. In *2020 IEEE Asia-Pacific Microwave Conference (APMC)*, pages 728–730, 2020.

[18] Aitor Correas-Serrano and Maria A. Gonzalez-Huici. Sparse reconstruction of chirplets for automotive FMCW radar interference mitigation. In *2019 IEEE MTT-S International Conference on Microwaves for Intelligent Mobility (ICMIM)*, pages 1–4, 2019.

[19] Vivek Dham. Programming chirp parameters in TI radar devices. *Texas Instruments*, 2020.

[20] Anand Dubey, Jonas Fuchs, Venkat Madhavan, Maximilian Lübke, Robert Weigel, and Fabian Lurz. Region based single-stage interference mitigation and target detection. In *2020 IEEE Radar Conference (RadarConf20)*, pages 1–5, 2020.

[21] Clément Fischer, Markus Goppelt, H-L. Blöcher, and Jürgen Dickmann. Minimizing interference in automotive radar using digital beamforming. *Advances in Radio Science*, 9:45–48, 2011.

[22] Stefano Fortunati, Luca Sanguinetti, Fulvio Gini, Maria Sabrina Greco, and Braham Himed. Massive MIMO radar for target detection. *IEEE Transactions on Signal Processing*, 68:859–871, 2020.

[23] Jonas Fuchs, Anand Dubey, Maximilian Lübke, Robert Weigel, and Fabian Lurz. Automotive radar interference mitigation using a convolutional autoencoder. In *2020 IEEE International Radar Conference (RADAR)*, pages 315–320, 2020.

[24] Kohei Fujiwara, Hidehiko Yamaoka, Tatsunori Onzuka, Shingo Ozaki, Yoneo Akita, and Yoshikazu Fujinaka. A simple-structure FMCW radar test system using pll-gunn oscillator and fundamental mixer in 79 GHz band. In *2018 International Conference on Radar (RADAR)*, pages 1–6, 2018.

[25] Xiangyu Gao, Guanbin Xing, Sumit Roy, and Hui Liu. RAMP-CNN: A novel neural network for enhanced automotive radar object recognition. *IEEE Sensors Journal*, 21(4):5119–5132, 2021.

[26] Xiangyu Gao, Guanbin Xing, Sumit Roy, and Hui Liu. Ramp-cnn: A novel neural network for enhanced automotive radar object recognition. *IEEE Sensors Journal*, 21(4):5119–5132, 2021.

[27] Davide Guermandi, Qixian Shi, Andy Dewilde, Veerle Derudder, Ubaid Ahmad, Annachiara Spagnolo, Ilja Ocket, André Bourdoux, Piet Wambacq, Jan Craninckx, and Wim Van Thillo. A 79-GHz 2 × 2 MIMO PMCW radar SoC in 28-nm CMOS. *IEEE Journal of Solid-State Circuits*, 52(10):2613–2626, 2017.

[28] Gor Hakobyan and Bin Yang. High-performance automotive radar: A review of signal processing algorithms and modulation schemes. *IEEE Signal Processing Magazine*, 36(5):32–44, 2019.

[29] Chenming Jiang, Tianyi Chen, and Bin Yang. Adversarial interference mitigation for automotive radar. In *2021 IEEE Radar Conference (RadarConf21)*, pages 1–6, 2021.

[30] Feng Jin and Siyang Cao. Automotive radar interference mitigation using adaptive noise canceller. *IEEE Transactions on Vehicular Technology*, 68(4):3747–3754, 2019.

[31] Sian Jin, Jun Hyeon Park, and Sumit Roy. Slow-time waveform randomization performance under incoherent FMCW radar interference. In *2021 IEEE 94th Vehicular Technology Conference (VTC2021-Fall)*, pages 1–7, 2021.

[32] Sian Jin and Sumit Roy. Cross-layer interference modeling and performance analysis in FMCW radar multiple access network. In *2020 IEEE 92nd Vehicular Technology Conference (VTC2020-Fall)*, pages 1–6, 2020.

[33] Sian Jin and Sumit Roy. FMCW radar network: Multiple access and interference mitigation. *IEEE Journal of Selected Topics in Signal Processing*, 15(4):968–979, 2021.

[34] Sian Jin, Pu Wang, Petros Boufounos, Phil Orlik, and Sumit Roy. Automotive radar interference mitigation with fast-time-frequency mode retrieval. In *2022 IEEE Radar Conference (accepted)*, 2022.

[35] Sian Jin, Pu Wang, Petros Boufounos, Phil Orlik, and Sumit Roy. Mutual interference mitigation for MIMO-FMCW automotive radar. In *IEEE SAM (to be submitted)*, 2022.

[36] Sian Jin, Pu Wang, Petros Boufounos, Phil Orlik, and Sumit Roy. Mutual interference mitigation for MIMO-FMCW automotive radar. *IEEE Transactions on Vehicular Technology (to be submitted)*, 2022.

[37] Steven M Kay. *Fundamentals of statistical signal processing: detection theory*. Prentice Hall PTR, 1998.

[38] Joud Khoury, Ram Ramanathan, Dan McCloskey, Russell Smith, and Timothy Campbell. Radarmac: Mitigating radar interference in self-driving cars. In *2016 13th Annual IEEE International Conference on Sensing, Communication, and Networking (SECON)*, pages 1–9, 2016.

[39] Geonu Kim, Jiwoo Mun, and Jungwoo Lee. A peer-to-peer interference analysis for automotive chirp sequence radars. *IEEE Transactions on Vehicular Technology*, 67(9):8110–8117, 2018.

[40] James F. Kurose and Keith W. Ross. *Computer Networking: A Top-Down Approach*. Pearson, 7 edition, 2016.

[41] Seongwook Lee, Jung-Yong Lee, and Seong-Cheol Kim. Mutual interference suppression using wavelet denoising in automotive FMCW radar systems. *IEEE Transactions on Intelligent Transportation Systems*, 22(2):887–897, 2021.

[42] Tang-Nian Luo, Chi-Hung Evelyn Wu, and Yi-Jan Emery Chen. A 77-GHz CMOS automotive radar transceiver with anti-interference function. *IEEE Transactions on Circuits and Systems I: Regular Papers*, 60(12):3247–3255, 2013.

[43] Mathworks. Increasing angular resolution with virtual arrays. 2022.

[44] Khurram Usman Mazher, Robert W. Heath, Kapil Gulati, and Junyi Li. Automotive radar interference characterization and reduction by partial coordination. In *2020 IEEE Radar Conference (RadarConf20)*, pages 1–6, 2020.

[45] Khurram Usman Mazher, Robert W. Heath, Kapil Gulati, and Junyi Li. Automotive radar interference characterization and reduction by partial coordination. In *2020 IEEE Radar Conference (RadarConf20)*, pages 1–6, 2020.

[46] W.L. Melvin. A STAP overview. *IEEE Aerospace and Electronic Systems Magazine*, 19(1):19–35, 2004.

[47] Sharef Neemat, Oleg Krasnov, and Alexander Yarovoy. An interference mitigation technique for FMCW radar using beat-frequencies interpolation in the stft domain. *IEEE Transactions on Microwave Theory and Techniques*, 67(3):1207–1220, 2019.

[48] T. Oberlin, S. Meignen, and V. Perrier. The fourier-based synchrosqueezing transform. In *2014 IEEE International Conference on Acoustics, Speech and Signal Processing (ICASSP)*, pages 315–319, 2014.

[49] Sujeet Milind Patole, Murat Torlak, Dan Wang, and Murtaza Ali. Automotive radars: A review of signal processing techniques. *IEEE Signal Processing Magazine*, 34(2):22–35, 2017.

[50] Karthik Ramasubramanian. mmWave radar for automotive and industrial applications. *Texas Instruments*, 2017.

[51] Karthik Ramasubramanian and Brian Ginsburg. AWR1243 sensor: Highly integrated. 76–81GHz radar front-end for emerging ADAS applications. *Texas Instruments Technical Report*, 2017.

[52] Muhammad Rameez, Mattias Dahl, and Mats I. Pettersson. Adaptive digital beamforming for interference suppression in automotive FMCW radars. In *2018 IEEE Radar Conference (RadarConf18)*, pages 0252–0256, 2018.

[53] Muhammad Rameez, Mattias Dahl, and Mats I. Pettersson. Experimental evaluation of adaptive beamforming for automotive radar interference suppression. In *2020 IEEE Radio and Wireless Symposium (RWS)*, pages 183–186, 2020.

[54] Sandeep Rao. Introduction to mmWave sensing: FMCW radars. *Texas Instruments (TI) mmWave Training Series*, 2017.

[55] Sandeep Rao and Anil Varghese Mani. Interference characterization in FMCW radars. In *2020 IEEE Radar Conference (RadarConf20)*, pages 1–6, 2020.

[56] Mark A. Richards. *Fundamentals of radar signal processing.* McGraw-Hill, second edition, 2014.

[57] Nicolae-Cătălin Ristea, Andrei Anghel, and Radu Tudor Ionescu. Fully convolutional neural networks for automotive radar interference mitigation. In *2020 IEEE 92nd Vehicular Technology Conference (VTC2020-Fall)*, pages 1–5, 2020.

[58] Johanna Rock, Wolfgang Roth, Mate Toth, Paul Meissner, and Franz Pernkopf. Resource-efficient deep neural networks for automotive radar interference mitigation. *IEEE Journal of Selected Topics in Signal Processing*, 15(4):927–940, 2021.

[59] Fabian Roos, Jonathan Bechter, Christina Knill, Benedikt Schweizer, and Christian Waldschmidt. Radar sensors for autonomous driving: Modulation schemes and interference mitigation. *IEEE Microwave Magazine*, 20(9):58–72, 2019.

[60] Peter J Rousseeuw and Christophe Croux. Alternatives to the median absolute deviation. *Journal of the American Statistical association*, 88(424):1273–1283, 1993.

[61] Shunqiao Sun, Athina P. Petropulu, and H. Vincent Poor. MIMO radar for advanced driver-assistance systems and autonomous driving: Advantages and challenges. *IEEE Signal Processing Magazine*, 37(4):98–117, 2020.

[62] Yin Sun, Árpád Baricz, and Shidong Zhou. On the monotonicity, log-concavity, and tight bounds of the generalized marcum and nuttall q-functions. *IEEE Transactions on Information Theory*, 56(3):1166–1186, 2010.

[63] Bo Tang, Wenjie Huang, and Jian Li. Slow-time coding for mutual interference mitigation. In *IEEE ICASSP*, pages 6508–6512, 2018.

[64] Gaurav Thakur, Eugene Brevdo, Neven S. Fuckar, and Hau-Tieng Wu. The synchrosqueezing algorithm for time-varying spectral analysis: Robustness properties and new paleoclimate applications. *Signal Processing*, 93(5):1079–1094, 2013.

[65] Gaurav Thakur and Hau-Tieng Wu. Synchrosqueezing based recovery of instantaneous frequency from nonuniform samples. *SIAM J. Math. Anal.*, 43(5):2078–2095, 2011.

[66] Mate Toth, Paul Meissner, Alexander Melzer, and Klaus Witrisal. Performance comparison of mutual automotive radar interference mitigation algorithms. In *2019 IEEE Radar Conference (RadarConf)*, pages 1–6, 2019.

[67] Mate Toth, Paul Meissner, Alexander Melzer, and Klaus Witrisal. Slow-time mitigation of mutual interference in chirp sequence radar. In *2020 IEEE MTT-S International Conference on Microwaves for Intelligent Mobility (ICMIM)*, pages 1–4, 2020.

[68] Mate Toth, Johanna Rock, Paul Meissner, Alexander Melzer, and Klaus Witrisal. Analysis of automotive radar interference mitigation for real-world environments. In *2020 17th European Radar Conference (EuRAD)*, pages 176–179, 2021.

[69] Faruk Uysal and Sasanka Sanka. Mitigation of automotive radar interference. In *2018 IEEE Radar Conference (RadarConf18)*, pages 0405–0410, 2018.

[70] Matthias Wagner, Fisnik Sulejmani, Alexander Melzer, Paul Meissner, and Mario Huemer. Threshold-free interference cancellation method for automotive FMCW radar systems. In *2018 IEEE International Symposium on Circuits and Systems (ISCAS)*, pages 1–4, 2018.

[71] Jianping Wang. CFAR-based interference mitigation for FMCW automotive radar systems. *arXiv preprint arXiv:2101.01257*, 2021.

[72] Jianping Wang, Runlong Li, Yuan He, and Yang Yang. Prior-guided deep interference mitigation for FMCW radars. *arXiv preprint arXiv:2108.13023*, 2021.

[73] Pu Wang, Petros Boufounos, Hassan Mansour, and Philip V. Orlik. Slow-time MIMO-FMCW automotive radar detection with imperfect waveform separation. In *ICASSP 2020 - 2020 IEEE International Conference on Acoustics, Speech and Signal Processing (ICASSP)*, pages 8634–8638, 2020.

[74] Pu Wang, David Millar, Kieran Parsons, Rui Ma, and Phillip V. Orlik. Range accuracy analysis for FMCW systems with source nonlinearity. In *2019 IEEE MTT-S International Conference on Microwaves for Intelligent Mobility (ICMIM)*, pages 1–5, 2019.

[75] Zigang Yang and Anil Mani. Interference mitigation for AWR/IWR devices. *Texas Instruments*, 2020.

VITA

Journal Papers:

1. S. Jin, P. Wang, P. Boufounos, P. Orlik, and S. Roy. “Mutual Interference Mitigation for MIMO-FMCW Automotive Radar”. To be submitted to IEEE Transactions on Vehicular Technology (TVT), 2022.

2. S. Jin and S. Roy. “FMCW Radar Network: Multiple Access and Interference Mitigation,” in IEEE Journal of Selected Topics in Signal Processing (JSTSP), Special Issue on Recent Advances in Automotive Radar Signal Processing, 2021.

3. S. Jin, S. Roy, and T. R. Henderson. “Efficient PHY Layer Abstraction for Faster Simulations in Complex System Environments,” in IEEE Transactions on Communications (TCOM), 2021.

4. Q. Wang, Y. Cui, S. Jin, J. Zou, C. Li and H. Xiong, ”Optimization-Based Decentralized Coded Caching for Files and Caches With Arbitrary Sizes,” in IEEE Transactions on Communications (TCOM), 2020.

5. S. Jin, Y. Cui, H. Liu and G. Caire, ”A New Order-Optimal Decentralized Coded Caching Scheme With Good Performance in the Finite File Size Regime,” in IEEE Transactions on Communications (TCOM), 2019.

Conference Papers:

1. S. Jin, P. Wang, P. Boufounos, P. Orlik, and S. Roy. “Mutual Interference Mitigation for MIMO-FMCW Automotive Radar”. To be submitted to IEEE SAM, 2022.

2. S. Jin, P. Wang, P. Boufounos, P. Orlik, and S. Roy. “Automotive Radar Interference Mitigation with Fast-Time-Frequency Mode Retrieval”. Accepted in IEEE RadarConf, 2022.

3. S. Jin, S. Roy, and T. R. Henderson. “EESM-log-AR: An Efficient Error Model for OFDM MIMO Systems over Time-Varying Channels”. In Proc. of ACM WNS3, 2021.

4. S. Jin, J. H. Park, and S. Roy. “Slow-Time Waveform Randomization Performance under Incoherent FMCW Radar Interference”. In VTC2021-Fall, 2021.

5. X. Gao, S. Roy, G. Xing and S. Jin. “Perception through 2D Sparse Array Automotive Radar under Adverse Weather”. In IEEE ICAS, 2021.

6. S. Jin, S. Roy, W. Jiang, and T. R. Henderson. “Efficient Abstractions for Implementing TGn Channel and OFDM-MIMO Links in ns-3”. In Proc. of ACM WNS3, 2020.

7. S. Jin and S. Roy, ”Cross-Layer Interference Modeling and Performance Analysis in FMCW Radar Multiple Access Network,” In Proc. of IEEE VTC2020-Fall, 2020.

8. Q. Wang, Y. Cui, S. Jin, J. Zou, C. Li and H. Xiong, ”Optimization-based Decentralized Coded Caching for Files and Caches with Arbitrary Sizes,” In Proc. of IEEE SPAWC, 2019.

9. S. Jin, Y. Cui, H. Liu and G. Caire, ”Uncoded placement optimization for coded delivery,” In Proc. of IEEE WiOpt, 2018.

10. S. Jin, Y. Cui, H. Liu and G. Caire, ”Order-Optimal Decentralized Coded Caching Schemes with Good Performance in Finite File Size Regime,” In Proc. of IEEE GLOBECOM, 2016.

Book Chapters:

1. S. Jin, X. Gao, and S. Roy. “Cognition in Automotive Radars”. To appear in Chapter 16, Next Generation Cognitive Radar Systems, IET.

Patent Pending:

1. H. Liu, G. Xing, S. Roy, and S. Jin. “Distributed Radar MAC”, applied for US Patent.

Tutorial and Teaching Experience:

1. Tutorial presenters, ACM WNS3, 2021, “Efficient PHY Layer Abstraction in ns-3: Principles and Implementation”.

2. Lecturer, ECE Department, UW, Autumn 2020, EE 505 (Probability and Random Processes).

3. Teaching assistant, ECE Department, UW, Spring 2020, EE 419 (Introduction to Computer-Communication Networks).

Industry Experience:

1. Research intern, Mitsubishi Electric Research Laboratories (MERL), Autumn 2021.
2. Software development intern, MathWorks, Summer 2021.